Department of Physics and Astronomy
University of Heidelberg

Bachelor Thesis in Physics
submitted by

Sebastian Preuß

born in Karlsruhe (Germany)

2020

Electron-Irradiation and Performance Test of the MuPix8 Silicon Pixel Sensor for the Mu3e Experiment

This Bachelor Thesis has been carried out by Sebastian Preuß at the
Physikalisches Institut in Heidelberg
under the supervision of
Prof. André Schöning

Abstract

The Mu3e experiment aims to observe the charged lepton flavor violating decay $\mu^+ \rightarrow e^+e^-e^+$ with a sensitivity of one in 10^{16} decays. Its observation would be a clear indication of the existence of physics beyond the standard model.

To fulfill the experimental requirements of high rate capability and low material budget, High Voltage Monolithic Active Pixel Sensors (HV-MAPS) have been chosen for the Mu3e pixel detector.

The detector will be placed around a stopping target located in a high intensity muon beam where the pixel sensors will be subjected to a high rate of decay electrons. Due to the low rest mass of the electron, only minor radiation damage of the bulk material is expected. However, effects due to ionizing energy deposition are assumed to occur.

To quantify these effects, a MuPix8 sensor was exposed to a strong Sr-90 source. In this thesis it is shown, that while changes due to the irradiation with a dose of $\mathcal{O}(2\,\mathrm{kGy})$ are observed, the sensor maintains a high efficiency of above 99 % and a good noise performance, thus satisfying the Mu3e requirements. Meanwhile its time resolution is degraded to a degree where it is unclear whether the requirement of an uncorrected time resolution of below 20 ns can still be reached without investigating possible compensation strategies.

Zusammenfassung

Das Mu3e-Experiment hat das Ziel, den geladenen leptonenzahlerhaltungsverletzenden Zerfall $\mu^+ \rightarrow e^+e^-e^+$ mit einer Empfindlichkeit von einem aus 10^{16} Zerfällen zu entdecken. Eine Beobachtung wäre ein klarer Hinweis auf die Existenz von Physik jenseits des Standardmodells.

Um die experimentellen Voraussetzungen der Einsetzbarkeit bei hohen Raten und eines niedrigen Materialbudgets zu erfüllen, wurden aktive monolithische Hochspannungs-Pixelsensoren für den Mu3e-Detektor ausgewählt.

Der Detektor umschließt ein Target, das sich in einem Myonenstrahl hoher Intensität befindet. Daher werden die Pixel-Sensoren einer hohen Rate von Zerfallselektronen ausgesetzt. Aufgrund der geringen Ruhemasse des Elektrons werden zwar nur geringe Strahlungsschäden am Bulk-Material erwartet. Es wird jedoch von Effekten aufgrund von ionisierender Energiedeposition ausgegangen.

Um diese Effekte zu quantisieren, wurde ein MuPix8-Sensor mit einer starken Sr-90-Quelle mit einer Dosis in der Größenordnung von $\mathcal{O}(2\,\mathrm{kGy})$ bestrahlt. In dieser Arbeit wird gezeigt, dass der Sensor trotz Veränderungen aufgrund der Bestrahlung eine hohe Effizienz von mehr als 99 % bei einem niedrigen Untergrundrauschen aufweist, wodurch die Mu3e-Anforderungen erfüllt bleiben. Die Zeitauflösung des Chips ist unterdessen so stark beeinträchtigt, dass unklar ist, ob das Ziel einer unkorrigierten Zeitauflösung von unter 20 ns noch erreicht werden kann, ohne dass Strategien zur Kompensation dieses Effekts in Betracht gezogen werden.

Contents

Part I

Introduction

1 Introduction

Currently, what is known about particle physics is summarized in the so-called Standard Model of particle physics (SM). It describes the elementary particles and their interaction. In the model, the lepton flavor is a property that is preserved. However, experiments such as Super-Kamiokande have shown that this is not the case in general due to neutrino oscillations [7]. So-called lepton-flavor-violating (LFV) events are as such a topic of high interest in modern particle physics in order to get a deeper understanding of how the Standard Model can be amended or extended and how exactly physics beyond the Standard Model (BSM) work.

The Mu3e-Experiment is designed to study such phenomena by searching for the charged LFV-decay $\mu^+ \rightarrow e^+e^-e^+$ which in the Standard Model (with extensions incorporating neutrino oscillations) is suppressed with a branching ratio of $\ll 10^{-50}$[4]. The goal is to observe this decay if its branching ratio exceeds 10^{-16} or to exclude a branching ratio greater than this at a 90 % confidence level if it is not observed [2].

This requires a detector that is capable of very high rates at the one hand while on the other hand providing a very low material budget to minimize multiple Coulomb scattering in the detector material. The development of the pixel-layer parts of this detector has been ongoing in the past years in the form of multiple generations of so-called MuPix chips. At the moment, the final generation of the sensor is coming closer and the experiment is assumed to start its operation in the upcoming few years.

The MuPix-chips are fabricated in a commercial HV-CMOS process and are built in a monolithic architecture. This means that opposed to the more conventional hybrid chips, which consist of a pixel matrix and readout circuitry that are bump-bonded together, the readout circuit is built-in in the same chip as the pixel matrix. This greatly decreases the production cost of the chip. As they can be thinned down to 50 µm, they fulfill the Mu3e requirement for a low material budget.

Detector damage due to radiation is assumed to be a non-issue in the context of the Mu3e experiment as the majority of particles are electrons or positrons and heavier particles do not hit the detector. Therefore, damage to the silicon bulk or oxide layers is not expected to occur in a large scale. While previously conducted irradiation studies of MuPix7 and design-related ATLASPix_simple sensors indicate a high radiation tolerance for neutrons and protons (see [11, 14]), a test with electron-irradiated sensors was carried out. The irradiation period of this experiment lasted for over one month and allows to tentatively estimate long-term effects a sensor in the Mu3e experiment might show.

This data will be examined in this thesis. As the exact sensor that was irradiated with a Sr-90 source was not previously tested or characterized, reference data will otherwise be reconstructed (see chapter 9 for details). Further, the irradiation process and the irradiated sensor were inspected. The irradiated sensor was characterized to check whether the Mu3e requirements are met.

2 The Mu3e experiment and the Standard Model of particle physics

The Mu3e experiment searches for the charged lepton-flavor violating decay $\mu^+ \to e^+e^-e^+$. This experiment is conducted in the context of a search for physics beyond the Standard Model. The search for charged lepton flavor violations is especially interesting when looking for new physics because the introduction of other proposed theories such as supersymmetry (SUSY) yields an experimentally observable number of lepton flavor violations. These could be observed within the sensitivity reached by the Mu3e experiment [4].

2.1 The Standard Model of particle physics

The Standard Model of particles (SM) describes the elementary particles – 3 generations of quarks and 3 generations of leptons– and their interactions, mediated by bosons. The SM is a local relativistic quantum field theory which describes the strong, weak and electromagnetic interactions. These are, besides gravity, three of the four fundamental interactions known to date.

The electromagnetic force is mediated by photons which couple to electrical charges. The photons themselves do not carry any charge. Due to the photons being massless, the electromagnetic force has an infinite range [25, pp. 205 sq.].

The strong force is mediated by gluons which couple to color charges. As the gluons carry a color charge themselves they can interact with each other. This leads to the strong force having a limited reach although the gluons are assumed to be massless [25, pp. 205 sq.].

The weak interaction is mediated by either the neutral Z-Boson or by the W^+ or W^- boson which carry one positive or negative elementary charge. Opposed to the photon or the gluon, the bosons mediating the weak force are massive: The $W^\pm$ have a mass of $80\,\mathrm{GeV}/c^2$ and the Z has a mass of $91\,\mathrm{GeV}/c^2$ [25, p. 143]. The mathematical consistency of the Standard Model requires the existence of a neutral Boson which couples to all other elementary particles proportionally to their mass. This Higgs Boson is the elementary particle associated to the Higgs field which gives the gauge bosons of the weak interaction their masses [25, p. 200].

Each generation of leptons has its corresponding lepton family number L_e, L_μ or L_τ. The charged leptons l and their associated neutrinos ν_l have $L_l = +1$ and the antiparticles $\bar{l}$ or antineutrinos $\bar{\nu}_l$ are assigned the value $L_l = -1$ [18, p. 155]. Within the Standard Model, the lepton family numbers are conserved [25, p. 142].

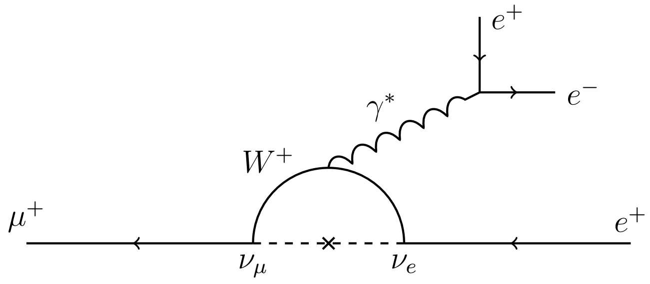

Figure 2.1: The $\mu^+ \to e^+e^-e^+$ decay caused by a neutrino oscillation.

2.2 The $\mu^+ \to e^+e^-e^+$ decay

As aforementioned, from the three forces described by the SM, only the weak force can couple to neutrinos – neutral particles that are described as massless by the Standard Model. It was however shown, that neutrinos have in fact to be massive. This makes physics involving neutrinos and the weak interaction in general interesting candidates for search of physics beyond the Standard Model [25, p. 165].

Neutrinos show so-called neutrino oscillations – a phenomenon where they can change their flavor with a periodically changing probability [25, p. 165]. This violates the lepton family number conservation.

In the scope of the Standard Model, muons decay with a probability of nearly 100 % according to the so-called Michel decay [18, p. 157]:

$$\mu^- \to e^-\bar{\nu}_e\nu_\mu \tag{2.1}$$

or for antineutrinos:

$$\mu^+ \to e^+\nu_e\bar{\nu}_\mu. \tag{2.2}$$

In this decay, the lepton flavor is conserved.

The Mu3e experiment searches for the decay

$$\mu^+ \to e^+e^-e^+, \tag{2.3}$$

where the lepton flavor is not conserved, i.e. a lepton flavor violation (LFV). Due to neutrino oscillations, this decay is allowed to occur in an extended version of the Standard Model allowing for massive neutrinos, but it is heavily suppressed. An according Feynman diagram is shown in Figure 2.1. This decay has, according to the extended Standard Model, a probability of $\ll 10^{-50}$ of occurring [12, p. 8].

Using theories beyond the Standard Model such as super-symmetry theories (SUSY), the branching ratio for a $\mu^+ \to e^+e^-e^+$ decay can surpass the value of 10^{-16} [18, p. 167]. This makes the $\mu^+ \to e^+e^-e^+$ decay such an interesting object of study as an observation would be a clear indication of the existence of physics beyond the Standard Model.

2.3 The Mu3e experiment

The Mu3e experiment aims to observe the decay $\mu^+ \to e^+e^-e^+$ if its branching ratio exceeds 10^{-16} or to otherwise exclude this branching ratio to a confidence level of

90 %. In order to achieve this, it has been calculated that a total of more than 10^{17} muons have to be stopped [2, p. 6].

The experiment is planned to be ran in two phases: Phase I works with the existing πE5 beamline at the Paul Scherrer Institute (PSI) located in Switzerland. This muon beam provides a rate of up to 10^8 Hz, allowing to test the branching ratio of the $\mu^+ \to e^+e^-e^+$ decay to a single event sensitivity of 2×10^{-15}.

The second phase requires a beam intensity of 2×10^9 Hz to test the targeted sensitivity within one year. It is set out to be ran after the proof-of-concept phase I has succeeded and once the appropriate beamline is built. The so-called high intensity muon beam (HiMB) is currently under development at PSI and aims to provide the required rate when finished.

2.4 The Mu3e detector

In order to measure the decay $\mu^+ \to e^+e^-e^+$, the main particles the Mu3e detector will have to detect are positrons (and electrons). To allow for a meaningful track reconstruction, scattering of these low-energetic light particles has to be kept to a minimum. This requires the actual detector chips to be as thin as possible. This is realized with silicon high-voltage monolithic pixel sensors (see section 2.5) for the inner and outer detector which is shown in Figure 2.2.

The concept for the whole detector is depicted in Figure 2.3: The detector has a hollow double-cone target at its center, around which two inner pixel layers are placed as a barrel. Going further outwards from the center, the detector features a scintillating fiber tracker for more accurate timing information accompanied by an outer double-layer of silicon pixel detectors. Up- and downstream of this central detector part, recurl stations are placed. These feature one layer of scintillating tiles each and a double-layer of pixel detectors which essentially form an extension of the outer part of the central detector [2, p. 11]. The whole setup is placed in a 1 T magnetic field so that charged particles are subjected to the Lorentz force allowing for particle identification and the reconstruction of particle momenta from reconstructed tracks.

2.5 The HV-MAPS concept

The tracking detector of Mu3e is realized through so-called **h**igh-**v**oltage **m**onolithic **a**ctive **p**ixel **s**ensors (HV-MAPS). Theses detectors combine multiple favorable properties of other sensor concepts or particle detectors in general: Figure 2.4 shows pixels of an HV-MAPS detector where the depletion zone of a diode is paired with in-pixel electronics: The latter part explains the "monolithic" part of the HV-MAPS' name: Unlike conventional hybrid sensors consisting of a pixel part and a readout part which have to be bonded together, the HV-MAPS detector has the required circuitry built-in in the same chip as the pixel matrix.

The actual signal generation happens in a reversely biased diode where a passing particle creates electron-hole pairs via ionization. The charge is then – in a conventional MAPS detector – collected via diffusion which hampers the achievable time

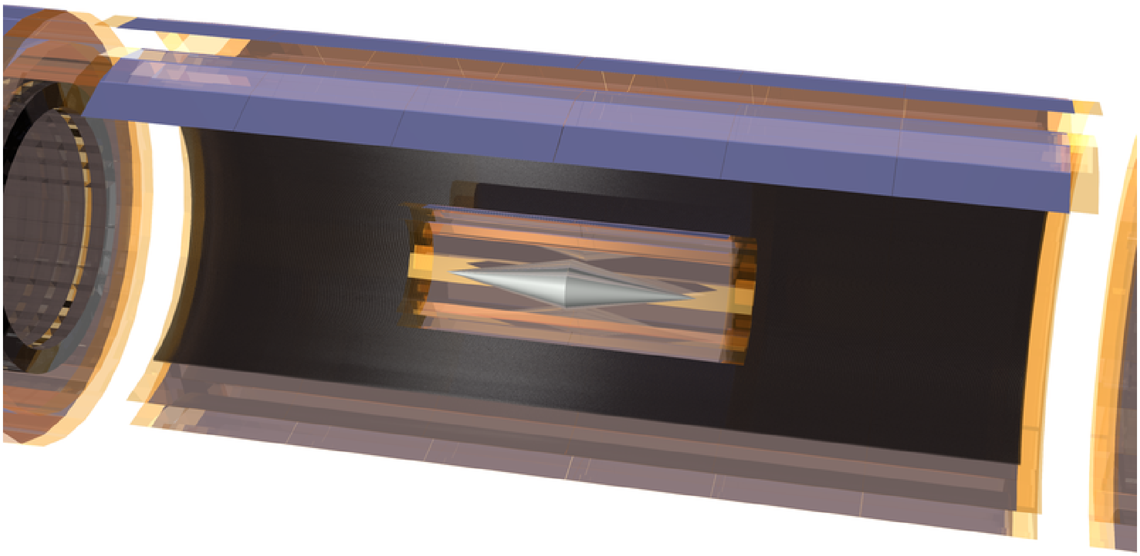

Figure 2.2: The central silicon detector part with the double-cone target and the scintillating fibers [22].

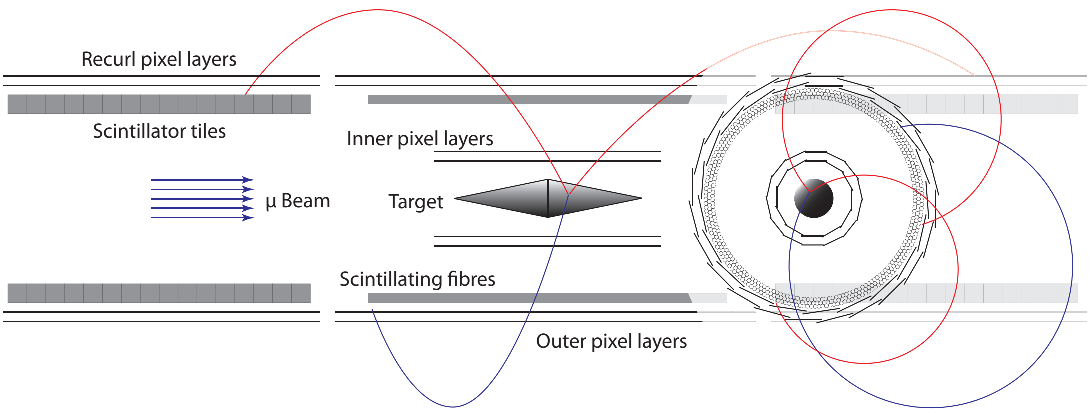

Figure 2.3: The concept for the Mu3e detector [22].

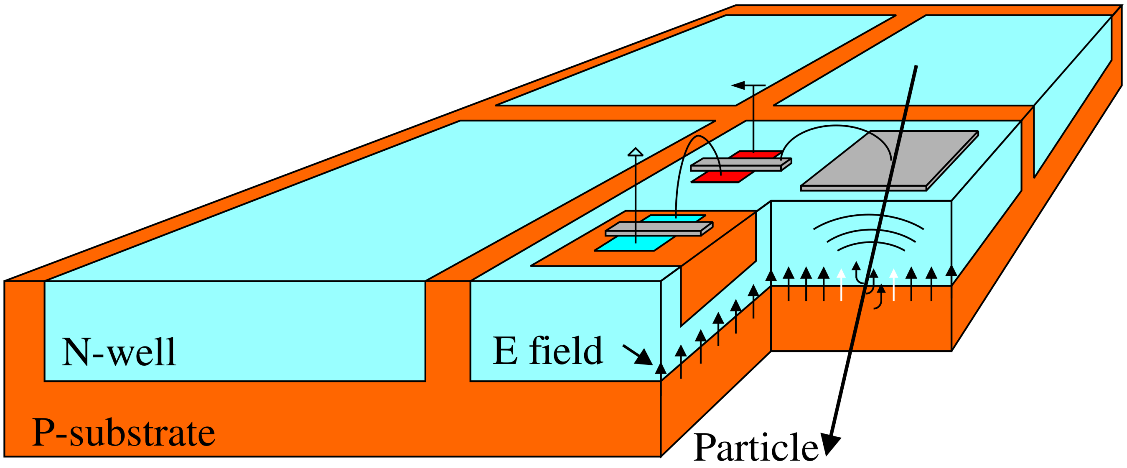

Figure 2.4: Schematic of four pixels of a HV-MAPS chip [23, p. 877].

resolution. This is circumvented by applying a high voltage: Charge collection now is sped up due to drift and also the depletion region of the diode is enlarged.

HV-MAPS have the advantage that they can be thinned to a decreased sensor thickness. This greatly reduces unwanted scattering effects, most notably multiple Coulomb scattering is reduced to a minimum as the detector thickness can be decreased down to 50 µm which is equal to less than 0.1 % of a radiation length [2, p. 26]. In addition, HV-MAPS can be manufactured in a commercial HV-CMOS (**c**omplementary **m**etal-**o**xide-**s**emiconductor) process which leads to a comparably low production cost.

2.6 The MuPix8 sensor

The MuPix8 is an HV-MAPS prototype developed as one iteration of the MuPix series of sensors for the Mu3e experiment. It is the successor of the MuPix7 and the first chip in the series to move the HV-MAPS concept to a large scale [14, p. 34].

The pixel matrix of the MuPix8 is made up of 128 columns × 200 rows with pixels measuring 80µm × 81µm (column width × row height). The pixels are divided in three sub-matrices, matrix A, B and C. The first 48 columns make up Matrix A, the following 48 columns comprise Matrix B and finally Matrix C is made up of the remaining 32 columns. These all have an individual data readout links, additionally the MuPix8 features one more link that can deliver multiplexed data from all submatrices together [14, p. 34].

Matrix A features a voltage mode signal transmission while matrices B and C use a current mode signal transmission. The MuPix8 chips come in substrate resistivities of 80 Ω cm and 200 Ω cm. The wafers have a thickness of 100 µm but the chips can be thinned to 50 µm. The sensors are fabricated in the AMS aH18 process with a minimum transistor gate length of 180 nm [34, pp. 2 sqq.].

Figure 2.5a shows the layout of the MuPix8: The main parts that are clearly visible are the pixel matrix, below it the readout part and at the bottom of the chip the end-of-column logic, the digital periphery and the bonding pads can be seen.

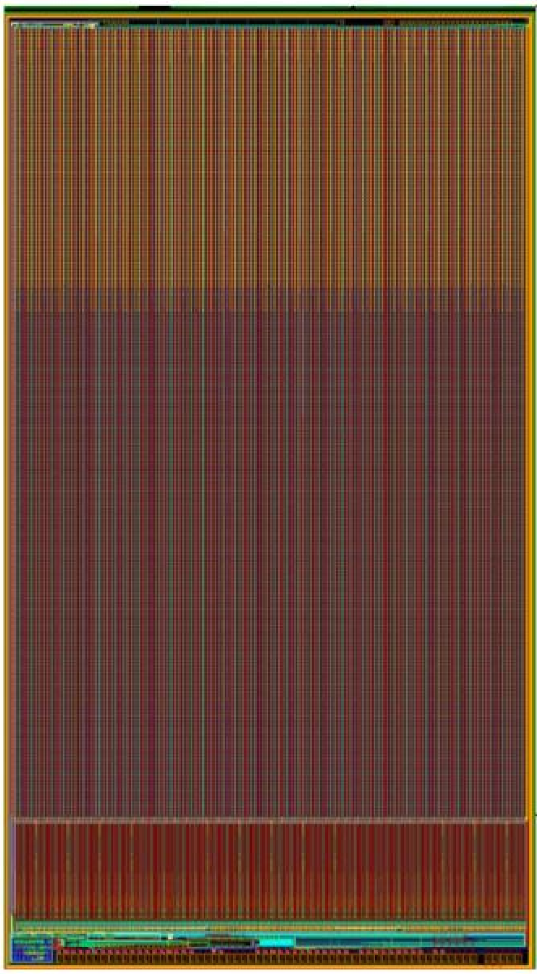

(a) MuPix8 layout [34].

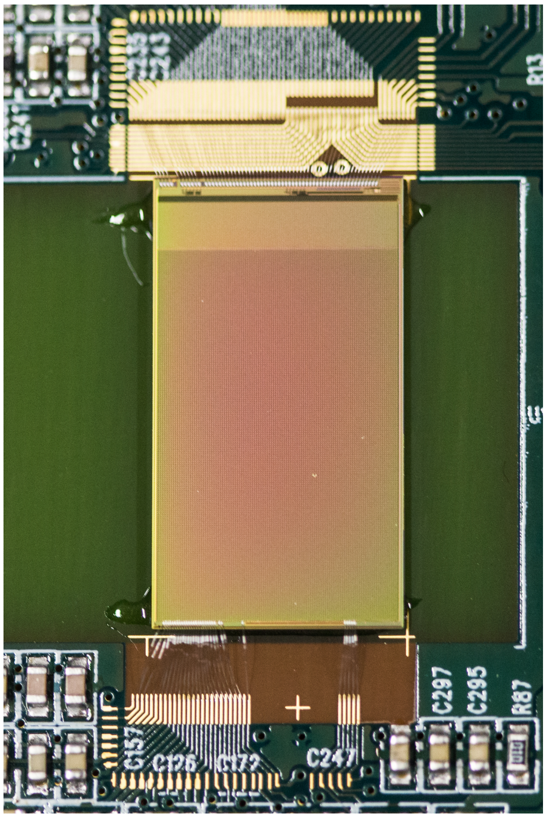

(b) The chip wire-bonded to an insert board [22].

Figure 2.5: The MuPix8 with a visible division in pixel matrix and the digital periphery.

3 Particle interaction with matter

When particles enter a given piece of matter, there is a probability of the particle interacting with it. The probability of an interaction happening depends amongst others on the material thickness and its composition as well as the particle type and its energy. The consequences of such interactions are twofold: On one hand, the incoming (primary) particle and the emitted (secondary) particle which is produced in the interaction differ in type or momentum – the interaction influences the particle. On the other hand the interaction changes the material the particle is entered by: These changes can be temporary, e.g. in momentary changes of internal electromagnetic fields, or permanent, e.g. in changed lattice structures in solids.

These interactions form the basic principle upon which particle detectors work: The resulting effects of the interacting particle in the detection volume are transformed into signals which can then be read out and analyzed [20, p. 5]. At the same time, the detector is damaged (or at least altered) by the incoming particles it detects. With high fluences or over long irradiation periods these effects can accumulate and significantly impact the performance.

The stopping power of a material describes the mean energy loss per distance traveled of a particle and is usually dependent on the type of particle, although there exist some generalizations for certain groups of particles. Charged particles dominantly lose kinetic energy through electromagnetic interaction with the atoms of the detector material, where these atoms are excited or ionized [20, p. 52]. This so-called collision loss is described for heavy particles (i.e. all particles except electrons and positrons because for these annihilation and particle exchange have a significant impact) by the Bethe-Bloch equation [16, p. 31]. For electrons and positrons, it is described by the following equation found by Berger and Seltzer:

$$-\frac{1}{\rho}\left(\frac{\mathrm{d}E}{\mathrm{d}x}\right) = \frac{0.153536}{\beta^2}\frac{Z}{A}B(T) \tag{3.1}$$

where the following symbols are used: $\beta = \frac{v}{c}$ is the velocity of the particle in relation to the speed of light, Z is the atomic number (i.e. number of protons), A is the mass number (the number of protons and neutrons) and T is the kinetic energy of the incoming particle [28, p. 665]. $B(T)$ is the the so-called stopping power calculated as

$$B(T) = B_0(T) - 2\ln\left(I/mc^2\right) - \delta \tag{3.2}$$

where in turn I is the mean excitation energy of the medium being entered and mc^2 is the rest energy of the electron/positron. δ describes the density-effect correction and $B_0(T)$ can be easily calculated from the kinetic energy.

Berger and Seltzer however found a simplification for the $B(T)$ term based on experimental data:

$$B(T) = \begin{cases} B_0(T) + b_0 - b_4(p/mc^2) & \text{where } T \leq T_0 \\ B_1(T) + b_1 - b_2\left(1 - [2\ln(p/mc)/b_4]\right)^k & \text{where } T_0 < T < T_1 \\ B_1(T) + b_1 & \text{where } T \geq T_1. \end{cases} \tag{3.3}$$

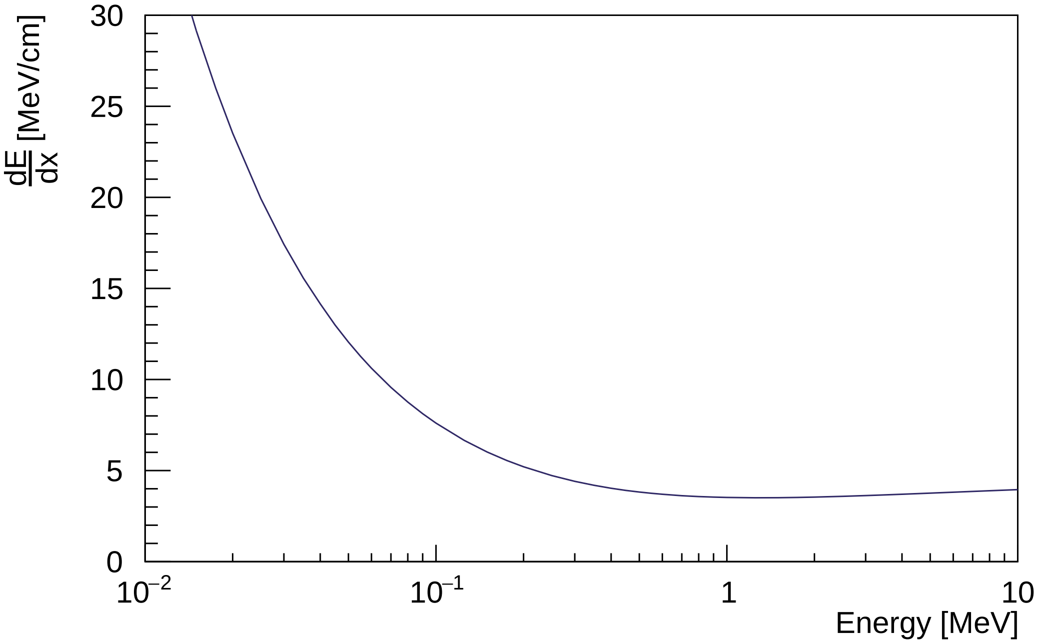

Figure 3.1: The stopping power of an electron in pure Si according to data from [28].

They catalogued the values of $B_0(T)$, $B_1(T)$, $b_0 \ldots b_4$, k for several energies and electrons and protons and T_0 and T_1 for 98 elements and 180 compound materials [28, p. 675]. This allows for an easy calculation of the stopping power of electrons and protons in different materials. One example can be seen in Figure 3.1, showing the stopping power of electrons in pure silicon.

4 Radiation damages in detectors

All particle detectors are – due to the very nature of the environment they are used in – subject to radiation which will, as described below, very likely damage or at least alter the internals of the detector. This is especially true for those detectors placed close to the interaction point as they will naturally be the part of a detector setup that is the most exposed to radiation. Thus it is essential to design radiation-hard detectors and ultimately test the radiation hardness.

4.1 Radiation damages in silicon detectors

Generally, there are two types of radiation damages that occur in silicon chips: Damages to the silicon bulk and changes in the oxide layers. The effects on the bulk are referred to as NIEL-effects as they stem from **n**on-**i**onizing **e**nergy **l**oss. The effects on the oxide layers are also called TID-effects (or IEL-effects) which stands for **t**otal **i**onizing **d**ose.

4.1.1 Damages and their effects

These processes damage different parts of the detector: The silicon bulk is mainly harmed by non-ionizing energy loss processes leading to displacement damages in the silicon lattice. Depending on the deposited energy, these so-called primary defects can lead to cluster defects [1, pp. 2 sq.].

This process is complicated by instabilities of the defects which leads to them propagating through the material to form more stable configurations. This process of defect reordering is called *annealing* and is highly temperature dependent. The defects in the silicon lattice then impact its optical and electrical properties and such the functioning of integrated circuits: Energies in the band gap rise when the lattice has structural defects. This in turn leads to the generation of electron-hole pairs which leads to an increased leakage current. Also, temporary charge trapping can happen reducing the efficiency of silicon-based charge-coupled devices or active pixels. When exposed to higher amounts of radiation, the effect of so-called type-inversion, whereby a n-type material is converted to a p-type material by the introduction of acceptors can happen [31, pp. 653 sqq.].

The total ionizing dose describes the amount of energy deposited into the detector. The effects arising from this ionization mostly affect the silicon oxide layers which are used as isolation layers in transistors. With decreasing process- and transistor sizes, the thickness of these SiO_2 layers has decreased as well down to the order of 10 nm. Consequently, TID effects do not play as large of a role in modern transistor designs as they used to [6, p. 2413]. The effects of a high dose seen by a single transistor are increases in the leakage current and a shifted threshold voltage. These effects highly depend on the foundry as well as the bias condition during the irradiation [8, pp. 750 sqq.].

4.1.2 The nature of anticipated Mu3e radiation damages

According to Equation 2.1 muons (antimuons) mainly decay into an electron (positron) and neutrinos. As the Mu3e experiment aims for a muon rate of 10^8 Hz (and higher rates in phase II of the experiment) [2, p. 6], the decay products registered by the detector can well be approximated to be electrons originating from the stopping target at about the same rate. These will of course not all be registered by one sensor, but the hottest sensor is expected to be hit by a rate of 5.2 MHz [2, p. 85].

Opposed to proton- or neutron-irradiation, electrons have a comparably low rest mass. This makes structural defects in the silicon bulk very unlikely to occur: An electron needs more than 1 000 times the energy of a proton or a neutron to cause a point defect and more than 300 times the energy to cause defect cluster [21, p. 277]. As such it is assumed, that the effects of bulk damages are negligible when looking at the electron-irradiation that was conducted on the sensor examined in this thesis.

However charge accumulation in oxide layers is very likely to occur. This leads to shifted working points in the transistors making up the functionality of the sensor. This might lead to a reduced efficiency or at least changed parameters for the optimal sensor performance. Further, one expects increased leakage currents. This in turn raises the chip temperature and imposes somewhat tighter limits on the cooling solution.

4.1.3 Calculating the effect of radiation damages

A lot of results describing the damages caused by radiation heavily rely on experimental data and many processes are not fully understood. NIEL effects are usually expressed in a measure of so-called 1 MeV neutron-equivalent fluences (often shorted to neutron-equivalent fluences), denoted as $\mathrm{n_{eq}/cm^2}$. Here, $1\,\mathrm{n_{eq}/cm^2}$ equals the NIEL damages caused by one neutron at an energy of 1 MeV. As per the NIEL scaling hypothesis, the bulk damages and thus the change in electrical and optical properties are proportional to the NIEL [13, p. 194]. In this context, the NIEL can be calculated as

$$\mathrm{NIEL} = \left(\frac{N}{A}\right)\left[\sigma_e L(T_e) + \sigma_i L(T_i)\right] \tag{4.1}$$

where $\sigma_{e/i}$ are the total elastic (or inelastic, respectively) cross sections and $T_{e/i}$ are the associated average recoil energies. N is Avogadro's number and A is the gram atomic weight of the target material [31, p. 660].

The recoil energies in this context have to be corrected for ionization losses (so that only the displacement energy is considered); this is done by incorporating the Lindhard factor $L(T)$ describing exactly this fraction [19, p. 411]. According to this hypothesis, bulk radiation damages can be theoretically handled relatively independent of the particle type or its impact energy.

To date it is very hard to analytically estimate radiation damages and it is heavily relied on simulations and irradiation campaigns to assess the actual damage done by radiation.

The same is true for the effects caused by the total ionizing dose: Due to these effects heavily depending on the fabrication process and the foundry as well as the bias conditions during the irradiation, it is not possible (at least without elaborate simulation work) to analytically gain meaningful quantitative predictions. Rather, experimental data is needed to gain reliable insight and a solid foundation to base further calculations on.

4.2 Irradiation campaigns

In order to estimate the effect, radiation damages have on particle detectors, so called *irradiation campaigns* are conducted. This process is split up in three main parts:

In a first part, the total radiation dose encountered by the detector over the whole experiment runtime is calculated as this is the minimum dose the detector should withstand, i.e. it has to be in an overall working state and it has to still fulfill the experimental requirements regarding especially resolution and efficiency.

In a second step, a detector to be tested for its radiation hardness is then irradiated with the expected dose in a comparably short time-frame, usually days or weeks.

The irradiated detector is then tested and analyzed to gain information on how its functionality or characteristics have degraded (or maybe even changed to the better) due to the irradiation process.

Part II

Setup

5 The irradiation process

As the main source of irradiation during the Mu3e-experiment stems from electrons, an irradiation study using electrons was conducted: In a first step, a sensor was irradiated with a Sr-90 source and was then later studied at a testbeam.

In the time period between the irradiation and the testbeam, the sensor was put in a freezer, to prevent annealing effects by greatly slowing down the annealing process. To check whether the observed effects actually originate from the irradiation, the irradiation setup was later replicated without a radioactive source for a controlled reference measurement.

5.1 The experimental setup and conditions

A MuPix8 chip was irradiated using a Sr-90 source in the "Isotopenlabor" in the basement of the Physikalisches Institut in Heidelberg. The irradiation of the MuPix8 sensor with the ID 265-6-3 started on 24.05.2019, 16:00 (± 30 minutes) and lasted until 27.06.2019, 09:30 (± 30 minutes). Consequently, the sensor was irradiated for a total of $(809.5 \pm 0.4)\,\mathrm{h}$. A mock-up picture of the setup can be seen in Figure 5.1.

A Sr-90 source was mounted 0.5 mm above the protective cap of the sensor which measures 1 cm in height. The whole setup was placed in an acrylic glass box to shield observers from stray radiation emitted by the source. The sensor was powered during the irradiation and automated measurements were done in specified intervals during the irradiation period: The leakage current as well as all bias currents were recorded once every second. To save hard-drive space, the data output was saved for a 10-second period in 5-minute intervals.

The sensor was operated at a high voltage of $-50\,\mathrm{V}$. During the first part of the irradiation, the blinds were not closed so the results show a certain light-sensitivity of the chip (see section 10.3). In the second part, the chip was placed in a dark environment. This happened after the 03.06.2019, i.e. after the 11th day of irradiation.

It was foreseen to turn the power off at some time to check how the sensor would react to being turned off for a period of time. Due to a power outage at the institute the sensor was unintentionally cut off the power and as such the effects of this will be studied. The power went out on 25.06.2019 at 02:44 (±1 minute) and came back on the same day at 12:03 (±1 minute). The sensor was thus unpowered for 9:19h.

5.2 Setup of the reference measurement

To be able to attribute the changes in the sensor to the irradiation and to exclude that they stem from some other effects of long-term running, a measurement without a radioactive source was conducted. This reference measurement was set up just as

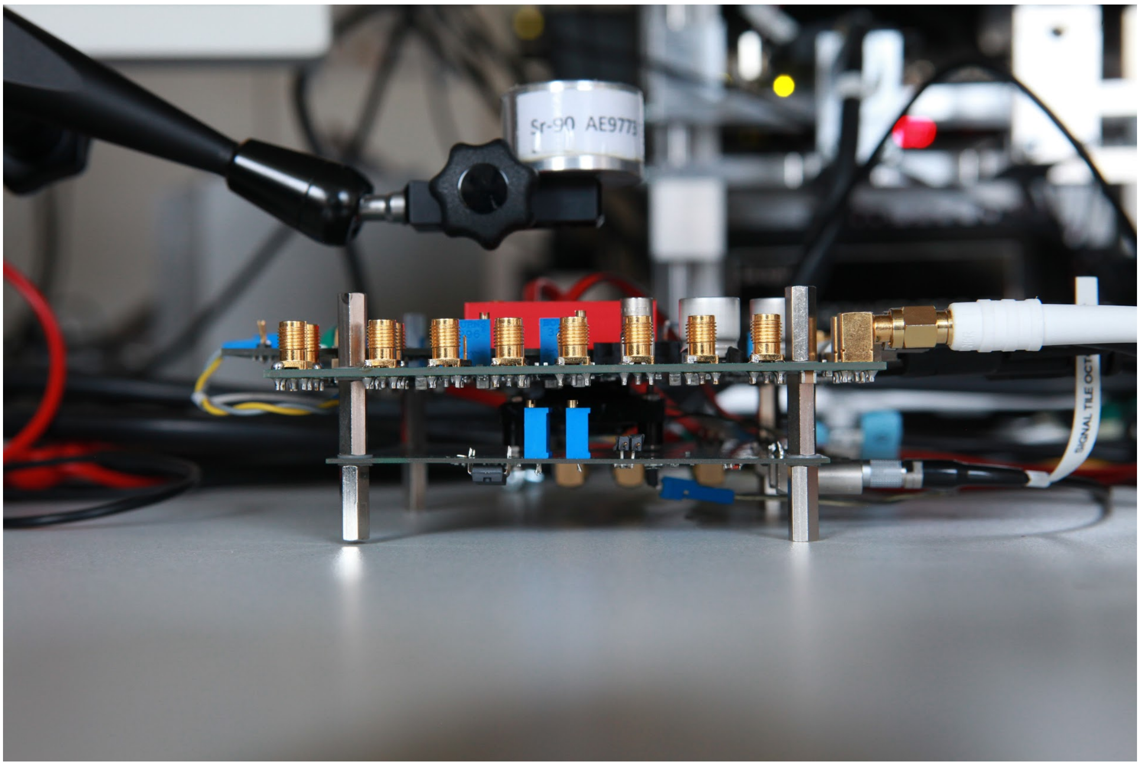

Figure 5.1: Mock-up of how the irradiation setup looked [15].

the one described in section 5.1. There was no source placed above the detector so it is only subject to the background radiation seen by the irradiated detector as well.

Due to time and equipment constraints, the sensor ran for 3 days without an ongoing power monitoring: The setup was started on 02.10.2020 at 19:20 ($\pm$5 minutes) in a laboratory in the PHYSIKALISCHES INSTITUT and ran until 05.10.2020 at 14:15 ($\pm$5 minutes), i.e. it was powered for 66:55 hours. It was then equipped with proper automated measurement tools and transferred to the Isotopenlabor where the original irradiation took place. The measurement was resumed at 17:20 ($\pm$5 minutes). From that time on it ran without interruption for 570:55 hours until 29.10.2020, 11:15 ($\pm$1 minute). Consequently, the sensor was powered for 637:50 ($\pm$5 minutes). This measurement was conducted using the sensor with the ID 265-3-5.

6 The testbeam procedure

Before using pixel detectors in a final experiment, numerous tests over multiple sensor generations are usually conducted. For measurements that cannot be done in a laboratory, e.g. tests with high-energy particles, so-called testbeam-facilities are open to the scientific community. There, measurements with accelerated particles can be conducted. These have the ability to pass through multiple detector layers which allows for track reconstruction in a proper setup. In order to do this, the sensor is placed in a so-called telescope (see section 6.1), an arrangement of multiple reference sensors and one sensor to be tested. This telescope is then placed in the particle beam. With the data from all sensors, particle tracks can be reconstructed from the data of the reference sensors. These tracks are then used to study the performance of the **d**evice-**u**nder-**t**est (DUT) like its efficiency or the time resolution.

6.1 The telescope

The telescope contains multiple sensor layers working as a reference and one DUT sensor. The general idea is to use the reference layers to gain data about particles passing through the telescope to evaluate DUT performance based on this data.
The main goal is to reconstruct tracks of particles registered by the reference detectors. This means that at least 3 reference layers have to be used because a straight line track through two points can always be trivially found. In the data analyzed in this thesis, all data taken at testbeams was gained using three MuPix8 reference layers.

The DUT is usually placed directly after the first reference detector. That way the particles hitting it have only been subjected to a minimal amount of scattering. For different DUT properties to be tested, suitable strategies for setting up the reference system are employed: By using reference detectors with smaller pixel sizes (and thus a better spatial resolution), sub-pixel resolution studies can be conducted (i.e. areas of single pixels can be checked for their efficiency). Similarly when the reference offers a good time resolution, the time resolution of the DUT can be determined more precisely. For this reason the MuPix-telescopes are all equipped with a scintillating tile detector providing a reference time information. An image of a telescope similar to the ones used for data-taking for this thesis is shown in Figure 6.1.

6.2 The DESY testbeam facility

All testbeam data analyzed in this thesis was taken at the DESY II testbeam facility. It is located in Hamburg and provides beamlines with particle momenta ranging from $1\,\mathrm{GeV}/c$ to $6\,\mathrm{GeV}/c$. The DESY testbeam lines provide electrons and positrons: From the primary beam of the DESY II synchrotron, bremsstrahlung photons are

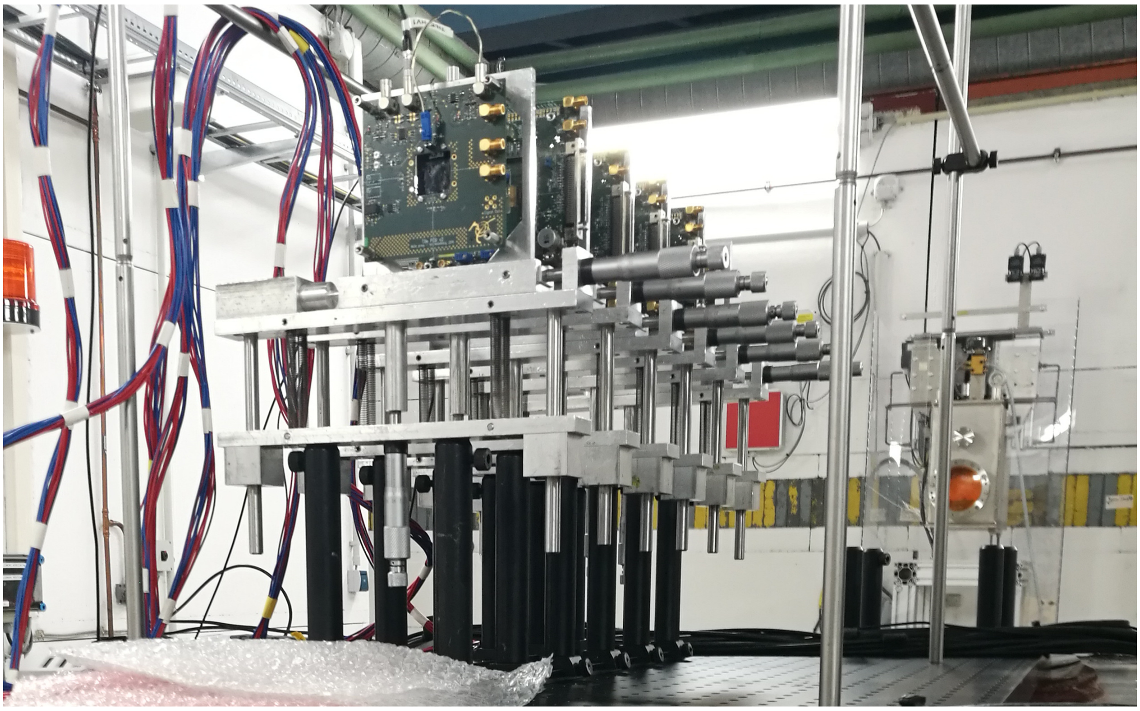

Figure 6.1: A telescope set-up at DESY consisting of 4 pixel detector layers and two scintillating tiles for timing reference.

emitted in a fiber target which then create electron-positron-pairs when hitting a secondary target [5]. All testbeams analyzed in the scope of this thesis were conducted with electrons.

6.3 Analysis of testbeam data

The data collected at testbeams is analyzed with a framework developed by the Mu3e-group in Heidelberg. While some steps or procedures can optionally be left out to speed up the analysis or to get results e.g. without certain corrections, the main steps are as follows:

1. Offline-alignment and analysis setup Before any real data analysis is run, a few checks and setup are done: The main point here is the offline-alignment of the telescope. Before testbeam data-taking is conducted, the layers in the telescope are aligned with micrometer-screws (shown in Figure 6.1) to guarantee a maximal overlap of the layers in beam direction. However, there is always some translational and rotational offset which needs to be corrected for offline. This is calculated beforehand in three steps:

In a first step, all layers are translationally aligned based on the column-to-column and row-to-row correlations of the hit positions. This does not take into account beam slopes or rotational mis-alignments and only serves as a preparatory step for the actual alignment:

This is done based on tracking information. The procedure is as follows:

- Tracks through all reference layers are built based on the hit-information (i.e. hit position and time stamp) and the information on layer position and rotation gained in the previous step (this procedure is the same one used in the actual analysis described below in more detail).
- From these tracks, slopes and residuals are computed: The track does not always go straight through a hit but rather always has an offset: The residual is the vector from the hit position to the track position. By splitting this vector in its components, the X- and Y- residuals, one can calculate the appropriate horizontal and vertical distances by which the chip needs to be shifted for a better alignment.
- By taking profiles of the residual histograms, rotational corrections can be calculated which are then also applied.
- These corrections are not always applied to their full degree to prevent the automated process from optimizing for local minima in the residual distribution.

The above is iterated multiple times to gain a soundly aligned reference system.

The DUT is then aligned using basically the same principle, but rather than building tracks through it, the DUT is aligned using the residuals between DUT-hits and tracks going through the reference layers only (where the process of deciding which hits/tracks to even compare in the first place is called matching and is described in detail below). This ensures that the analysis is not biased towards the DUT and higher quality results can be gained.

The obtained geometry is then saved to disk and used in the actual analysis for runs with the same geometry. For all analyses discussed in this thesis, the offline alignment was repeated every time the beam area was accessed, regardless of whether sensors were changed or touched to ensure potential changes in alignment e.g. due to changed cable strain or other unnoticed effects are accounted for.

2. Track-building through reference layers Building tracks through the reference layers is – just like the matching – one of the steps that the analysis and the offline alignment have in common: Three reference layers are used to ensure that particle tracks are actually reconstructed from particles and not from coincidental noise occurrences.

Hits occurring within a chosen time-window, set as a cut on all reference layers are connected by a straight-line fit. The reconstructed tracks are then classified based on their χ^2/n.d.f value and either used or rejected for further analysis.

3. Clustering On the DUT layer, hit information originating from neighboring pixels within a short, predefined time window are grouped together as a cluster. As there are mainly two reasons for a cluster to occur – actual charge sharing from a single hit and cross-talk – this can improve (in the former case) or worsen (in the latter case) the spatial resolution.

This step is – as of now – only done for hits on the DUT. It is currently a work in progress to extend this clustering process to the other layers in order to build

tracks not through hits but rather through clusters.
While this does decrease the spatial resolution of tracks, the order of this inaccuracy is below that of the size of a single pixel. As spatial resolution is not examined in the scope of this thesis, this aspect does not degrade the results in a meaningful manner.

4. DUT-Matching of tracks Having the clusters and the tracks computed, the DUT clusters are now matched to tracks through the reference layers. Whether a match is made is defined by both a matching time and a matching radius which can be individually defined for each analysis run.

From the data gained in the analysis steps explained above, multiple DUT properties can then be deduced which are explained in detail in the following part:

6.3.1 Efficiency and noise

The efficiency is calculated as the number of tracks that could be matched to a hit divided by the number of total tracks:

$$\text{Eff} = \frac{\#\ \text{matched tracks}}{\#\ \text{total tracks}} \tag{6.1}$$

It is closely intertwined with the noise which is defined as the number of unmatched hits on the DUT (attention: For the efficiency calculation the number of clusters is the significant figure, for the noise it is the number of hits as noise-hits are assumed to not be from a particle, so clustering them together would make no sense). The noise is usually expressed as a frequency over a given time interval:

$$\text{Noise rate [Hz/pixel]} = \frac{\#\ \text{unmatched hits}}{\#\ \text{pixels} \cdot \text{time}} \tag{6.2}$$

This calculation generally overestimates the noise because of inefficiencies in the reference layers: When a particle is present that is not registered by one of the reference layers but by the DUT, the associated DUT hit is registered as noise by the described procedure due to the absence of a track to match it to. This effect can be corrected for in the following way:

The efficiency of the reference system is given as (cf. [14, p. 50])

$$\epsilon_{ref} = \prod_{1}^{N_{layers}} \epsilon_i \tag{6.3}$$

where ϵ_i describes the efficiency of the i-th reference plane. The fraction of wrongly assigned noise hits is then given as:

$$\frac{N_{wrong}}{N_{tracks}} = \frac{1}{\epsilon_{ref}} - 1. \tag{6.4}$$

The additional noise rate per pixel can then be calculated as:

$$R_{add} = \frac{N_{tracks}}{t_{run} \cdot N_{pixels}} \cdot \left(\frac{1}{\epsilon_{ref}} - 1\right). \tag{6.5}$$

With some numbers taken from the data analyzed in chapter 11, an estimate for this added noise ration can be given:

$$R_{add} = \frac{1,123,732}{76.2267\,\mathrm{s} \cdot (200 \cdot 48)\,\mathrm{px}} \cdot \left(\frac{1}{(0.995)^3} - 1 \right) \approx 0.02\,\frac{\mathrm{Hz}}{\mathrm{s}} \tag{6.6}$$

This calculation assumes 3 reference layers (as was used for all analyses in the scope of this thesis) and an assumption of 99.5 % efficiency for each reference layer which is usually surpassed, so this value can be seen as an upper boundary for the artificially introduced noise rate. Because of the negligible size of the effect, this correction is currently omitted in the analysis.

Another drawback of using this approach is the inclusion of unwanted edge effects: As the reference sensors have the same size as the DUT, particles passing near the edge of the sensor with a slope can be registered by multiple sensors and be out of the pixel matrix of other sensors. This problem is amplified when considering particles scattering in the telescope from outside which happens mainly on the sensor edges. This is corrected for by omitting the outer 5 rows/columns of the DUT for the analysis resulting in an effective matrix of 38×190 pixels.

6.3.2 Cluster size and crosstalk

From the clustering step, the average cluster size can directly be deduced. The clustering stems from two effects:

Charge sharing Clusters can originate from so-called charge sharing, a process in which an incoming particle deposits charges in multiple pixel cells. It is mainly influenced by the incident angle of the particle and its position relative to the pixel: Particles with an angle differing from the perpendicular and those passing near the edges of a pixel are most likely to lead to charge sharing [26, p. 65].

In the telescope the particles hit the detector in an approximately perpendicular angle, so the effect of charge sharing is small. When placing the detectors at an angle however, an improved spatial resolution could be observed as the information from multiple pixels allows a better determination of the position of the particle than just the information from one pixel.

Crosstalk Clusters can also be registered due to the occurrence of line crosstalk: This is an effect due to the capacitive coupling of signal lines: In the MuPix8 which is characterized in this thesis, the digitization of the analog pulses happens in the periphery. This means in turn that the signal has to be transmitted to the periphery. As the signal lines for multiple pixels are neighboring each other, there is a capacitive coupling between them which can lead to the induction of a secondary pulse in the neighboring signal line which is then interpreted as a clustered hit. Especially for Matrix A of the MuPix8 which has a voltage-based line driver, the occurrence of crosstalk is favored.

Due to its nature, crosstalk is depending on the on-chip routing. The MuPix8 is routed in a way that crosstalk can pretty much only occur on two vertically neighboring pixels and is favored in columns with higher numbers. This leads to an easily applicable, statistical correction for crosstalk in the recorded data:

At a sufficiently large number of hits it is assumed that the number of clusters stemming from charge sharing should be equally distributed between horizontally and vertically extended clusters. Based on this assumption, one can then deduce the difference of the numbers of horizontal and vertical clusters to be the number of hits for which crosstalk occurred. The crosstalk probability of a hit in a cluster is thus given as:

$$\text{xt-probability} = \frac{n_{\text{cluster, vertical}} - n_{\text{cluster, horizontal}}}{n_{\text{cluster, vertical}} + n_{\text{cluster, horizontal}}}. \tag{6.7}$$

The above correction has the significant drawback of only being of statistical nature. This means while one gets a sound estimate for the actual cluster size originating from charge sharing, a discrimination on whether a single cluster originated from crosstalk or not cannot be made. This means that the improved spatial resolution based on crosstalk is partly canceled out. This can be counteracted by certain techniques such as weighting the cluster position by the time over threshold of each pixel which is proportional to the charge deposited. The evaluation of such techniques is however beyond the scope of this thesis and at least for telescope data effects are expected to be slim anyways.

6.3.3 Time resolution and corrections

The time resolution of the MuPix8 sensor is calculated using the reference time information provided by the scintillating tiles placed upstream and downstream of the telescope: The difference between the hit time-stamp `TS1` of the MuPix and the reference time information $\mathtt{T}_{\mathtt{REF}}$ of the tile is plotted in a histogram and fitted with a gaussian function. The time resolution of the sensor is then defined as the σ-parameter of this function.

Because of effects discussed below, the histogram is not symmetric around its mean but rather has a “tail” to its right with a much slower fall-off than towards the left. For this reason, the fitting range is chosen to only include the peak and some of the right edged of the gaussian peak. An example of this fitting range is shown in Figure 6.2.

The initial, raw time resolution can however be improved significantly by applying some correction steps. In the analysis used here, three corrections are implemented:

a) Run correction The FPGA (**f**ield **p**rogrammable **g**ate **a**rray) recording the data and the chip run on different clock speeds: Namely the FPGA runs at a frequency of 500 MHz while the chip runs at 125 MHz. On the other hand, the data is recorded in so-called runs: Self-contained units of acquired data at a certain chip setting. As a result of this, the synchronization between chip- and FPGA clock cycle could differ from run to run (i.e. the recording can start in any of the 4 FPGA clock cycles within one chip clock cycle).

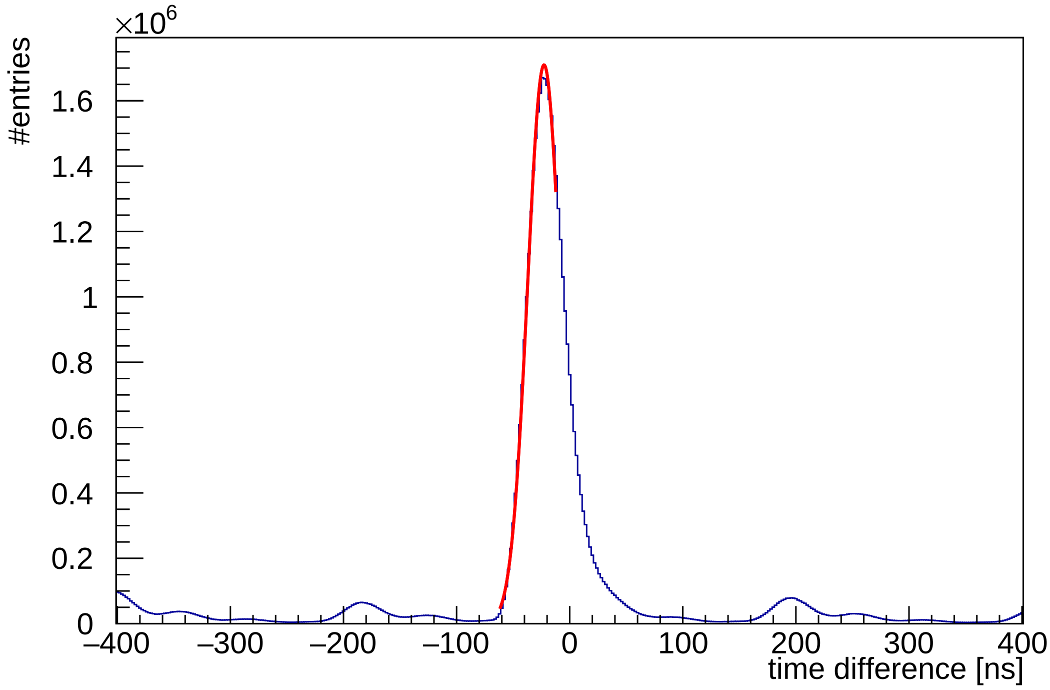

Figure 6.2: The fitting range of the gaussian function for the time resolution mainly covers the rising edge for better fit accuracy.

As a run is merely a construct to have a contained unit for the analysis, but multiple runs are analyzed together in order to gain more statistics, this is an artificial delay which is corrected for in the analysis by retroactively lining up these differences between the single runs.

b) Delay correction Earlier measurements of the time resolution of the MuPix8 showed that pixels with higher row and/or column addresses showed an increased delay between `TS1` and $\mathtt{T_{REF}}$. The correction that has been found and that is adapted for the analyses done in the scope of this thesis is detailed in [9, p. 83]. It mainly consists of three steps:

First, the sensor's pixels are grouped in super pixels, where each super pixel measures 8×8 px (note: in [9] these were 6 columns × 8 rows large). This is done to reduce the effect of pixel-to-pixel variations and to gather more statistics. In the second step, the mean delays of every super pixel (the mean delay of every hit registered in one of the pixels in the super pixel) are put in a 2-dimensional histogram which is then fitted with a 2-dimensional linear function

$$\mathrm{del}(\mathrm{col}, \mathrm{row}) = p_0 + p_1 \cdot \mathrm{col} + p_2 \cdot \mathrm{col} \tag{6.8}$$

where the parameters p_0, p_1 and p_2 describe an initial offset and the slope of the delay in column and row direction respectively. In the third step this correction is then applied by calculating a corrected `TS1` value for each registered hit:

$$\mathrm{TS1}_{\text{delay-corr}} = \mathrm{TS1}_{\text{non-corr}} - \mathrm{del}(\mathrm{col}, \mathrm{row}). \tag{6.9}$$

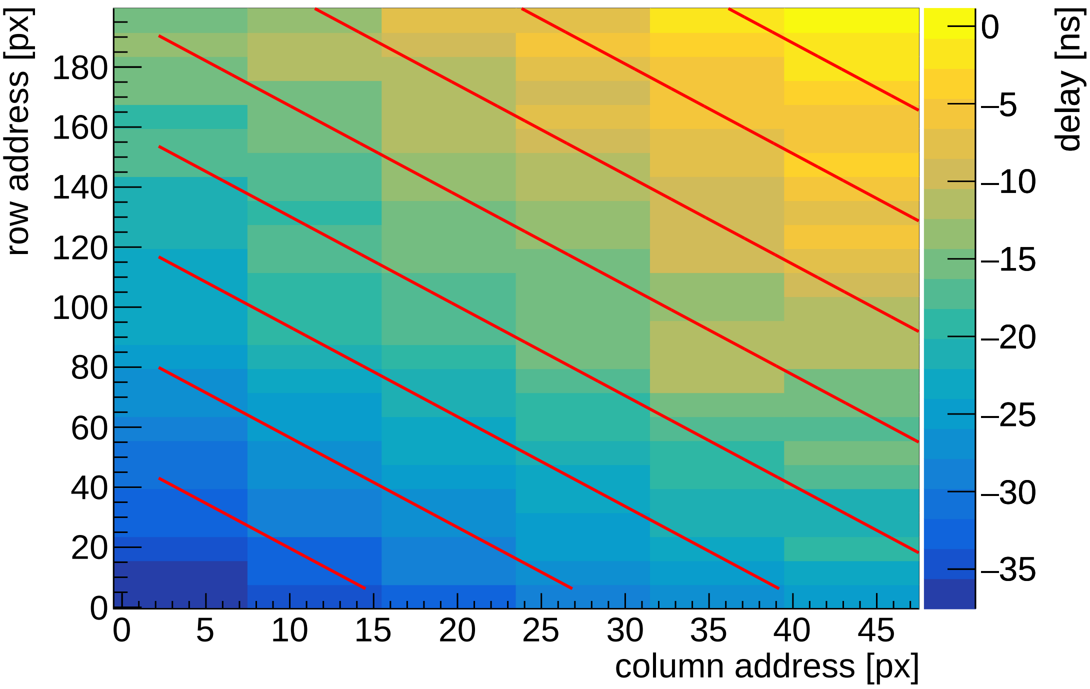

Figure 6.3: The pixel matrix of the MuPix8 is divided into 8×8 px super pixels and their delay is fitted with a 2D-linear function, whose equipotential lines are shown here.

Col and row describe the column and row of the superpixel in which the hit was registered. An example of the delays of the super pixels with equipotential lines of the fit is shown in Figure 6.3.

c) Time walk correction Another phenomenon which deteriorates the time resolution is the so-called time walk: Larger pulses in the pixels have a steeper rising edge and thus cross the threshold earlier than smaller pulses starting at the same instant. This is visualized in Figure 6.4a. To counteract this effect, two strategies are employed: Firstly, there is an on-chip correction mechanism using two thresholds, a high threshold `ThHigh` and a low one, called `ThLow`. A hit is counted only if its pulse crosses `ThHigh`, but `TS1` is sampled once the pulse rises above `ThLow`, which allows for `ThLow` to be placed much closer to the noise level than otherwise possible and to thus obtain a more accurate hit time information. This function is illustrated in Figure 6.4b.

The second strategy to mitigate this effect is in the analysis: From the measured time-over-threshold (ToT), a correlation between the delay (`TS1` and $\mathtt{T}_{\mathtt{REF}}$) and the ToT can be observed: The larger the ToT, the smaller the measured delay is. By taking the mean delay associated to each ToT value, one can then correct the `TS1` values accordingly when enough statistics are available.

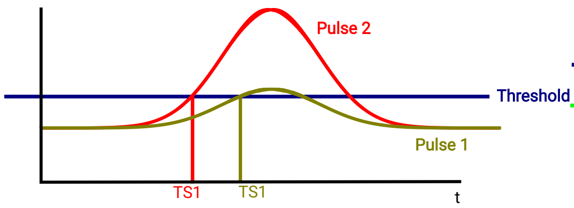

(a) Timewalk.

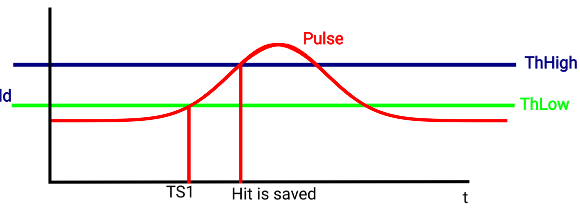

(b) `ThLow` and `ThHigh`.

Figure 6.4: A higher pulse generates an earlier `TS1`. This can be corrected by doing ToT measurements; the effect is reduced by sampling `TS1` at a lower threshold.

7 Temperature studies

During the testbeam, the Sr-90 irradiated sensor has been operated at temperatures of $-20\,°C$, $20\,°C$ and $40\,°C$. These are the temperatures measured at the chiller. Additionally, the inflow and outflow gas temperatures at the sensor case were measured (see Figure 7.1)

These registered temperatures are listed in Table 7.1.

To compare the testbeam data to results gained from simulations or to estimate the suitability of the cooling solution of the MU3E experiment, it is necessary to deduce the actual sensor temperature from these measurements. It can be inferred from the internal temperature diode of the chip, which needs to be calibrated first. This is a simple diode run in forward bias. According to an on-chip digital-analog-converter (DAC), different currents are successively passed through this diode and the voltage drop across it is measured. Hence, the I-V-curve gained from this data follows the Shockley-Equation [32, pp. 137 sqq.]:

$$I = I_S \left(\exp\left(\frac{V_D}{n \cdot V_T} \right) - 1 \right) . \tag{7.1}$$

This equation for the diode current depends on I_S, the reverse bias saturation current, the voltage across the diode, V_D, and the thermal voltage V_T multiplied by an emission coefficient n. This allows for a calibration of the temperature diode by recording multiple I-V-curves at different known temperatures. From this reference data, measured I-V-curves can then be mapped to actual temperatures.

Such a reference measurement was conducted in the laboratory at the PHYSIKALISCHES INSTITUT in Heidelberg at the end of October 2020: MU3E group-internal measurements using twelve different MUPIX8 chips found that at a current of $2\,\mu A$ flowing through the on-chip temperature diode, the voltage drop across said diode was very similar for all tested sensors: Across all measured values, a standard deviation of $\sigma_V = 0.9\,mV$ was encountered. In accordance with this data, the calibration of the temperature diode was done with a sensor different from the one used at the testbeam, the standard deviation calculated above will be used as an error for the gained calibration values.

Chiller temperature [°C]	Inflow temperature [°C]	Outflow temperature [°C]
−20	−12	−9
20	21	22
40	40[a]	—[a]

Table 7.1: Chiller temperatures vs. in- and outflow temperatures. The temperatures did not change over multiple measurements.
[a] The inflow temperature for $40°C$ was only measured once, the outflow temperature for $40°C$ was not measured at all, all other temperature measurements were taken continuously during the whole data-taking process.

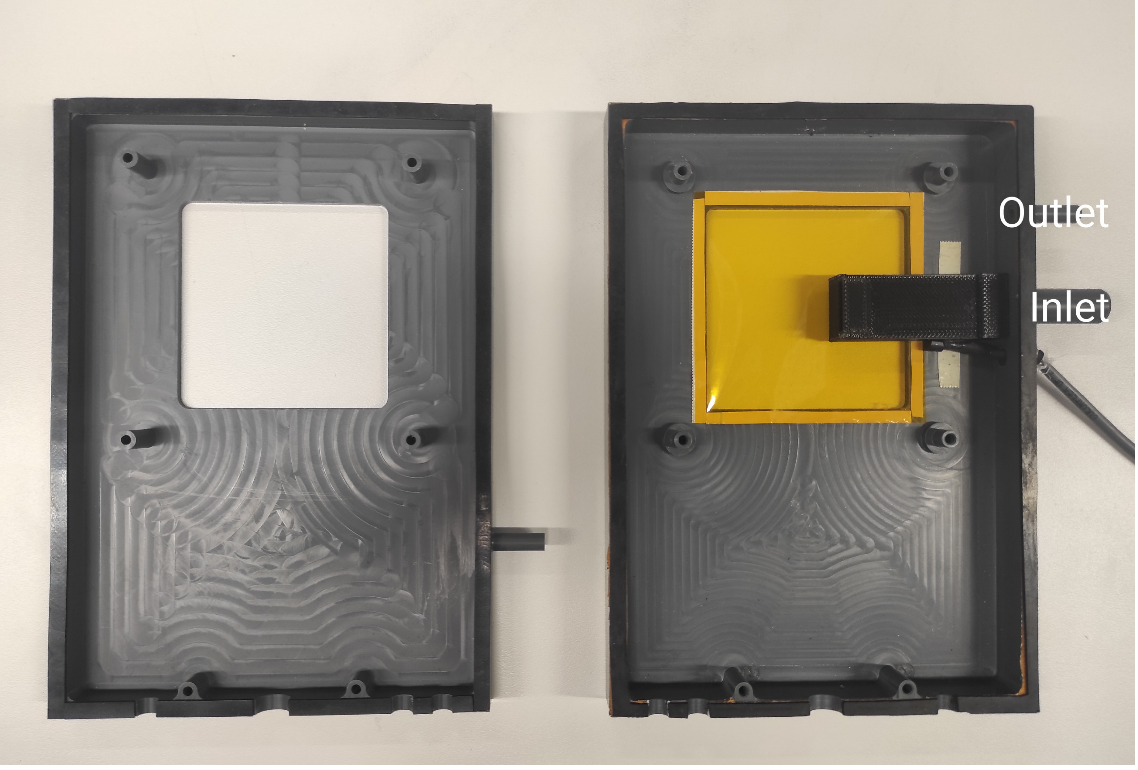

Figure 7.1: The cooling box used during the testbeam with chiller inlet and outlet positions.

The measurement principle largely follows the one laid out in [17, pp. 97 sqq.]: To determine a temperature reference, the sensor was placed in a Binder climate cabinet where the MuPix8 was placed on a ceramic plate to shield it from any electromagnetic interference from the climate cabinet. The cabinet was controlled via a LabView program which allows to set and read out its temperature. The temperature was cross-checked with an external Pt1000 thermometer. The thermometer as well as the MuPix8 power and readout cables were fed through a hole at the top of the cabinet which was then sealed from the outside, to shield the inside from heat exchange with the laboratory.

The climate cabinet's temperature was used as a reference temperature and the voltage drop across the diode at a current of 854 nA (corresponding to a DAC setting of `0xdac0`) was measured and plotted against the reference temperature. As the same current value was measured at the testbeam, this allows for a straight-forward calibration of the actual chip temperature.

Part III

Measurements and Results

8 Temperature diode calibration

Following the procedure laid out in section 7, the voltage drop across the temperature diode was measured at temperatures from −20 °C to 80 °C in steps of 5 °C. For this measurement, the sensor with the ID 265-3-9 was used. The chip was not powered on so that it does not dissipate heat on its own, affecting the measurement. The temperature diode was externally connected and powered by a power supply which also recorded the voltage drop across the diode.

The calibration curve gained from this measurement is shown in Figure 8.1. From the fit parameters of the linear temperature fit seen in this calibration curve, the following formula can be derived:

$$T_{\text{MuPix8}} = 312.198°\text{C} - V_{854\text{nA}} \cdot 0.474 \frac{°\text{C}}{\text{mV}} \tag{8.1}$$

The calibration curve was double-checked at three data points with the actual irradiated sensor with the ID 265-3-6. The results matched within 1 mV, which indicates that according to Equation 8.1, the calibration is off by less than 0.5 °C.

During the testbeam, an automated I-V-scan of the temperature diode was conducted after every *run* – a self-contained data-taking unit in which about 500 MB of data are gathered and which takes about one to three minutes. There were 450 runs conducted at −20 °C chiller temperature, 195 runs at 20 °C and 225 runs at 40 °C.

As the sensor temperature is assumed to be constant over these runs, the voltage measurements of all runs at one temperature are averaged and used to deduce a temperature from Equation 8.1. The result of this calibration is shown in Table 8.1. The actual voltages of the temperature diode at a diode current of 854 nA (i.e. the reference current used for calibration) which were measured at the testbeam are displayed in Figure 8.2. One can observe that the temperature was quite stable at all times. It can be seen, that the chiller was first set to −20 °C, then to 20 °C and the final measurements were conducted at 40 °C.

Chiller temperature [°C]	Calibrated chip temperature [°C]
−20	29.93 ± 1.37
20	60.76 ± 1.27
40	79.69 ± 1.32

Table 8.1: The MuPix8 temperatures calculated using Equation 8.1.

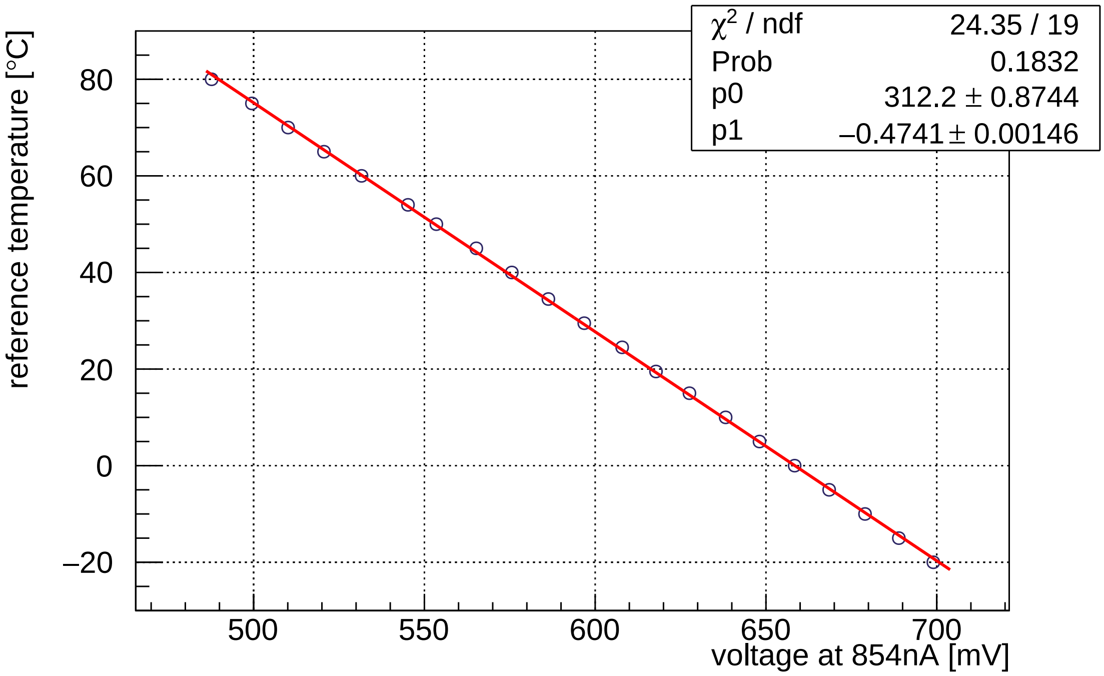

Figure 8.1: The temperature calibration curve recorded with the MuPix8 with ID 265-3-9.

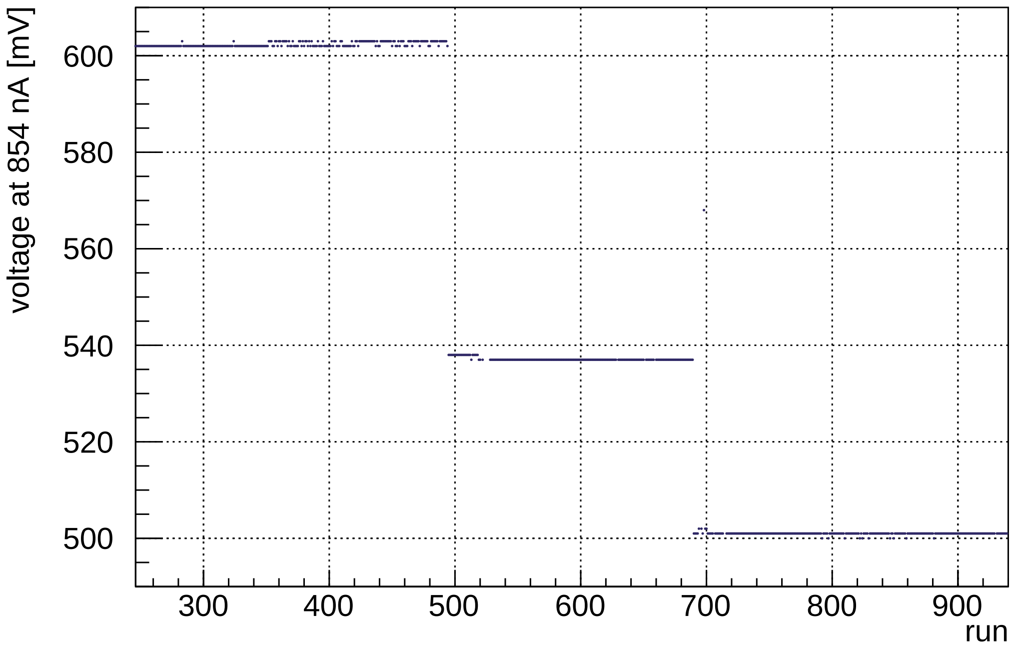

Figure 8.2: The voltage drop across the temperature diode at the testbeam.

9 Unirradiated reference data

The electron-irradiated sensor examined in this thesis was neither characterized before its irradiation, nor was data taken to conduct the appropriate characterization. There are however two clues to estimate its original performance: The performance of other MuPix8 sensors (section 9.1) and the performance of the irradiated sensor when it was used as a reference layer to test other sensors (section 9.2).

9.1 Performance of unirradiated MuPix8 sensors

An extensive study of over 20 MuPix8 sensors was conducted in [14, pp. 146 sqq.]. A study testing the efficiency of these sensors shows that there is quite a variation in-between different sensors based amongst others on thickness, substrate resistivity and production batch at identical settings. It was additionally shown that sensors from the same wafer seem to behave similarly. It was also proven that the sensors with a substrate resistivity of 200 Ω cm show a larger high efficiency plateau than those with a resistivity of 80 Ω cm and that thinning does not degrade the sensor performance.

The irradiated sensor studied in this thesis is thinned down to 100 µm and has a substrate resistivity of 200 Ω cm. It was on wafer 18 for which [14] does not provide any reference data.

9.2 The investigated sensor before its irradiation

The sensor investigated here was, although not characterized on its own, used as a reference layer (see section 6.1) when studying other sensors. From this dataset some information can be inferred. The sensor being used as a reference plane means its parameters were not changed, so threshold-dependent values are not available, but there are benchmark values for a threshold of 51 mV above the baseline (the threshold voltage the sensor was run at when used as a reference). This is lower than the thresholds set at the irradiated sensor for most of the measurements. However, as the data indicates a shift of the working range anyways (see chapter 11), the data is comparable.

The reference dataset was chosen such that the DUT (which now acts as a reference layer for the characterized sensor) was run at similar settings to those used for the reference layers in the actual testbeam with the irradiated sensor to get the most sensible data. The parameters gained this way are summarized in Table 9.1. These results are all well within the specification for the final Mu3e experiment: An efficiency of 99 % or higher while having less than 20 Hz/px noise at the same time, and an uncorrected time resolution of below 20 ns [2, p. 39].

As the efficiency (and thus presumably also other main sensor characteristics) differs from chip to chip (see section 9.1) this data will also be used to assess the performance degradation after the irradiation.

Parameter	Value
Efficiency	99.93 %
Clustersize	1.36 px
XT-corrected clustersize	1.04 px
Noise-rate	0.004 Hz
uncorrected time resolution	(14.90 ± 0.01) ns
run-corrected time res.	(14.90 ± 0.01) ns
delay-corrected time res.	(13.91 ± 0.01) ns[b]

Table 9.1: Results of the unirradiated sensor at a threshold of 51 mV

[b] ToT-correction was not possible due to it not being correctly sampled, see also section 11.8.

10 The irradiation process

Over the course of 34 days ($(809.5 \pm 0.4)\,\mathrm{h}$), one MuPix8 sensor was exposed to a strong Sr-90 source. During this irradiation, the current flow/power consumption of the chip was recorded and will be examined in the following chapter.

Monitoring the power consumption of the chip is of importance as the maximum power draw is imposed by cooling restrictions in the final experiment. The specification requires a power consumption of no more than $350\,\mathrm{mW/cm^2}$ [2]. The cooling solution is designed to be able to handle a setup dissipating $400\,\mathrm{W/cm^2}$, but a power consumption of around $250\,\mathrm{W/cm^2}$ is desired.

As the results presented in the following sections show that the power consumption increases after radiation exposure, this poses even tighter restrictions on the initial power consumption. On the other hand, the following results show that the power consumption goes down again after the sensor being turned off for a period of time (even while still being subject to irradiation). This effect could allow the development of strategies to make sure that the power consumption stays within certain boundaries.

10.1 Calculating the radiation dose

There are generally two data sources to infer information on the dose seen by the detector from: One approach is to analyze the Sr-90 source directly and to calculate the amount of radiation seen by the detector from its characteristics and the geometry of the setup. The other method is to make use of the data recorded by the chip during the irradiation.

In the following section, both approaches will be explored and their results will be compared. It is currently planned to do an extensive simulation of the source with its actual geometry to gain more exact results [27]. As these results are not available yet, only an estimate will be given.

In the following two sections, a number of electrons expected to be seen by the detector will be derived from the data of the Sr-90 source as well as from the data recorded by the sensor during the irradiation. In section 10.1.3 the actual dose deposited in the detector will be calculated from these figures.

10.1.1 The Sr-90 source

Sr-90 is a strontium isotope with a half-life of $(10\,522 \pm 27)\,\mathrm{d}$ [3, p. 327] and the irradiation lasted for $(809.5 \pm 0.4)\,\mathrm{h} = (33.729 \pm 0.017)\,\mathrm{d}$. This allows to calculate the activity loss of the source during the irradiation: The activity of a radioactive source is described by the following set of equations:

$$A(t) = -\frac{\mathrm{d}N}{\mathrm{d}t} \tag{10.1}$$

$$N(t) = N_0 \cdot \exp\left(-\lambda t\right) \tag{10.2}$$

$$\lambda = \frac{\ln(2)}{T_{1/2}} \tag{10.3}$$

so that

$$A(t) = \lambda \cdot N_0 \cdot \exp\left(-\ln(2)\frac{t}{T_{1/2}}\right) = A(0) \cdot \exp\left(-\ln(2)\frac{t}{T_{1/2}}\right). \tag{10.4}$$

In these, A is the Activity of an active material with N atoms, t is the time, λ is the decay constant and $T_{1/2}$ is the half-life of the material. According to this, the relative loss in activity is given as:

$$\frac{A(0) - A(t)}{A(0)} = 1 - \exp\left(-\ln(2)\frac{t}{T_{1/2}}\right) \tag{10.5}$$

and the relative activity loss is

$$\left.\frac{A(0) - A(t_{\mathrm{end}})}{A(0)}\right|_{\text{Sr-90 irrad of MuPix8}} = (0.2219 \pm 0.0006)\%. \tag{10.6}$$

Therefore the activity will be assumed to be constant in the following calculations.

The nominal activity of the strontium source that was used is given as 74 MBq on 18.12.2014 [24]. Equation 10.4 allows to calculate the activity of the source at the start of the irradiation (24.05.2019), which is 1 618 days after the reference date:

$$A(24.05.2019) = 74\mathrm{MBq} \cdot \exp\left(\frac{1\ 618}{10\ 522}\right) = 66.5\mathrm{MBq} \tag{10.7}$$

The active material is directly and fully enclosed inside the source. In the outlet direction, the material is shielded by a 50 µm thick stainless steel window. The internal design of the source influences the emitted energy spectrum: Reflections in the enclosing material as well as absorptions in the window play a role here. To simplify the following computations, all internal reflection and scattering effects will be ignored.

The nominal activity is the activity of the whole material placed in the source. That means this activity would be measured across a solid angle of 4π sr. The irradiated sensor however only occupies a fraction of that angle. To compute this fraction, some simplifications will again be employed:

The source was mounted 1.5 cm above the sensor. To estimate the fraction of the solid angle taken up by the chip, a calculation as outlined in Figure 10.1 will be done: The fraction of the angle taken up by the sensor will be estimated as

$$p = \frac{A_{sensor}}{A_{sphere}} \tag{10.8}$$

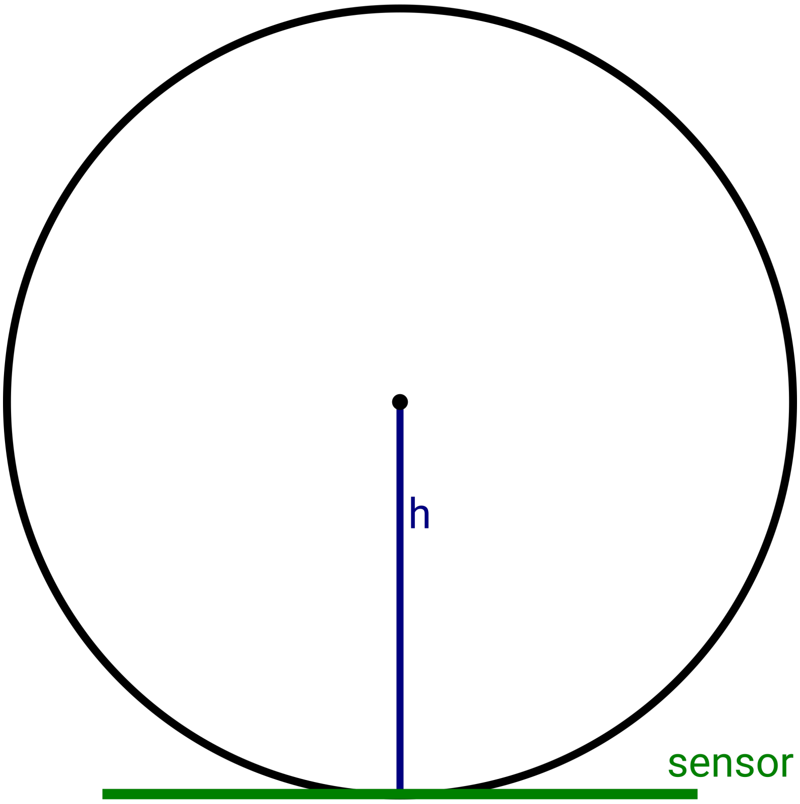

Figure 10.1: A two-dimensional sketch of the geometry which is used to estimate the activity registered by the sensor.

where the sphere has radius of 1.5 cm and A_{sensor} describes only the active pixel matrix. According to basic geometry, the following holds:

$$A_{sphere} = 4\pi \cdot h^2 = 28.27\text{cm}^2 \tag{10.9}$$

$$A_{sensor} = (n_{cols} \cdot 80\text{µm}) \cdot (n_{rows} \cdot 81\text{µm}) = 0.62\text{cm}^2. \tag{10.10}$$

Hence,

$$p = \frac{A_{sensor}}{A_{sphere}} = 2.2\% \tag{10.11}$$

which means that 2.2 % of the electrons emitted by the source actually hit the sensor. Going one step further, the number of electrons hitting the sensor can then be calculated using the irradiation-time $t = (809.5 \pm 0.4)$ h as

$$N_{e^-,\text{total}} = A \cdot t \cdot p = \big((66.5 \cdot 10^6) \cdot (809.5 \cdot 3600) \cdot 0.022\big) \approx 4.26 \cdot 10^{12}. \tag{10.12}$$

10.1.2 Data from the detector

Figure 10.2 shows the hit-rate registered by the MuPix8 during the irradiation in spring 2019: To save disk space, an automated measurement lasting 10 s was started every 300 s. From this data a hit-rate can be deduced. As the figure of interest is

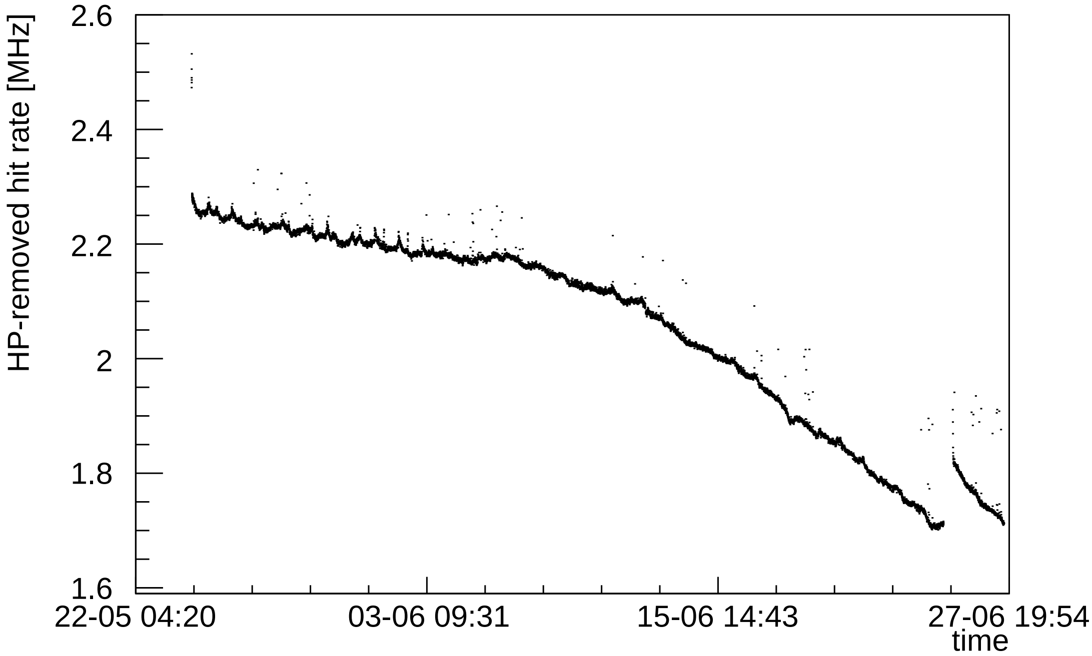

Figure 10.2: The hit-rate registered by the MuPix8 during the irradiation after the removal of hot pixels.

the actual number of particles and the detector performance is not studied at this point, the data from hot pixels was completely discarded and their hit count was set to 0. For this step a pixel is defined as a hot pixel once it registered 3 times as many hits as the average pixel (for each 10-second-measurement anew).

This means that the hit-rate is underestimated in the following computation. An upper boundary on this underestimation can be set by the following calculation (whose assumptions will be justified just afterwards): On average, 5.2 hot pixels per 10-second-measurement were detected (the evolution of the number of hot pixels is shown in Figure 10.3a). If the actual hit-rate of the hot pixels is assumed to be around the level of the other pixels, it holds that (with a pixel matrix size of $48\,\mathrm{px} \times 200\,\mathrm{px}$), the hit rate is underestimated by no more than:

$$N_{\text{pixels, removed}}/N_{\text{pixels, total}} = \frac{5.2}{48 \cdot 200} = 0.05\%. \tag{10.13}$$

As can be seen from Figure 10.3a, the amount of hot pixels increased over the time, while the hit-rate decreased (the non-adjusted hit-rate also decreased in roughly the same manner, so this effect is not due to the hot-pixel removal). This shows that the actual underestimation is lower than the boundary calculated above. From Figure 10.3b, the assumption of equally distributed hit-rates is justified.

From the knowledge, that the activity of the source only decreased by a negligible amount ($< 1\%$) and taking into account that Figure 10.2 shows a significant rise in the hit rate after the sensor was powered off it becomes apparent, that the drop in the hit rate is not due to a reduced particle rate but rather due to a shift in the operating point of the sensor. The results show that the detector did, even after

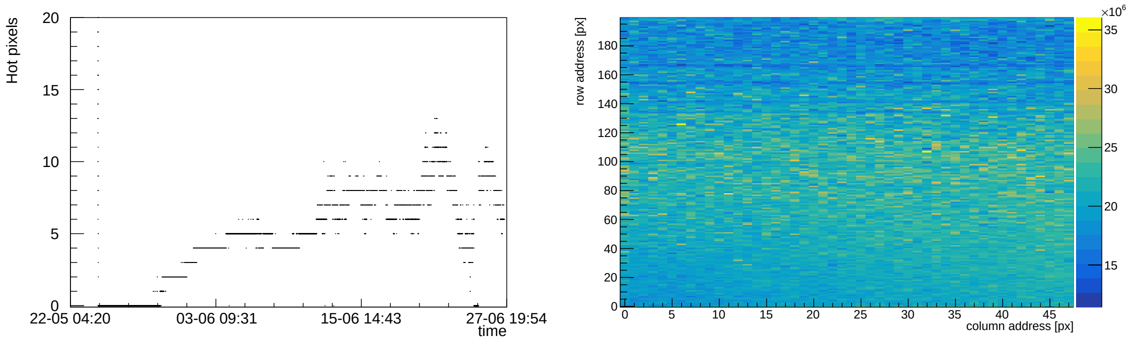

(a) Number of hot pixels.

(b) Accumulated hitmap.

Figure 10.3: The number of removed hot pixels and an accumulated hitmap of all measurements conducted during the irradiation process.

irradiation, have an efficiency of above 99 % (see section 11.4) so this rate decrease is not due to an efficiency drop either.

During the first few days, fluctuations due to open blinds and the light sensitivity of the sensor can be seen. As the interesting quantity is however the number of electrons from the Sr-90 source, these regularly appearing peaks have to be ignored and the baseline value has to be determined. For further analysis, the average value of the first night (for this purpose defined as the time between 11pm and 4 am) which is at 2.25 MHz will be assumed as the rate for the whole irradiation period. As the sensor has an efficiency of over 99 % (see section 9.2 for measurements before, section 11.4 for results after the irradiation), for the further calculation there is no correction done for sensor inefficiencies and the measured rate is assumed to be the source's β rate.

This allows a first calculation: The detector was exposed to the Sr-90 source for (809.5 ± 0.4) h, this means the pixel matrix part of the detector was hit by

$$N_{e^-,\mathrm{total}} = f \cdot t = 2.5\,\mathrm{MHz} \cdot (809.5 \pm 0.4)\,\mathrm{h} = (6.557 \pm 0.003) \times 10^{12} \tag{10.14}$$

electrons.

10.1.3 Dose calculation

The Berger-Seltzer formula – in the following, the formula based on experimental data as given in Equation 3.3 will be used with appropriate interpolation – describes the amount of energy $\mathrm{d}E$ deposited by an electron after traveling a distance $\mathrm{d}x$ as a function of the particle's kinetic energy. This is of course a statistical process, so what is really given is the *mean* energy deposition $\langle \frac{\mathrm{d}E}{\mathrm{d}x} \rangle$.

Obviously, as a particle travels through matter, it loses energy, so the stopping power $\frac{\mathrm{d}E}{\mathrm{d}x}$ changes over the distance traveled. This means, the energy of an incoming particle (with an initial kinetic energy of E_0) after passing the distance Δx can numerically be approximated as

$$E_1 := E(\Delta x) = E_0 - \left.\frac{\mathrm{d}E}{\mathrm{d}x}\right|_{E_0} \cdot \Delta x. \tag{10.15}$$

This procedure can then be repeated:

$$E_2 := E(2\Delta x) = E_0 - \left.\frac{\mathrm{d}E}{\mathrm{d}x}\right|_{E_0} \cdot \Delta x - \left.\frac{\mathrm{d}E}{\mathrm{d}x}\right|_{E_1} \cdot \Delta x = E_1 - \left.\frac{\mathrm{d}E}{\mathrm{d}x}\right|_{E_1} \cdot \Delta x. \tag{10.16}$$

One ultimately arrives that after traveling a distance d it has an energy of

$$E(d) = E_0 - \sum_{i=0}^{n-1} \left.\frac{\mathrm{d}E}{\mathrm{d}x}\right|_{E_i} \cdot \Delta x, \tag{10.17}$$

where $n = \frac{d}{\Delta x}$.

This information can be used to numerically calculate a *Bragg-curve*, which shows the stopping power as a function of the absorber depth [20, p. 119]. Working with a discretized problem anyways, multiplying the stopping power by Δx then yields a curve showing the energy deposited in the detector as a function of its depth measured from the electron's entry point. Integrating (i.e. in the discrete case: summing) over this curve then yields (depending on the integration interval) the average energy deposited by one electron in the detector or a part thereof:

$$E_{deposit}(E_0) = E(d) - E_0 \tag{10.18}$$

Of course the Bragg curve depends on the initial electron energy E_0. This means that for a proper analysis not only the detector thickness has to be discretized but also the emission energy spectrum: The interval of kinetic energies emitted by the source ranging from $E_{emission,min}$ to $E_{emission,max}$ defines the possible values of initial electron energies entering the detector material (here, energy losses in the air between the source and the detector are neglected; these errors are discussed later).

Discretizing the above mentioned interval leads to energy deposition curves for initial energies $E_0^1, \ldots, E_0^m$ where m is the number of divisions of the energy emission interval $[E_{emission,min}, E_{emission,max}]$.

Based on this it is now possible to calculate the energy deposited in the detector material based on the initial energy of the particle $E_{deposit}(E_0^j)$, $j \in 1 \ldots m$. To get a figure for the average energy deposited in the detector by a single electron originating from the source, the energy depositions of all possible initial energies have to be summed up, weighted by the emission spectrum of the source:

$$E_{deposit,average} = \sum_{j=1}^{m} E_{deposit}(E_0^j) \cdot w(E_0^j). \tag{10.19}$$

In the discrete case, the weights $w(E)$ are chosen so that

$$\sum_{j=1}^{m} w(E_0^j) = 1 \tag{10.20}$$

and that each weight corresponds to the relative emission probability of a particle of its respective energy by the source.

The quantity gained this way is of purely statistical nature. As during the MuPix8 irradiation $> 10^9$ particles were registered, it is safe to assume that the

	Energy deposition [10^{11} MeV]		Dose [kGy]	
	whole chip	electronics	whole chip	electronics
Source data	2.44	0.37	2.70	2.69
Sensor data	1.59	0.24	1.75	1.75
average	2.01	0.30	2.22	2.22

Table 10.1: The total irradiation dose seen by the MuPix8 during the irradiation campaign. *Electronics* indicates the first 15 µm of detector material.

calculations done above are statistically sound. To actually get a figure for the total energy deposited in the detector over the irradiation period, the following calculation is sufficient:

$$E_{deposit,total} = E_{deposit,average} \cdot N_{e^-} = E_{deposit,average} \cdot f \cdot t, \tag{10.21}$$

where N_{e^-} is the number of electrons seen by the detector calculated as a product of the hit rate f and the irradiation time t. By modifying the summation range in Equation 10.17, it is possible to calculate the energy deposited in only a part of the detector.

Finally, the results need to be converted to a radioactive dose usually given in the unit of 1 Gy = 1 J/kg for proper comparability. For this calculation, a sensor density of $\rho = 2.33\,\mathrm{g/cm^3}$ is assumed, which is equal to the density of pure silicon[29]. This assumption is justified because the sensor is mostly made of silicon and the very similar density of silicon oxide ($\rho_{SiO_2} = 2.27\,\mathrm{g/cm^3}$ [30]) does not meaningfully alter the overall mass.

The mass of the pixel matrix A of a MuPix8 chip is then given as

$$m_{\text{MuPix8}} = (48 \cdot 80\,\mu\mathrm{m}) \cdot (200 \cdot 81\,\mu\mathrm{m}) \cdot 100\,\mu\mathrm{m} \cdot \rho = 14.5\,\mathrm{mg} \tag{10.22}$$

and the dose can be calculated as

$$D = \frac{E_{deposit}}{m_{\text{MuPix8}}}. \tag{10.23}$$

Results

The calculations discussed above were conducted using a number of divisions for the detector thickness and the energy spectra of $n = m = 250\,000$. The emission spectrum of the source was reconstructed according to data from [10, p. 1242] and is depicted in Figure 10.4. Using the number of electrons calculated in sections 10.1.1 (data from the source) or 10.1.2 (data from the detector) respectively, one gets the results shown in Table 10.1. As the TID effects mostly affect the in-silicon electronics, which are only placed in the topmost 15 µm of the chip, the energy deposition in that part of the chip is also calculated. These values are the ones labeled *electronics* in Table 10.1.

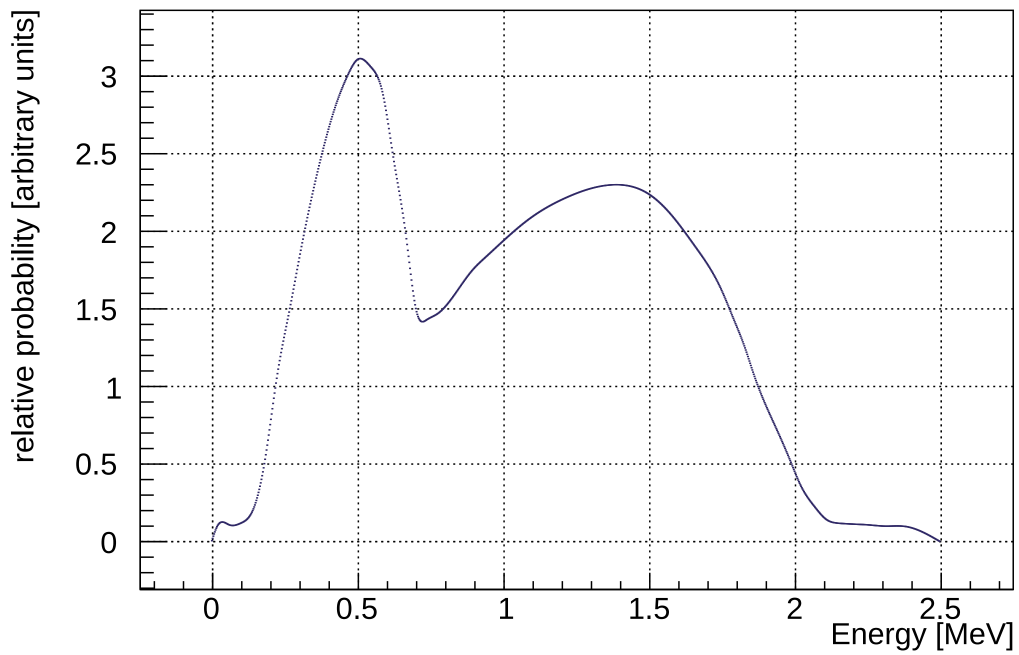

Figure 10.4: The assumed emission spectrum of the Sr-90 source reconstructed from [10, p. 1242].

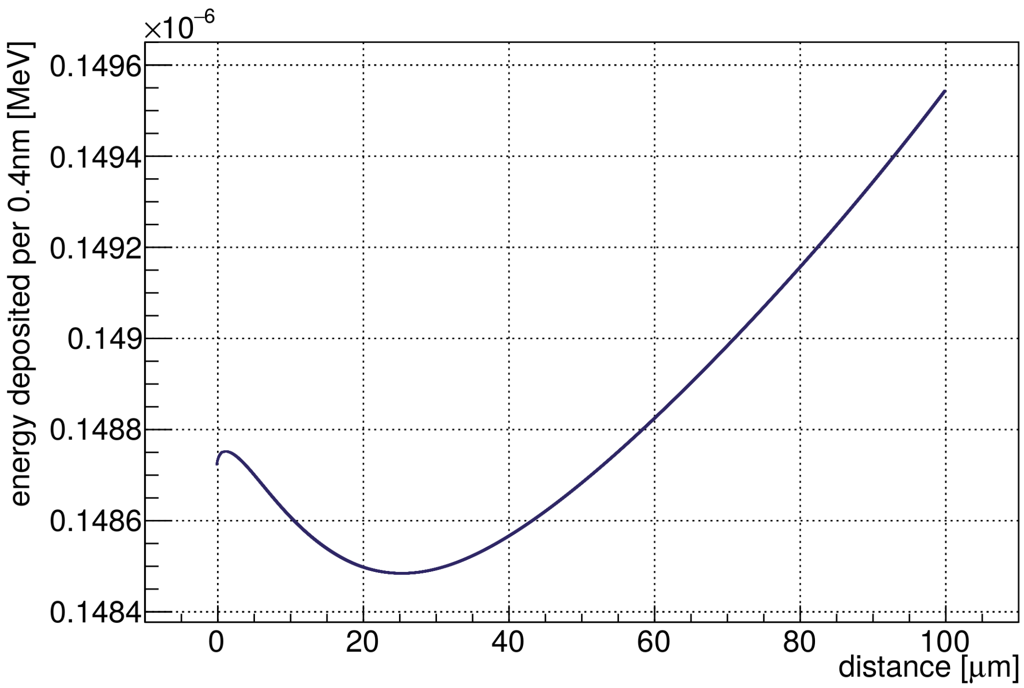

Figure 10.5: The average energy deposition in the detector material by a single particle.

Error discussion

The dose determination process is based on a series of assumptions that introduce uncertainties in the gained results. The most notable effects are:

The emission spectrum The energy spectrum of the electrons entering the detector material is not exactly known for mainly two reasons: The energy loss of electrons between the source and the detector is not accounted for. This imposes a lower boundary on the initial energy E_0 because:

- The source has a thin stainless steel shield in front of it which low-energy electrons cannot pass.
- A protective cap with Kapton tape is placed between the sensor and the source which again cannot be passed by very low-energetic electrons.
- Electrons of very low energy lose momentum in the air between the source and the detector.

These effects are especially important for electrons with low energy as their Bragg peak is inside the detector material (i.e. they deposit all their energy). For electrons with higher energy, the energy loss is to a good approximation constant. Therefore, the above-mentioned points do not play as much of a role when looking at the energy deposition.

On the other hand, the number of electrons actually exiting the source is hard to predict, especially in relation to their energy. Inside the source, reflections and scattering can happen. These effects may also happen at the shield in front of the source which further limits predictability.

Angular effects The above assumes in the deduction of Equation 10.18 that all particles hit the chip perpendicularly. This is generally not the case. To take this into account, a geometric discussion about the setup and the exact relative positioning of the chip in regard to the source would have to be made.

Geometric simplifications The geometry of the problem was greatly simplified: The source is assumed to be a point with no spatial extension and the fraction of the solid angle of the source emission taken up by the sensor as calculated according to Figure 10.1 differs from the real value.

10.2 HV leakage current during the irradiation

Figure 10.6 shows the HV leakage current during the irradiation campaign which was conducted in May – July 2019. During the irradiation the HV was set to $-50\,\text{V}$.

As the HV current is directly proportional to the number of registered hits, the light sensitivity of the chip or respectively the day/night cycle can be observed until 03.06.2019 after which the blinds in the room where the irradiation setup was placed were shut. Afterwards smaller pulses following a daily pattern can be seen

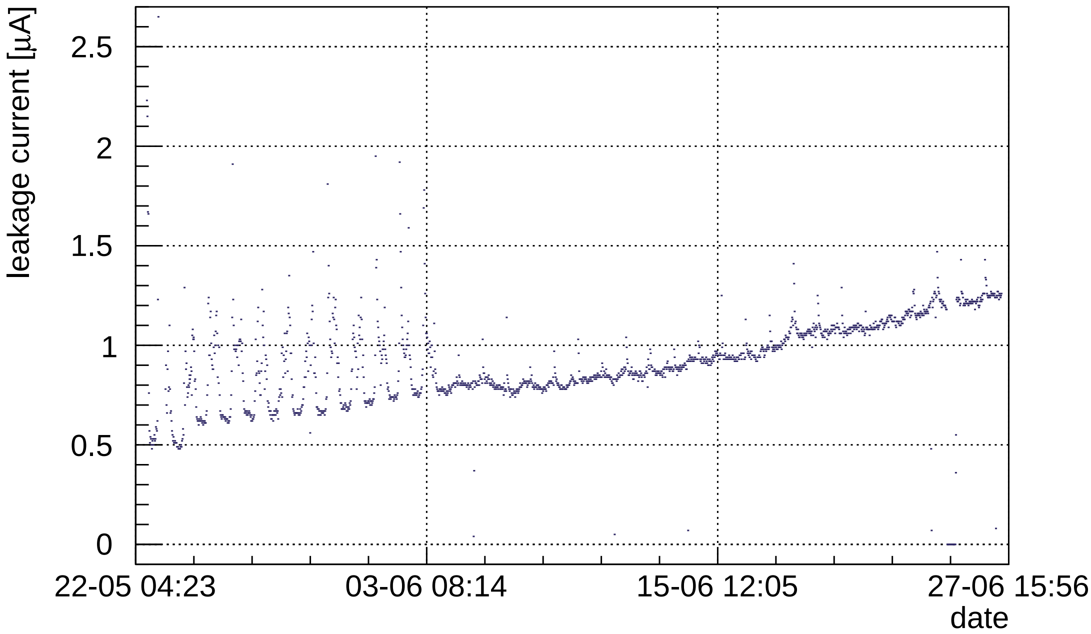

Figure 10.6: The HV ($-50\,\mathrm{V}$) current flow during the irradiation in May to July 2019. Until the beginning of June, day/night cycles can be seen.

each day at around 5:30 pm. Additionally, the power outage from around 03:20 am to 11:25 am on 25.06.2019 can be very well seen. After this power shutdown, no significant change in the HV current flow can be observed – the time after the power outage is too short to conclude with certainty whether the current increase continues.

What is more interesting though is the steady rise in HV current over time regardless of the day/night cycles. This is emphasized in Figure 10.7 where at each time stamp the average current flow of the surrounding twenty-four hour window is plotted. In absence of external light sources (i.e. in the time from 03.06. – 24.06.2019) a current increase of about $0.4\,\mu\mathrm{A}$ can be observed.That this effect was in fact caused by the irradiation was proven by the reference measurement: As shown in Figure 10.8, the leakage current did not increase during the reference measurement without a radioactive source nearby.

10.3 Bias voltage power during the irradiation

As shown in sections 10.2 and 11.2 the HV current does not significantly affect the power consumption in comparison to the low voltage (LV) components. Therefore, it is important to monitor how these components behave under exposure to irradiation. During the irradiation, the chip was externally powered using a HAMEG HMP4040. The three bias voltages VDDD, VDDA and VSSA were all individually applied and the respective current flows were monitored and recorded. This allows for a detailed investigation of their behavior which is depicted in Figures 10.9 to 10.12:

Figures 10.9 and 10.10 show that VDDA and VDDD behave quite similarly:

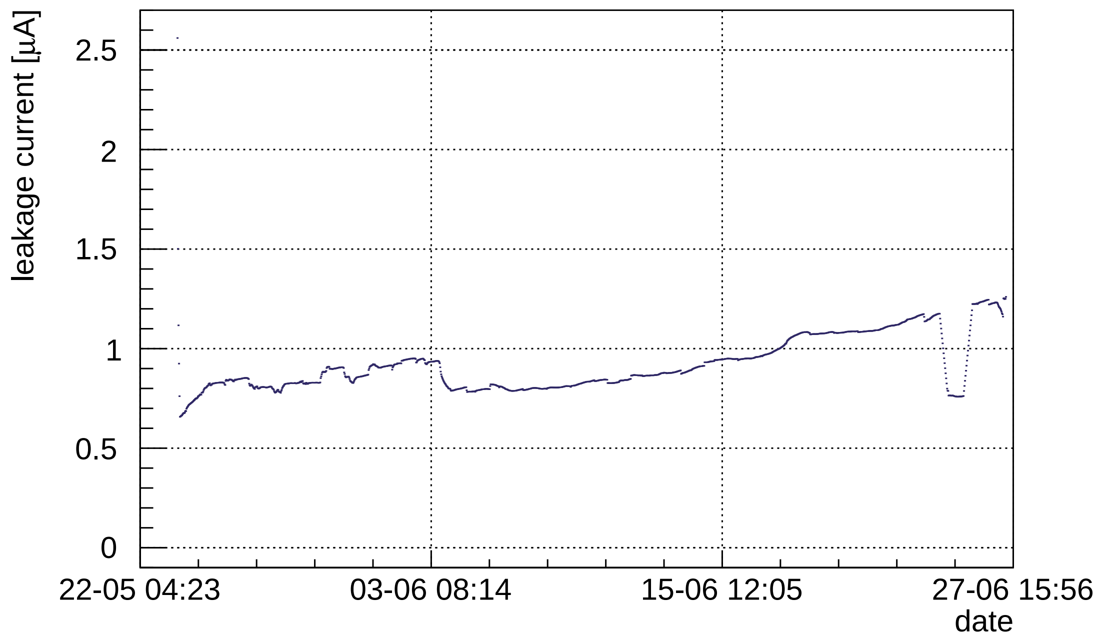

Figure 10.7: The average HV current flow over a 24h sliding window during the irradiation in May to July 2019. At the beginning of June a drop can be seen corresponding to the blinds being permanently closed.

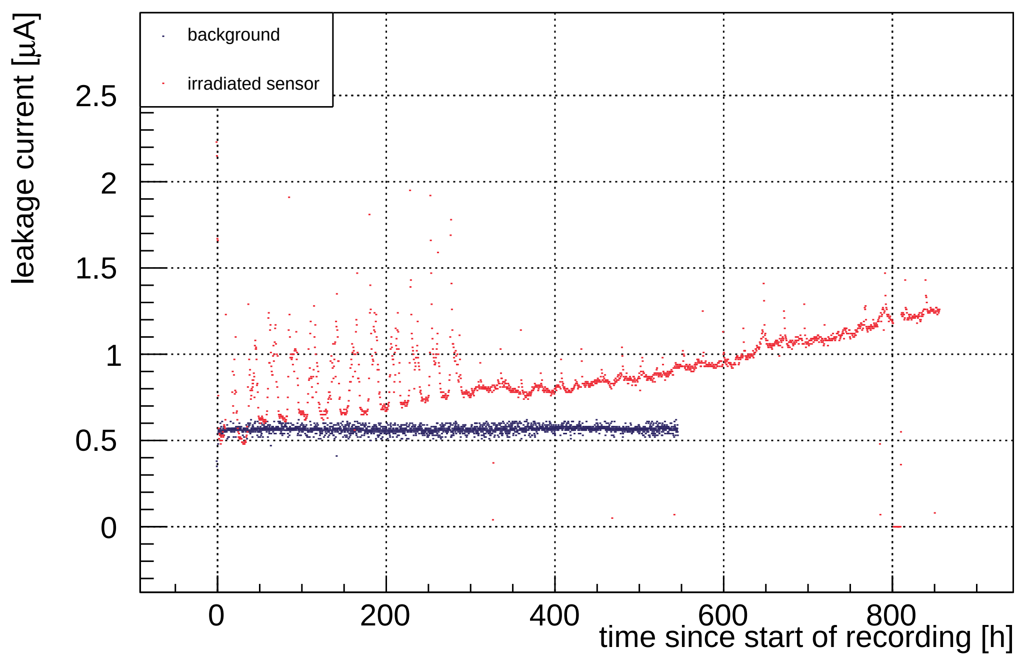

Figure 10.8: During the reference measurement in October 2020, the leakage current did not rise.

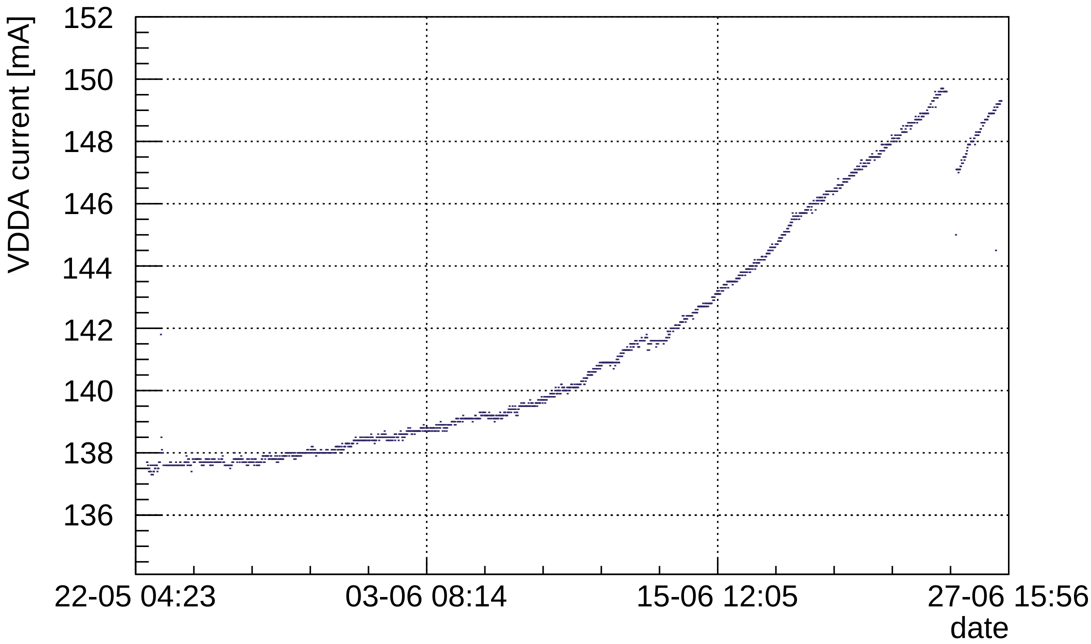

Figure 10.9: The VDDA current during irradiation.

After a phase of 13 days (VDDD) or 7 days (VDDA) respectively, the currents start to increase after staying at essentially the same level beforehand. After the power-off a significant drop in the current flow can be observed.

The VSSA current however behaves wholly different: It rises by about 2 mA during the first 15 days of irradiation and then saturates. Because the overall current is quite low it can be seen, that the discretization given by the measurement resolution of the power supply is observable in Figure 10.11. Therefore, it is hard to judge from this data whether the drop seen after the power outage is actually significant and whether an actual plateau is reached or if the current starts to increase again after staying at said plateau for another 15 days.

10.3.1 Relaxation effect

On the 25th June 2019 at 02:44 am, a power outage happened at the institute which caused the irradiation setup to be unpowered until the outage was fixed 9 h later. It can be seen that this caused the power consumption of the bias voltages to significantly decrease after being turned on again: The VDDA-current dropped from (149.6 ± 0.0) mA to (147.1 ± 0.0) mA while the VDDD-current dropped from (97.5 ± 0.0) mA to (95.6 ± 0.0) mA.

This effect is – while small in absolute values – significant in its nature and requires further study to properly assess its reproducibility and to obtain a statistically sound quantitative value for the relaxation effect. This is necessary as the observed behavior indicates that controlled detector shutdowns can decrease the overall power consumption. Due to e.g. work being done on the beam, shutdowns

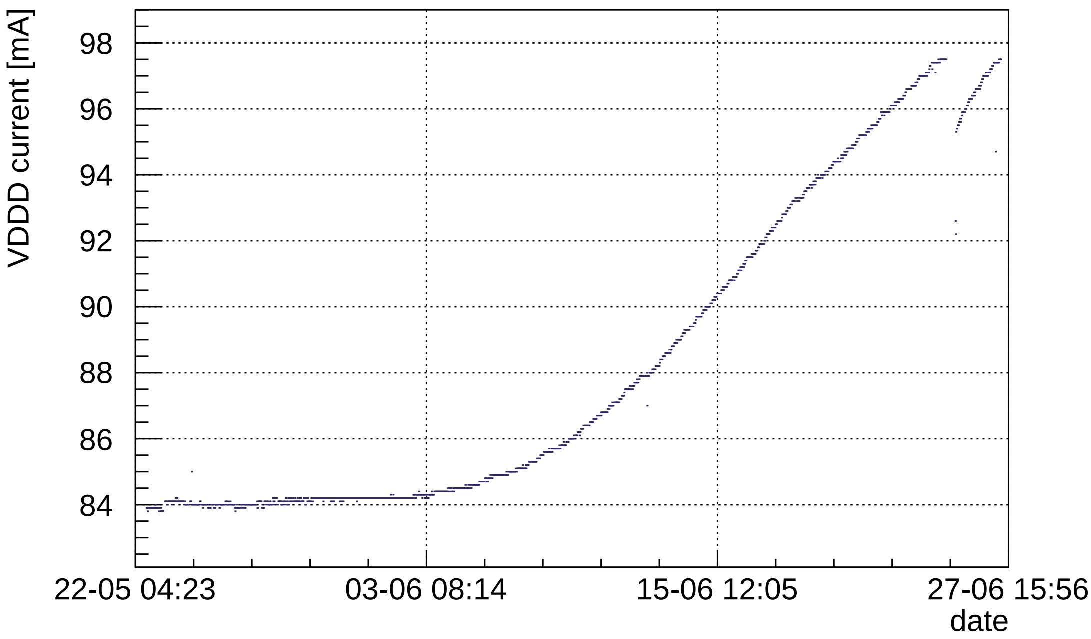

Figure 10.10: The VDDD current during irradiation.

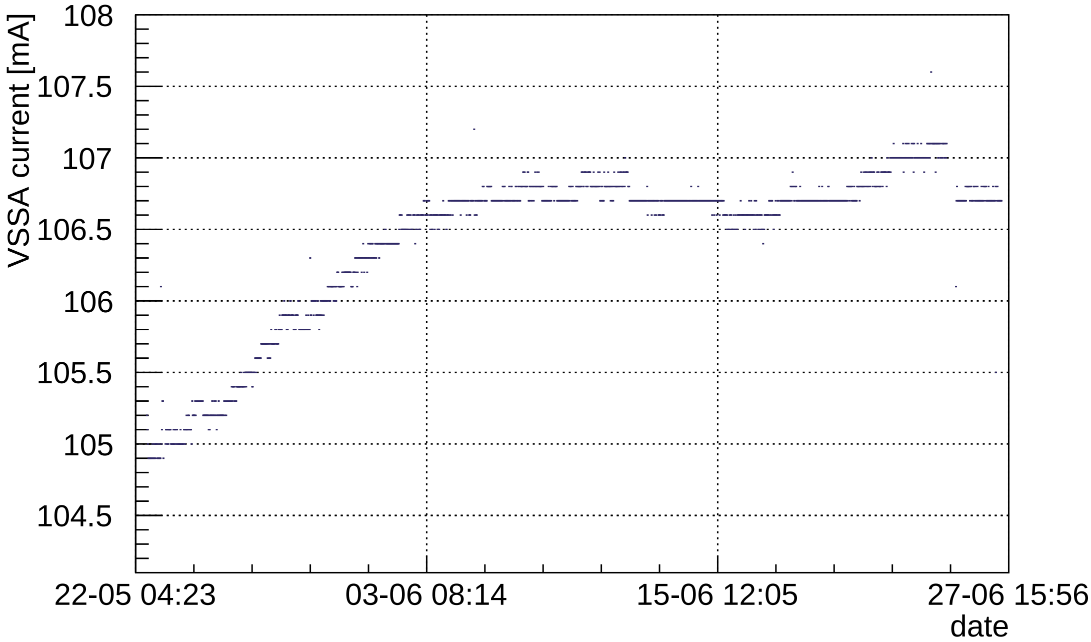

Figure 10.11: The VSSA current during irradiation.

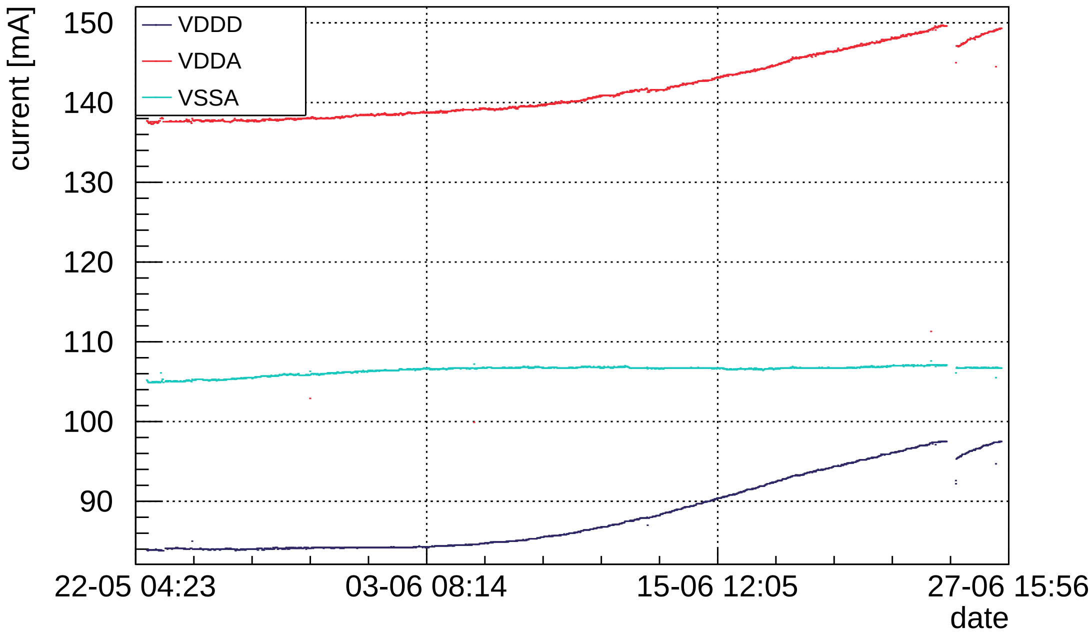

Figure 10.12: All LV currents during the irradiation.

are foreseen to happen during the final experiment. Fully investigating and understanding this effect allows these controlled shutdowns to be planned to minimize power consumption and thus the heat dissipated by the chip.

In the same vein more detailed temperature studies could prove useful: The chips do not heat up evenly. A detailed study on regional heating effects and the relaxation effect could give more insight into whether the cooling solution is sufficient or if there is the need for some modification.

The indication that the current increase is caused by the electron irradiation is confirmed not only by the relaxation effect described above but also by the background measurement conducted without a radioactive source nearby: Figures 10.13, 10.14 and 10.15 show that for neither of the three bias voltages a current increase was observed.

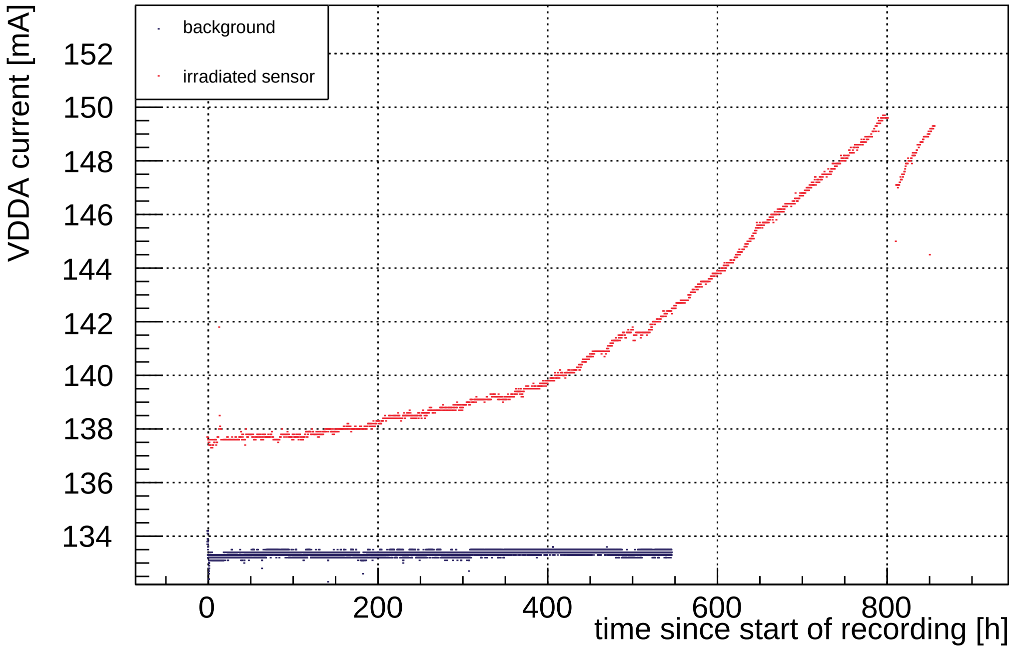

Figure 10.13: The VDDA current during irradiation and during the background measurement.

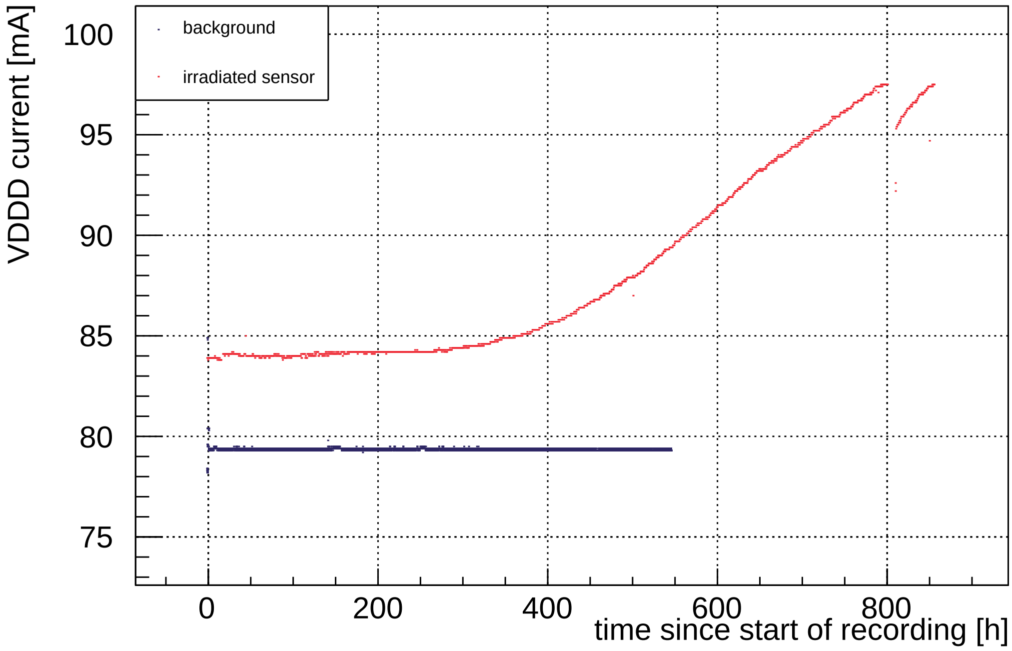

Figure 10.14: The VDDD current during irradiation and during the background measurement.

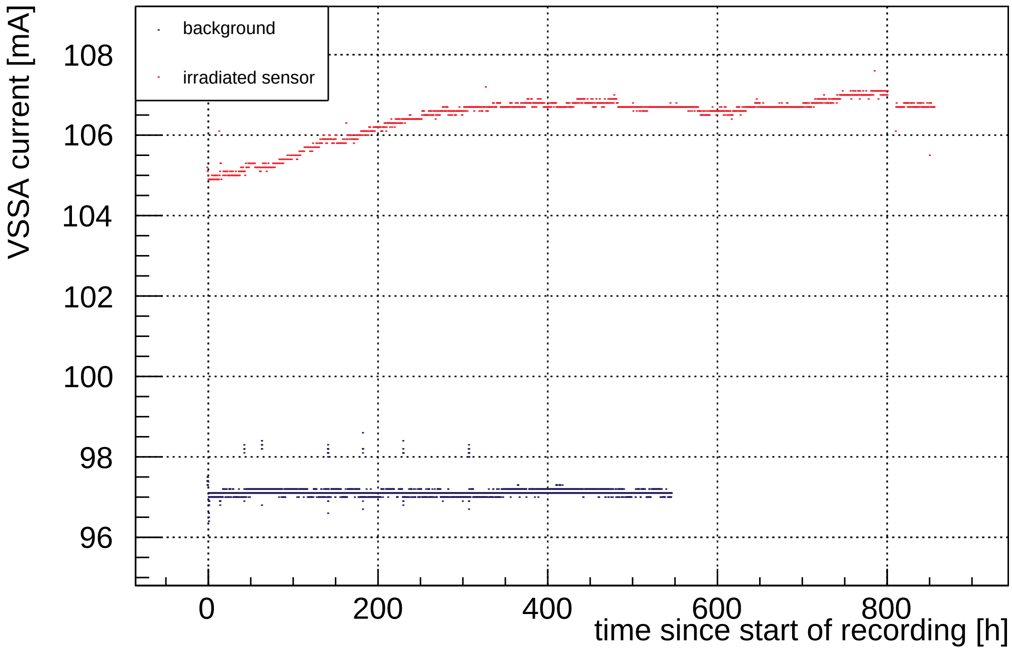

Figure 10.15: The VSSA current during irradiation and during the background measurement.

11 Characterization of the irradiated sensor

The MuPix8 sensor has a pixel matrix of 128 columns × 200 rows which is divided in three sub-matrices: The first 48 columns constitute matrix A, the following 48 columns make up matrix B and the remainder of 32 columns is called matrix C [14, p. 34].

As the MuPix8 is a prototype sensor, these matrices use different signal transmission techniques and matrices B and C turned out to be performing worse than matrix A [9, p. 50]. For this reason, matrices B and C were turned off during the tests described below and only the part known as matrix A is analyzed. The following results were taken from the testbeam data gained in July 2019. For each configuration (i.e. one threshold/temperature/high voltage combination), between 6.12×10^6 and 3.39×10^8 DUT-hits were registered to ensure enough statistics are available to gather meaningful results.

All threshold values given in the following sections are actually threshold-over-baseline-values to allow an easy comparison to different datasets. During the measurements the baseline was set to 500 mV.

11.1 Breakdown voltage

The MuPix-chips are HV-MAPS types which means that besides the usual low-voltage chip powering they also have a high voltage applied. The breakdown voltage describes the voltage from where on the sensor diode reaches its breakthrough region and as such poses an upper limit on the HV that can be supplied. In order to determine the breakdown voltage, an IV-curve (i.e. applying different voltages and plotting them against the current that flows) of the high voltage is recorded. When the diode goes into breakthrough, the current exponentially increases. This increase and the background current are each fitted with an exponential function. When these functions are plotted on a logarithmic y-axis, two straight lines can be observed. The breakdown voltage is then defined as the intersection of these lines.

Usually for MuPix8 sensors, this voltage is at $-50\,\mathrm{V}$ to $-60\,\mathrm{V}$ [14, p. 124]. However, after the Sr-90 irradiation the sensor showed significantly higher breakdown voltages. The breakdown voltages were measured for multiple temperatures during the testbeam in July 2019 once before and once after testing the sensor at each temperature setting. Due to one IV-curve measurement recording being corrupted, the breakdown voltage at 20 °C was only measured before testing the sensor. The individual I-V-curves with the according fits are shown in Figures A.4 to A.8. The resulting breakdown voltages are shown in Figure 11.1. A linear fit shows that the breakdown voltage rises with the temperature in a linear fashion by $(0.0583 \pm 0.0006)\,\mathrm{V/°C}$.

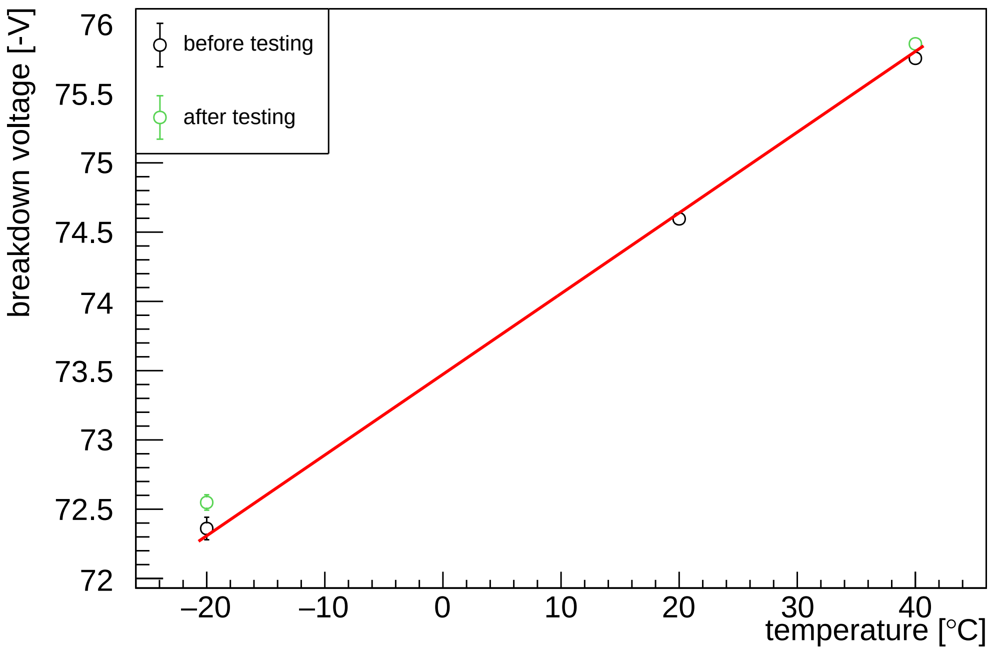

Figure 11.1: The breakdown voltages measured during the testbeam in July 2019.

As is shown in section 11.4 (and onwards), the sensor performs significantly better when a higher high voltage is applied. Considering this, further studies are necessary here, to determine whether this effect can be systematically observed and to what extent the breakdown voltage increases with the radiation dose.

11.2 Leakage current during the testbeam

The leakage current during the testbeam is plotted in Figure 11.2. Multiple effects can be observed here: The current rises significantly with the temperature, also a slight rise with an increase in the high voltage can be seen. This behavior is displayed in Figure 11.3 where the average leakage currents are plotted for each setting.

11.3 Power consumption during the testbeam

During the testbeam, the bias voltages were supplied at a 5 V input level applied to the motherboard which in turn has voltage regulators built-in that are then able to supply the appropriate voltages to the chip. This has two main consequences: Firstly, the measured current is not the current drawn by the chip itself but rather a sum of the current drawn by the chip and the current needed to supply the board. Secondly, the current measurements do no longer show a separation regarding what part of the chip consumes how much power. This makes the comparison to the power draw during irradiation more difficult where the three chip voltages were all individually supplied and measured.

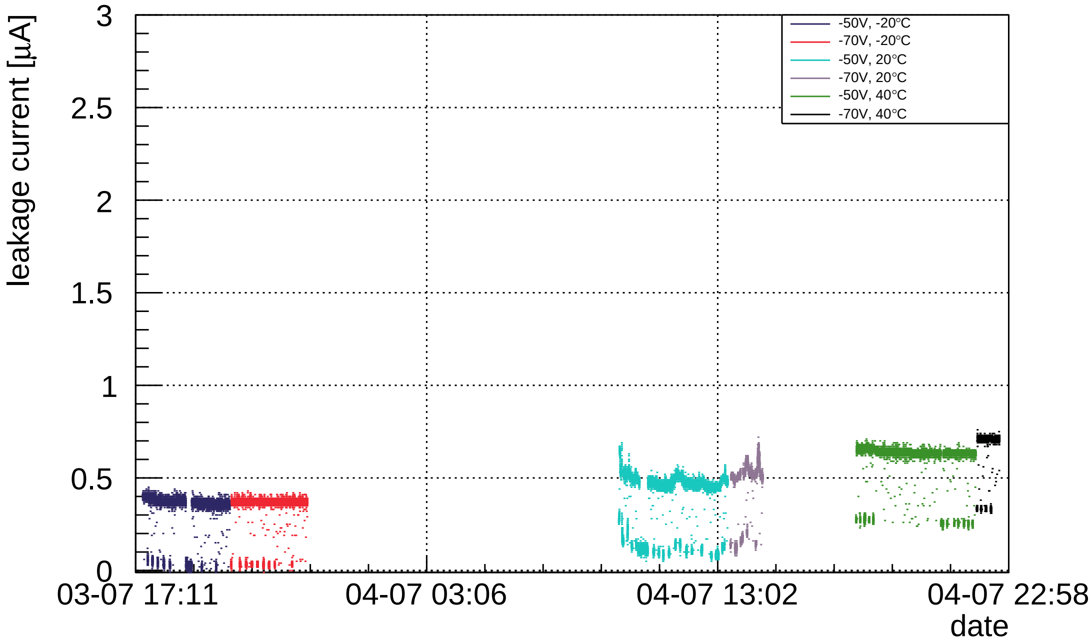

Figure 11.2: The HV current flow during the testbeam in July 2019.

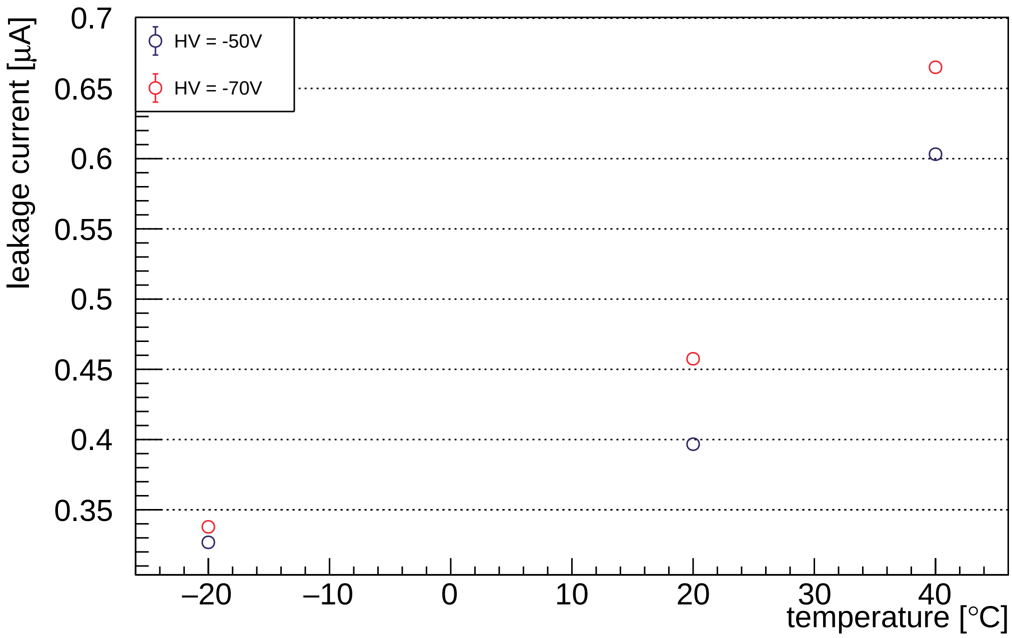

Figure 11.3: The averaged HV current flow during the testbeam in July 2019 at different temperatures.

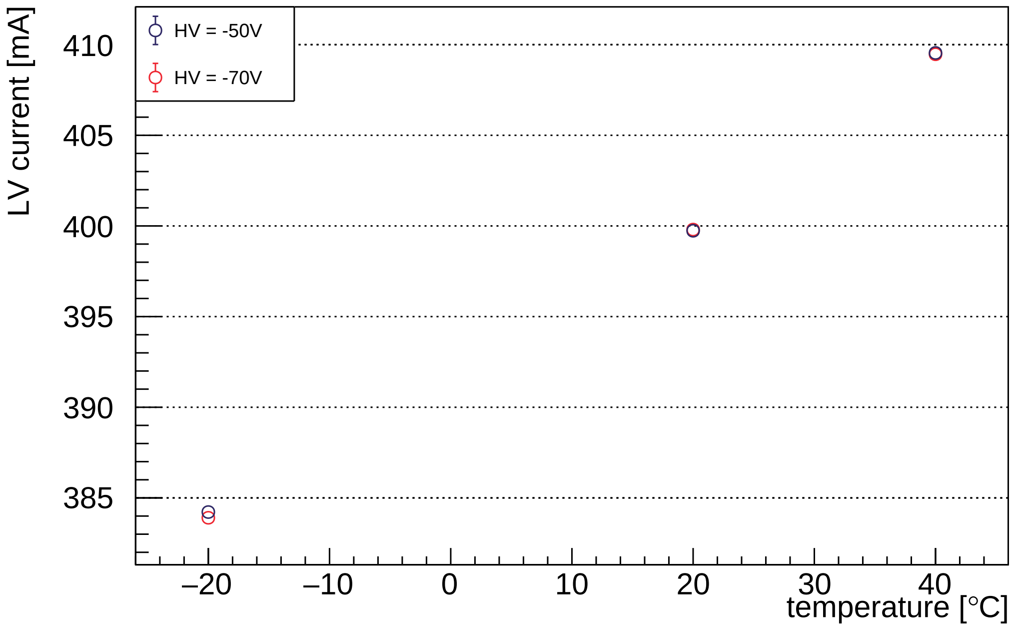

Figure 11.4: The LV current draw observed during testbeam plotted against all temperatures that experiments were conducted at.

In Figure 11.4 the LV current measured by the power supply (at 5 V) is plotted. The currents are all averaged values over all data points recorded at each temperature during the testbeam measurements. It is visible that the bias current does not significantly depend on the high voltage setting of the chip but is rather a function of the chip temperature only.

The board supply current is about 50 mA which is quite accurately the difference between the LV current at the testbeam at 20 °C and the combined LV current at the end of the irradiation which was performed at room temperature. It can be observed that decreasing the temperature from 40 °C to −20 °C lowers the power consumption by more than 6 %. This is a significant effect to take into account when planning the cooling setup.

Judging the overall power consumption is not an easy task for mainly two reasons:

- Due to the actual chip voltages being supplied by a board and not by the power supply with precise current and voltage measurements, the testbeam data cannot be considered to be as accurate as data gained in the laboratory with individually supplied bias voltages.

- Matrices B and C were not actively read out during the testbeam data taking. It is assumed, that this does not affect the power consumption of the chip, but a small impact cannot be ruled out.

As the data suggests that the power consumption at the testbeam is similar to the irradiation setup, this more reliable data set can be consulted to draw meaningful conclusions: It shows that the power consumption neared the mark of 350 mW/cm^2.

This increase however started from a power consumption of just below 320 mW/cm^2 which is already at the upper end of the range of acceptable chip power consumption. Consequently a significant increase of current flow due to chip irradiation has to be budgeted for when developing further MuPix chips.

11.4 Efficiency

The efficiency is defined as the fraction of all tracks that could be matched to a hit. For more details regarding this calculation see section 6.3.1. For the matching, a radius of 400 µm around the extrapolated track position was chosen which is a good compromise between matching a sufficient number of tracks and excluding noise from being counted as hits. Further, a matching time of 240 ns was chosen.

11.4.1 Corrections in the analysis

Due to some effects discussed below, the efficiency one would naively calculate using Equation 6.1 would be lower than the actual performance delivered by the chip. Because of that, some numerical corrections to minimize these effects are applied. Below, their impact and their justification is discussed.

Spatial edge effects To minimize the edge-effects that necessarily occur when doing measurements with a telescope with same-size sensors, the first and last 5 columns as well as the first and last 5 rows were cut off in the analysis for efficiency calculations. This means that the following results describe a sensor of 38 columns $\times$ 190 rows which corresponds to a sensor area of $\sim$46.8 mm^2.

Time edge effects Another artifact of the analysis that artificially lowers the calculated efficiency below the physically correct value is the offline sorting of hits: Generally all hit information from all chips in a telescope is sent to an FPGA where it is further processed and finally written to a file.

Per chip, all hits that are registered are packed in a so-called frame – a data read-out unit containing all hit data for a given time window. These frames are then sequentially read out by the FPGA. Put simplified, this can generally happen in two ways: Either the hits are written in the order they occur (i.e. the data is *sorted* and hits from frames of different sensors are mixed in-between each other) or the frames of all chips are sequentially written to disk (here, the hits of each chip are all in separate frames and the order in which they are written to disk does not necessarily encounter the order of the hits as they were encountered by the chip). In the latter case, the proper order of the hits needs to be restored during the analysis. This computation step is referred to as *offline sorting*.

Offline sorting is complicated due to multiple time stamps of different bit lengths being used when the run data is recorded. After all, the actual order cannot perfectly be restored which leads to a characteristic distribution of the restored track time stamps (i.e. a dip in the time stamp distribution at the edge of the frames). To counteract this behavior, tracks with corresponding time stamps are not considered in the analysis.

During the testbeam investigation of the electron-irradiated MuPix8 sensor data was not sorted on-FPGA and the offline sorting had to be employed.

Incorrect time stamp determination There is another effect which artificially lowers the measured efficiency which has to be corrected for in the analysis step: When determining whether to count a pulse as a hit, not one but two thresholds are used: `ThLow` and `ThHigh`. The threshold that determines whether a hit is to be counted is determined by whether it surpasses `ThHigh`. To minimize the effect of timewalk (see section 6.3.3) however, the `TS1`-value is sampled when the pulse surpasses `ThLow`. This behavior is schematically depicted in Figure 11.5.
When `ThLow` is now set too low (i.e. a value that is – at least in some pixels – surpassed by the normal noise level), the `TS1` sampling is stuck and it cannot sample any new values, thus its physically true value is never correctly recorded. Rather, the value of `TS1` is constantly written to memory. Therefore, the digital memory cells will discharge over time and all bits will reach the same value. In this case, `TS1` is 10 bits long, so the value $0b1\ 111\ 111\ 111 = 1023$ is read out. This behavior depends on the temperature and occurred in the recorded data for $\mathcal{O}(5)$ pixels at $-20\,°\mathrm{C}$, for $\mathcal{O}(20)$ pixels at $20\,°\mathrm{C}$ and for for $\mathcal{O}(40)$ pixels at $40\,°\mathrm{C}$. These hits will then mostly not be matched to tracks because the track time stamp differs by too much from the (false) hit time stamp.

As the (falsely) recorded `TS1` value is always the same one, this allows for a correction by not doing the time-matching step in the matching step of the analysis (see section 6.3). This in turn introduces an, albeit small, share of false-positive matches: Matching is still done based on spatial resolution, but the timing component is no longer available.

Given that this behavior occurred only on less than 50 px, an upper boundary on the overshoot efficiency / the reduced noise can be calculated: 50 pixels make up less than 0.7 % of the total pixel matrix. These pixels are safely assumed to have an efficiency of more than 90 %, so in a worst-case scenario it can with a lot of buffer be said that no more than 10 % of wrongly classified noise-hits are registered as being in a track on 0.7 % of all pixels. This means the efficiency is probably overcalculated by no more than 0.07 %.

On the other hand it is assumed that on these pixels the noise rate is higher than the one calculated due to the correction, so the noise is underestimated by no more than the same 0.07 % across the whole sensor (again, only accounting for the miscalculations done due to this specific correction). Due to the still-employed matching based on the hit-position, the actual over-/underestimation is even lower than the figure given above.

11.4.2 Temperature dependence

In Figure 11.6 it is clearly visible that the efficiency has suffered due to the irradiation. At thresholds of 100 mV and below it still meets the experimental requirements of being at 99 % or above. A rather interesting effect however is observed when look-

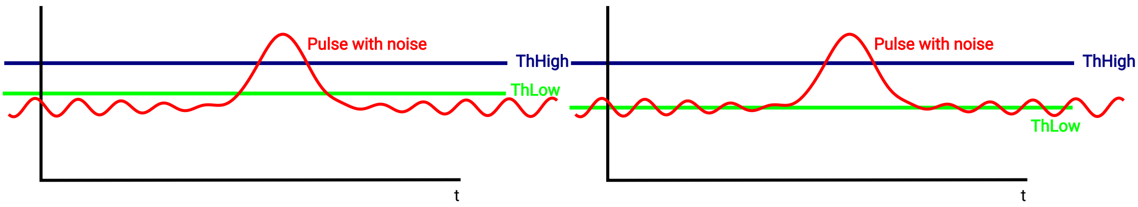

(a) Normal behavior. (b) Unwanted behavior producing sticky bit.

Figure 11.5: Schematic representation of the effect of `ThLow` being set too low (i.e. in the noise).

ing at the temperature dependence: Preliminary results indicate that at −20 °C normal, unirradiated sensors perform significantly worse than at higher temperatures of about 0 °C to 40 °C.[1]

For the irradiated sensor, a temperature gradient can generally be seen in the efficiency: With higher temperatures the efficiency degrades as evidenced by Figure 11.7. The difference between this behavior of the irradiated chip and an unirradiated reference could be explained by:

Internal chip temperature Due to higher leakage currents in the irradiated chip it heats up more than its non-irradiated counterparts which causes its actual temperature to be higher at the same environmental temperature. The reference data indicates however, that this effect would only explain the irradiated chip being more efficient than the unirradiated one at low temperatures and not the irradiated chip being most efficient at the lowest temperature.

Pulse height effects When a hit is registered in the chip, an according pulse is produced. When this pulse is shaped by chip components, its amplitude slightly decreases. As the irradiated chip has generally higher currents flowing, these pulse shaping effects and consequently the amplitude decrease are stronger. As the efficiency also scales with the produced pulse height, it is higher when less pulse shaping is taking place. This is exactly the case at lower temperatures and hence contributes to the irradiated chip being more efficient at lower temperatures.

11.4.3 High voltage dependence

The irradiated chip was (see section 11.1) able to run high voltages of up to −70 V safely. Therefore the chip was tested at both −70 V and at −50 V which is the HV the non-irradiated MuPix8 chips are usually run at.
Figure 11.8 and Figure 11.6 show the efficiency's dependence on the HV for each temperature and threshold setting. At the settings yielding the highest efficiency (i.e. low thresholds and low temperatures), the impact of the HV is very small and in some datapoints even negligible. As the overall efficiency decreases however (i.e.

[1]These results were obtained using a different sensor, and are not statistically backed up by tests with other sensors. Therefore, these results cannot be confirmed with complete certainty. For completeness, the relevant plots can be found in section A.1.

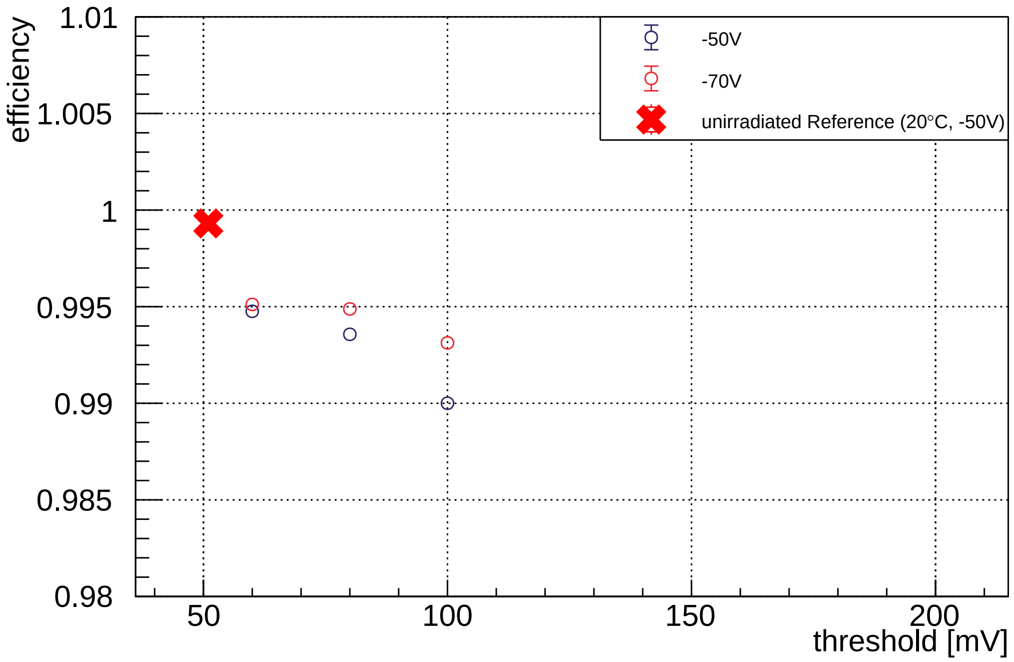

Figure 11.6: The threshold-dependent efficiency of the irradiated MuPix8 sensor at 20 °C compared to the unirradiated reference. Due to the zoomed-in y-axis, the efficiency at higher thresholds is no longer visible.

stepping away from the efficiency plateau and going towards higher temperatures) the -70 V setting leads to significantly better efficiencies.

With higher temperatures the plateau with acceptable efficiencies also drastically decreases in its width. At high voltage settings of -50 V this effect is even more predominant than at -70 V.

11.5 Noise

While the efficiency is defined as the fraction of tracks which have a hit matched to them, the noise on the other hand is defined as the remainder of hits: It is the number of hits on the DUT that have not been matched to a track. The reasoning behind this definition is that a hit without a corresponding track does not stem from an actual particle (which would have created a track). This definition brings with it an inherent overestimation of the actual noise because of inefficiencies in the reference layers: These inefficiencies lead to real particle hits being counted as noise.

The noise data in the following plots is always given as the average noise rate in Hz per pixel. Because of the effects described in section 11.4.1 the noise is corrected in the analysis just in a very analogous way to the efficiency, in particular the noise is averaged over an area of 38 columns $\times$ 190 rows.

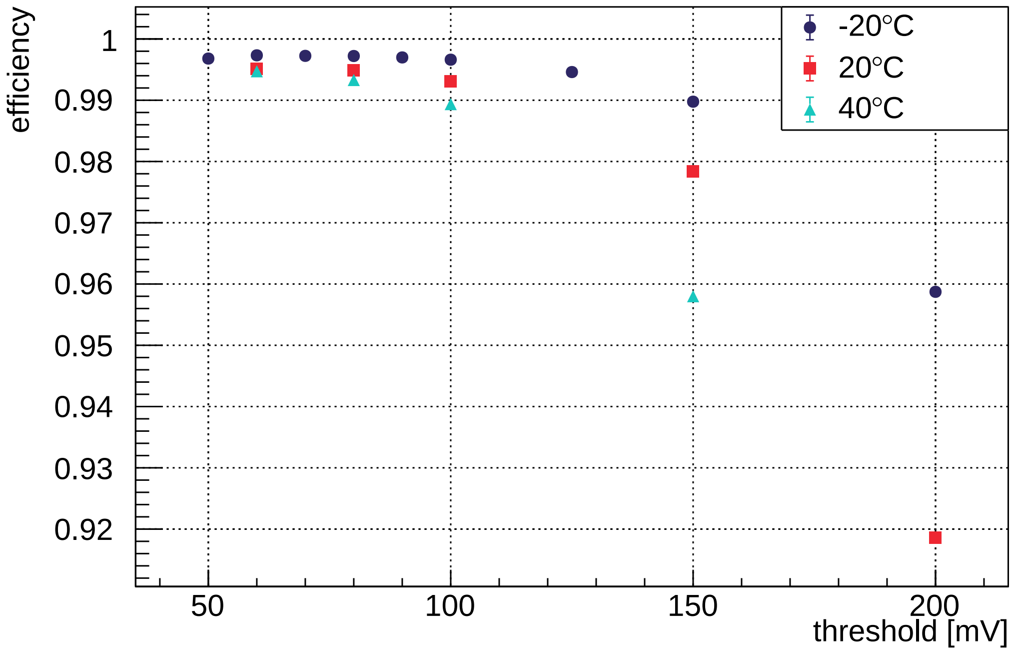

Figure 11.7: The threshold-dependent efficiency of the irradiated MuPix8 sensor at $-70\,\mathrm{V}$ at all temperatures that are measured. The efficiency decreases with an increasing temperature. A similar behavior is observed for a high voltage of $-50\,\mathrm{V}$ (see Figure A.12).

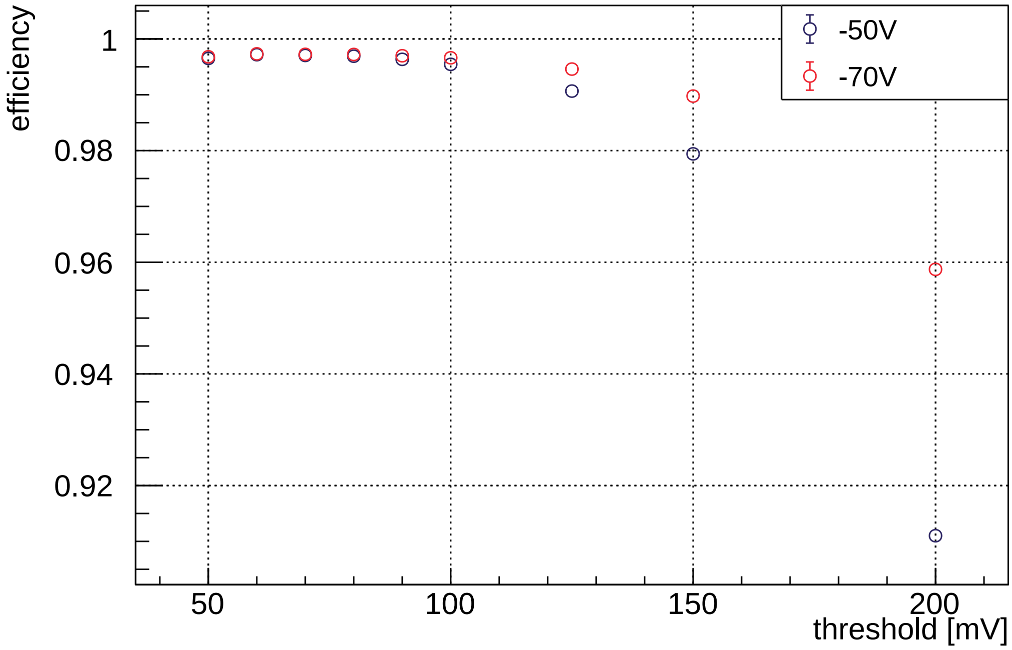

(a) Efficiency at $-20\,^{\circ}\mathrm{C}$.

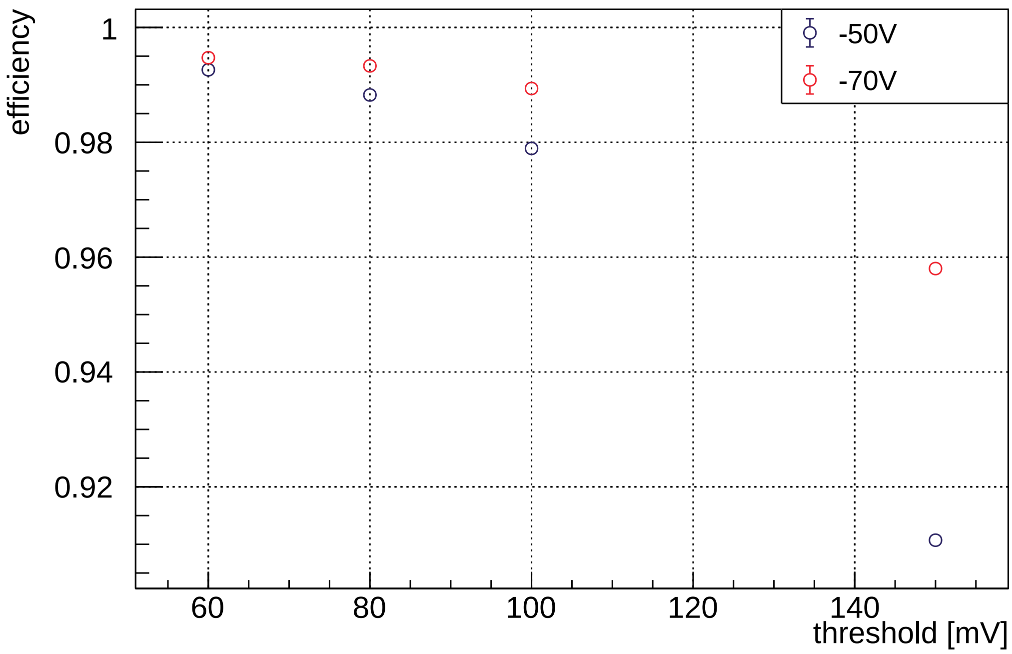

(b) Efficiency at $40\,^{\circ}\mathrm{C}$.

Figure 11.8: The irradiated sensor efficiency at chiller temperatures of $-20\,^{\circ}\mathrm{C}$ and $40\,^{\circ}\mathrm{C}$.

11.5.1 Temperature and HV dependence

Figure 11.9 shows that the noise rate barely depends on the HV setting: While at 40 °C the noise rate at 70 V is about 0.1 Hz higher than at −50 V (for the points with reasonable noise rates, i.e. at thresholds ≥80 mV), at 20 °C there is one data-point (threshold 100 mV) where the high voltage of −50 V has a higher noise. Finally at −20 °C the −50 V-setting produces almost consistently higher noise rates.

However, a strong dependence on the temperature can be seen: At thresholds below 80 mV the measurements taken at −20 °C consistently deliver the highest noise rates. Going towards higher thresholds of 100 mV and above this drastically changes and the measurements taken at −20 °C show the lowest noise rates and the ones taken at 40 °C show the highest noise rates.

11.5.2 Impact of the irradiation

In Figure 11.10 the noise rate at 20 °C is plotted against the threshold. It is apparent that the noise rate of the unirradiated sensor is several orders of magnitude smaller. This shows that the irradiation significantly increases the noise rate and matches with the observation that all (leakage) currents have increased over the irradiation period (see section 10.3) as leakage currents typically coincide with signal noise. Still the noise rates are well within the specifications for the final experiment.

11.6 Efficiency and noise

The requirements for the final Mu3e experiment are to have a sensor that provides an efficiency above 99 % while maintaining a noise rate of below 20 Hz/px. This leads to the challenge of having to find a working point (i.e. a threshold setting – and further settings that are beyond the scope of this thesis/whose characteristics have not been tested with the irradiated sensor) which simultaneously fulfills both conditions.

The data for the irradiated sensor suggests that the threshold value can be chosen relatively independent of the temperature and HV at around 60 mV to 80 mV when optimizing for optimal efficiency and noise.

Figure 11.11 shows that at −20 °C a threshold voltage of at least 80 mV is needed to fulfill the requirements. At higher temperatures the requirements are fulfilled by a threshold setting of 60 mV. Even at the worst performing combination of 40 °C and a high voltage of −50 V, an efficiency of 99.26 % can be confirmed at a noise rate of just below 4 Hz/px which is well within the demanded specification.

11.7 Clustering and crosstalk

Sometimes a single particle leads to a pulse being generated in multiple adjacent pixels. This happens especially when a particle does not enter the detector exactly perpendicular to the sensor plane. On the other hand, large pulses can lead to pulses being induced on the lines of other pixels due to capacitive coupling between

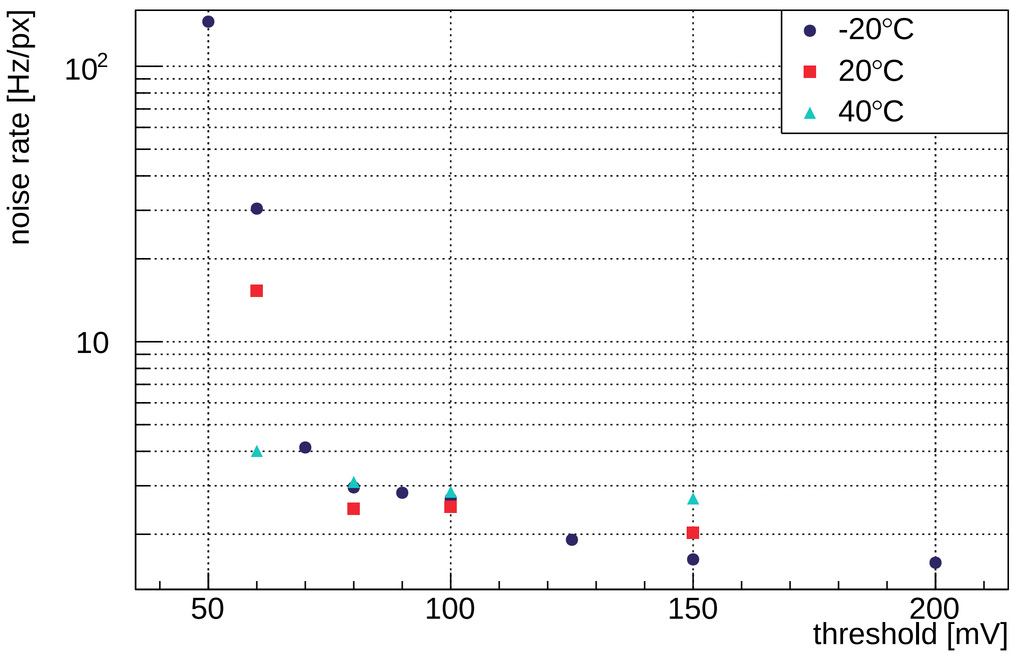

(a) Noise rate at $-50\,\text{V}$.

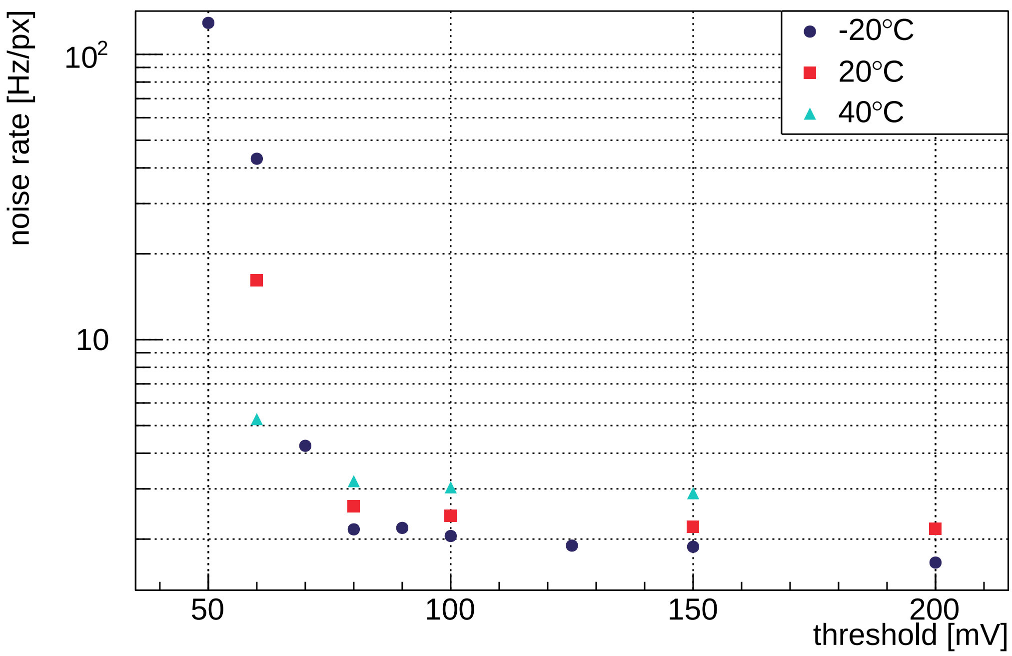

(b) Noise rate at $-70\,\text{V}$.

Figure 11.9: The per-pixel noise rates at HV settings of $-50\,\text{V}$ and $-70\,\text{V}$.

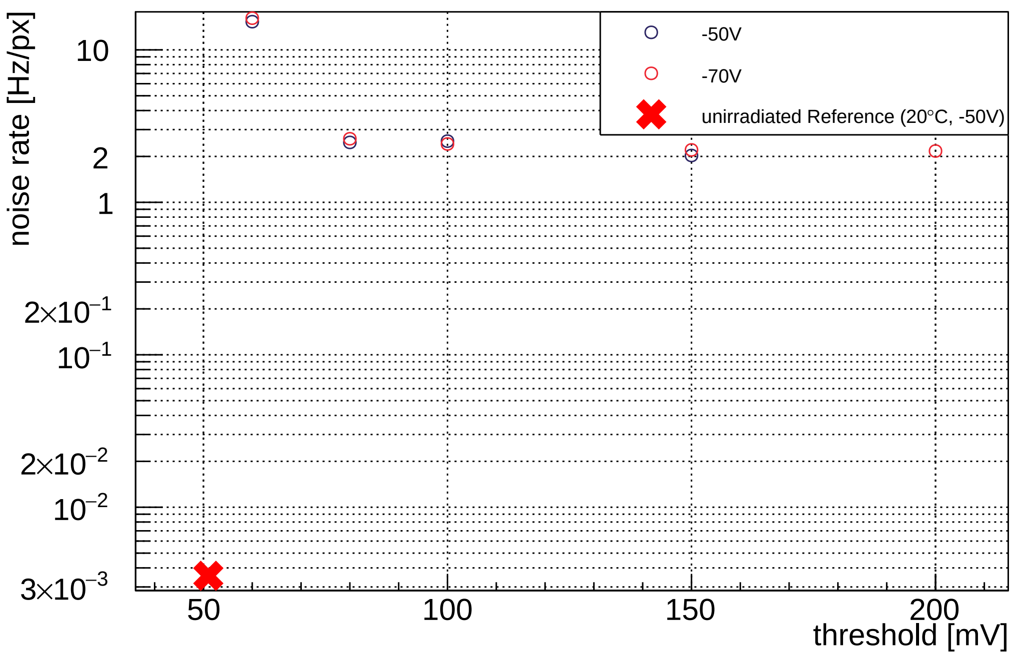

Figure 11.10: The noise rate at 20 °C with the unirradiated reference data-point.

them [26, p. 59]. Therefore this so-called crosstalk depends on the physical on-chip routing layout and it can – at least statistically – be filtered out in the analysis.

11.7.1 Raw cluster sizes

In Figure 11.12 the raw (i.e. without any corrections in the analysis) cluster size as well as the crosstalk-corrected cluster size is displayed. From this plot, three things are mainly inferred:

HV dependence At low thresholds (i.e. below 150 mV) the high voltage of −70 V leads to significantly bigger clusters than the one of −50 V. The difference in cluster size decreases with an increasing threshold and nearly vanishes at a threshold of 150 mV.

Temperature dependence The lower the temperature, the bigger the clusters that the sensor registers. The strength of this effect also decreases with an increasing threshold, just as the HV dependence. However the temperature seems to affect the cluster size stronger and at a threshold of 150 mV, significant differences between the different temperature datapoints can be seen at both −50 V and −70 V.

Changes due to irradiation A comparison with the unirradiated sensor shows that – at least at the one data-point that is available – the irradiated sensor has significantly smaller clusters: At comparable settings (threshold 51 mV for the non-irradiated, 60 mV for the irradiated sensor, HV at −50 V, temperature 20 °C), the

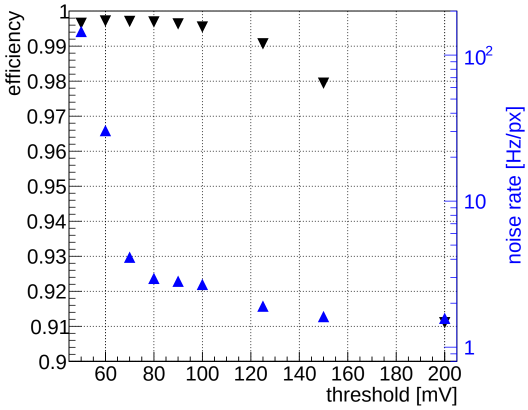

(a) At −20 °C and −50 V.

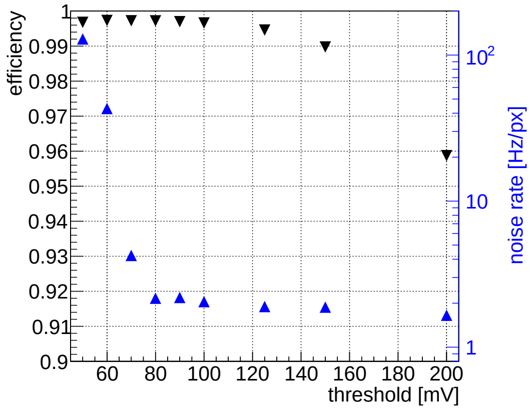

(b) At −20 °C and −70 V.

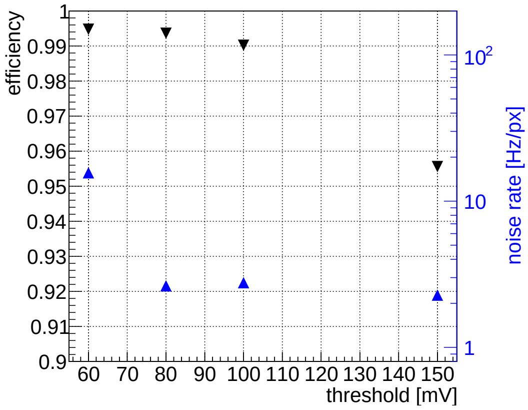

(c) At 20 °C and −50 V.

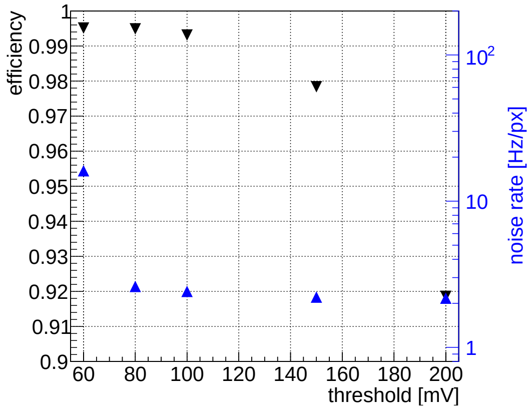

(d) At 20 °C and −70 V.

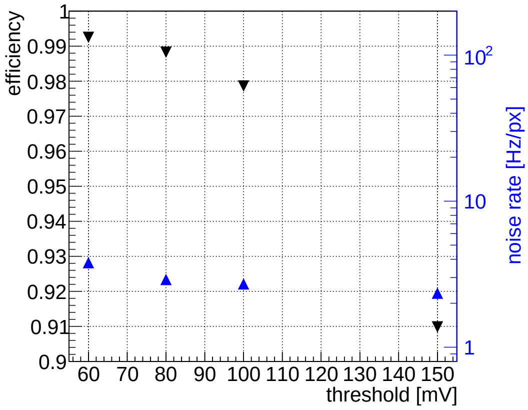

(e) At 40 °C and −50 V.

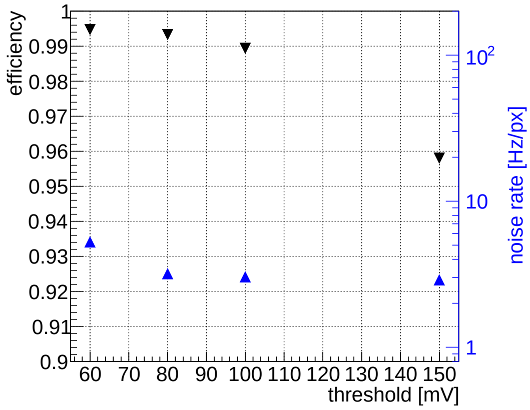

(f) At 40 °C and −70 V.

Figure 11.11: The efficiency and the noise of all settings. A threshold setting of 60 mV to 80 mV leads to desired results within the specified requirements.

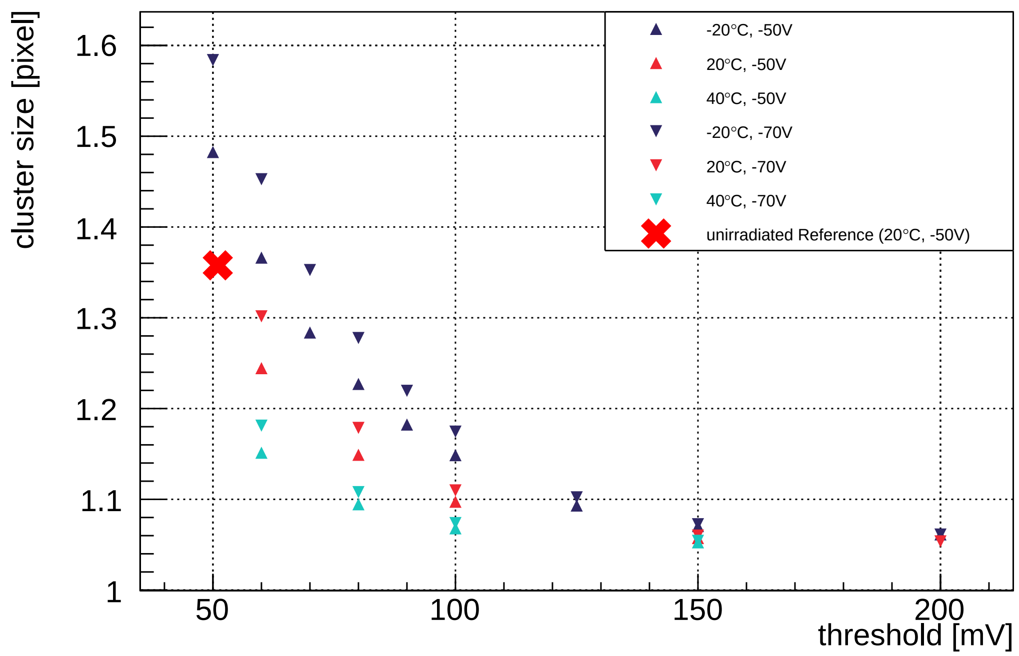

Figure 11.12: The raw cluster size with an unirradiated reference datapoint from the same sensor.

irradiated sensor has a cluster size of 1.24 px whereas the non-irradiated sensor shows a cluster size of 1.36 px.

11.7.2 Crosstalk analysis

The MuPix8 layout favors crosstalk to occur in rows with higher numbers [14, pp. 36 sq.]. This can be seen in Figure 11.13 which shows the crosstalk probability – a measure describing how probable it is that a randomly chosen hit registered in a given column originates from crosstalk and is not in fact triggered by an incoming particle. This value is in fact not an exact number but rather a statistically derived quantity (see section 6.3.2 for more details) which at the number of hits registered for the analysis conducted here can be assumed to be rather sound.

In Figure 11.14 one can see the corresponding crosstalk measurement for the irradiated sensor under the same conditions: The crosstalk of the non-irradiated sensor is greater by a factor of about 1.5. Also the crosstalk starts about 15 row addresses later in the irradiated sensor. This hints at a generally lower pulse height in the irradiated sensor which means that longer parallel data lines (equal to a larger capacity between the lines) are necessary for crosstalk to occur.

While all threshold/high voltage/temperature-combinations lead to essentially the same qualitative row-address dependent behavior, the amount of crosstalk encountered varies greatly with high voltage, temperature and of course the threshold. This is illustrated by Figures 11.15 and 11.16: A higher HV setting leads to a larger crosstalk probability, especially at the higher column addresses. At the same time,

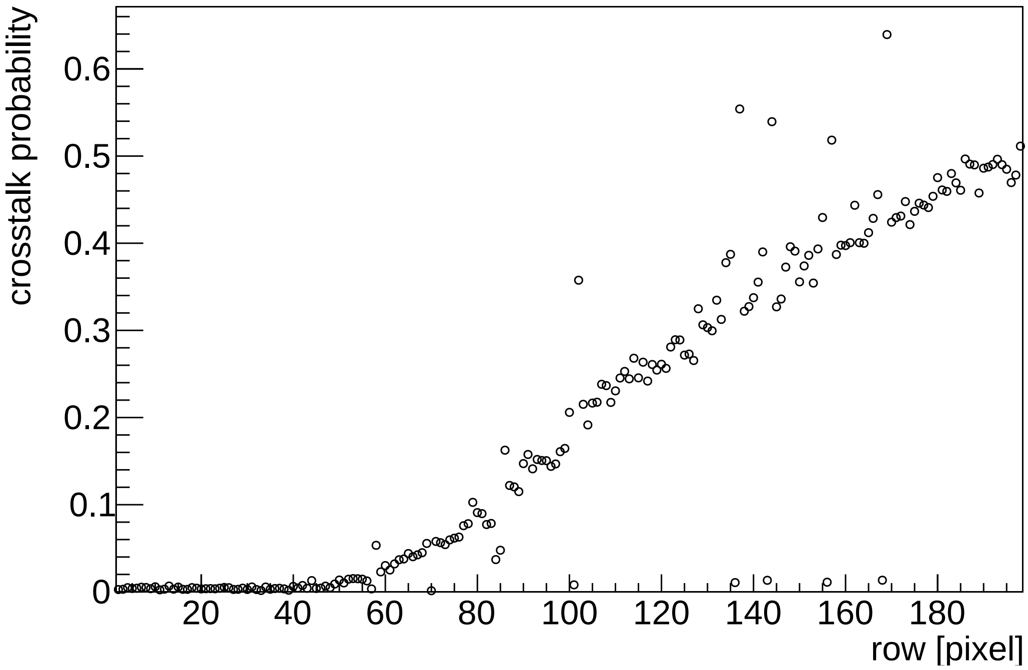

Figure 11.13: The row-address dependent crosstalk of the unirradiated sensor.

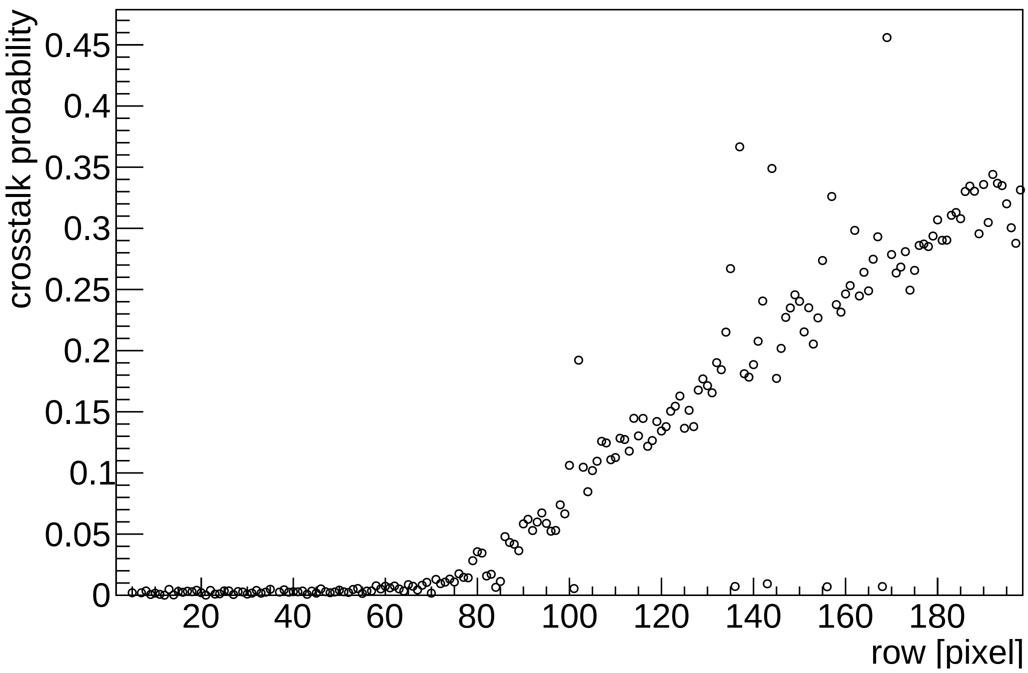

Figure 11.14: The row-dependent crosstalk of the irradiated sensor at the same settings as the unirradiated sensor (depicted in Figure 11.13).

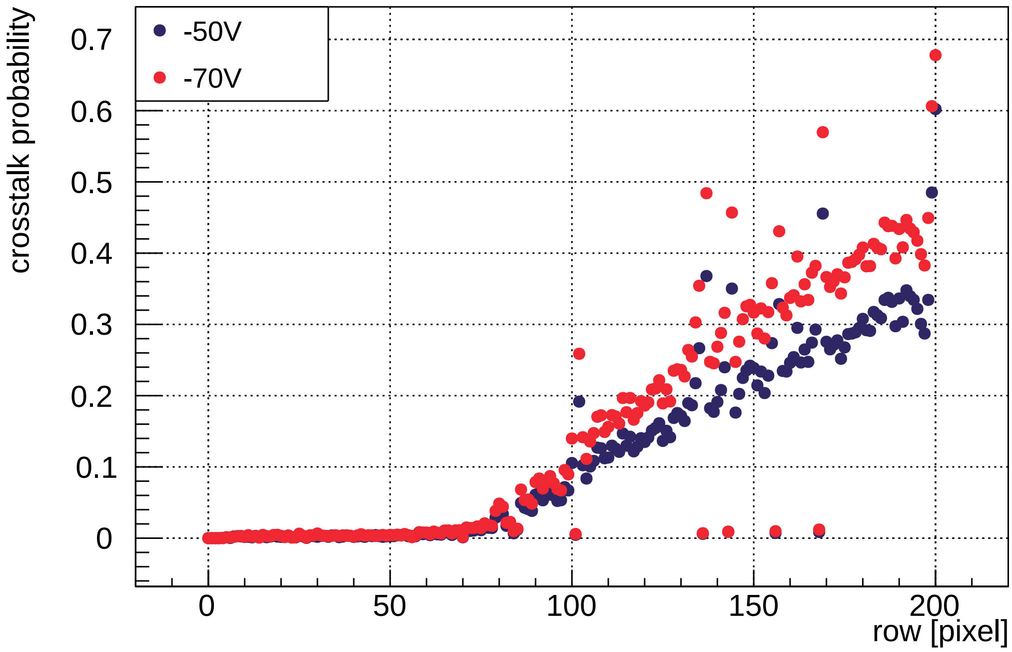

Figure 11.15: The row-address dependent crosstalk of the irradiated sensor at a threshold of 60 mV and a chiller temperature of 20 °C. A similar behavior is observed at −20 °C and 40 °C (see Figure A.10 and Figure A.11).

a lower temperature leads to more crosstalk. The probably most significant impact on the crosstalk is however given by the threshold: At the highest thresholds of above 150 mV, crosstalk is nearly completely suppressed as the signals induced by capacitive coupling are too low to cross these thresholds. This is illustrated in Figure 11.17.

11.7.3 Crosstalk corrected cluster analysis

From the data gathered above, the cluster size originating from actual charge sharing from a single particle can be calculated: The crosstalk hits are subtracted (see section 6.3.2 for details on the calculation) from the other registered hits to obtain the corrected cluster size. This is of course mainly depending on the chip orientation in regard to the beam: If a layer is not placed perpendicular to the beam, particles may traverse two (or at shallower angles even more) pixels and trigger a signal in them.

As all measurements were taken with the same setup and planes set up roughly perpendicular to the beam, the results contain information on how likely it is that particles pass through pixel edges.

From Figure 11.18, multiple effects can be observed: One is that the corrected cluster size still decreases with the threshold. Further, it is apparent that at 40 °C and 20 °C, the −50 V setting leads to smaller clusters, whereas at −20 °C for thresholds 100 mV and below, the clusters occurring at −50 V are larger.

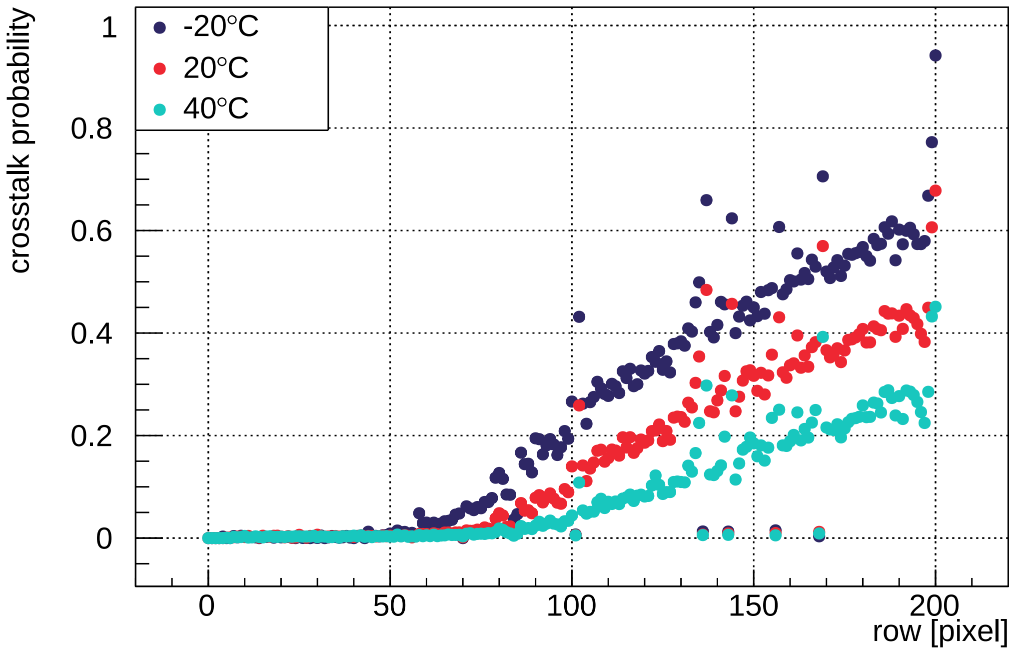

Figure 11.16: The row-address dependent crosstalk of the irradiated sensor at a threshold of 60 mV and a high voltage of −70 V. A similar behavior can be observed at −50 V (see Figure A.9).

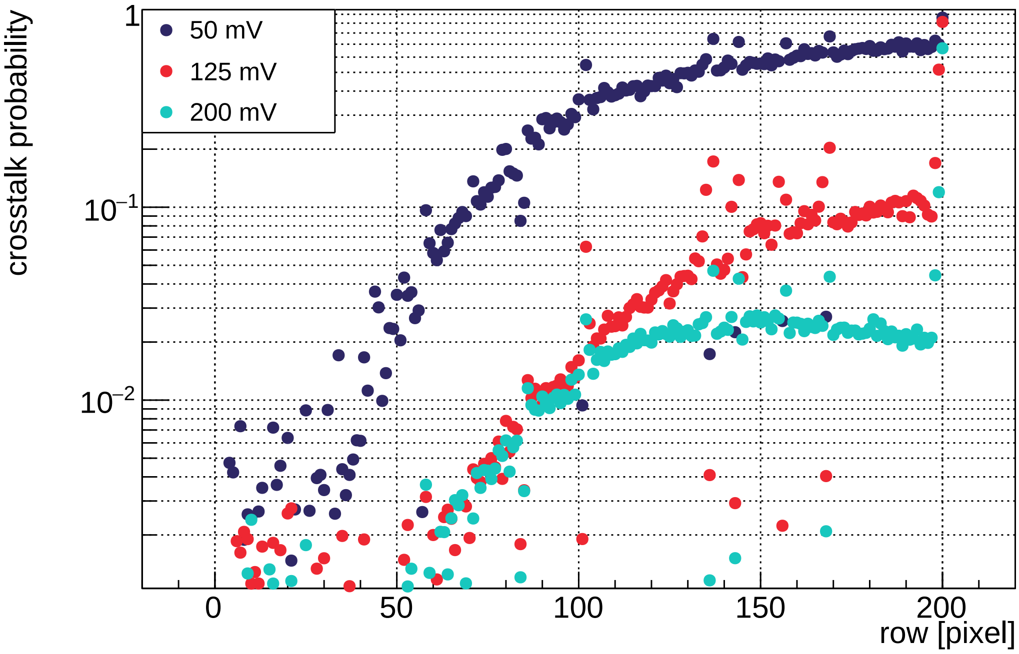

Figure 11.17: The row-address dependent crosstalk of the irradiated sensor at a high voltage of −70 V at −20 °C.

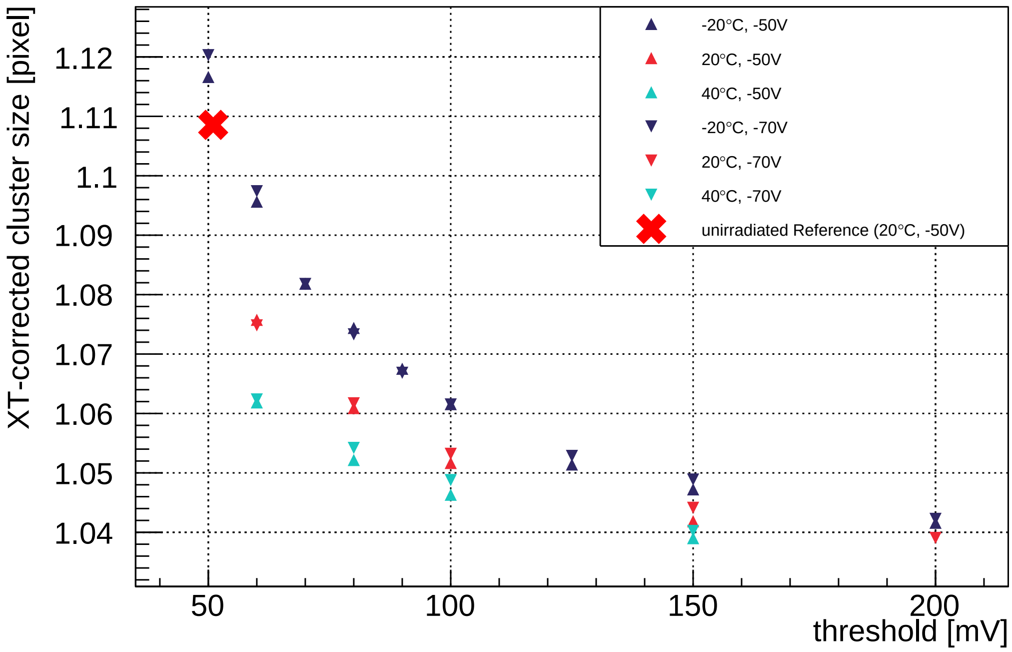

Figure 11.18: The crosstalk-corrected cluster size has greatly increased after the irradiation.

The larger impact on cluster size is had by the temperature: The cluster size rises with a lower temperature for both HV settings at all measured threshold values.

11.8 Time resolution

Another important characteristic of a particle detector is its time resolution. The final MuPix detector is aiming for a time resolution of below 20 ns [2]. It is crucial that this time resolution can be achieved as well in the later stages of the experiment runtime after the detector has been subjected to particle irradiation.

The data presented below shows the time resolution measured at the testbeam at DESY in July 2019. Due to the configuration used there, the ToT information was not correctly sampled. This means that the most significant offline correction step – the timewalk-correction (see section 6.3.3 for more details) – cannot be performed in the analysis.

As the Mu3e requirements specify a target for the uncorrected time resolution this is of no further concern. However it would still be interesting what time resolutions could potentially be reached with a timewalk-correction to decide on whether it could be incorporated in some form. Besides the timewalk-correction, two more corrections are applied: The *run correction* and the *delay correction*; the details of these corrections are explained in section 6.3.3.

Chiller temperature [°C]	HV [V]	chosen threshold [mV]	time resolution [ns]
-20	-50	70	16.79 ± 0.01
	-70	70	14.94 ± 0.01
20	-50	60	24.73 ± 0.03
	-70	80	24.22 ± 0.02
40	-50	60	45.05 ± 0.05
	-70	60	39.77 ± 0.03

Table 11.1: The uncorrected time resolution of the irradiated MuPix8 at various settings.

11.8.1 Uncorrected time resolution

The raw time resolution (as defined in section 6.3.3) is displayed in Figure 11.19. It is obvious, that the time resolution has been impaired due to the irradiation: Earlier studies measured uncorrected time resolutions of 20 ns [14, p. 127] or between 10.5 ns to 13.5 ns [9, pp. 95 sqq.], while the raw time resolution of the irradiated sensor before irradiation was determined to be (14.904 ± 0.006) ns (see section 9.2).

The irradiated sensor shows a time resolution that is worse and degrades with the threshold, eventually saturating at thresholds above 150 mV. For datapoints with a satisfactory efficiency/noise-ratio (i.e. thresholds of 60 mV to 80 mV), uncorrected time resolutions as listed in Table 11.1 were measured.

At -20 °C these fulfill the final experiment specification of being below 20 ns whereas all higher temperature settings miss this goal. A clear beneficial effect of an increased high voltage can be seen in the data: At the same threshold, increasing the HV from -50 V to -70 V improves the time resolution by nearly 2 ns at -20 °C, by roughly 3 ns at 20 °C and by around 5 ns at 40 °C chiller temperature.

The more significant impact is however had by the temperature: At -50 V of high voltage applied, the jump from -20 °C to 20 °C worsens the time resolution by roughly 10 ns (with slight variations depending on the threshold), the step to 40 °C further increases the time resolution by approximately 20 ns. At -70 V these values are around 7 ns and again 20 ns respectively.

11.8.2 Run- and delay-corrected time resolution

The run-correction does not yield real improvements in the time resolution, they are mostly within 1 ns of the uncorrected time resolution. This is to be expected due to the nature of the run correction.

The delay correction described in section 6.3.3 is always applied after the run correction described above. Therefore, the results presented below as delay-corrected always include an already-made run-correction. It significantly benefits the time resolution as can be seen in Figure 11.20: The time resolution improvements are in the same order of magnitude for all other temperature/high voltage combinations. Depending on how good the initial raw time resolution is, an improvement ranging from less than 1 ns to up to 30 ns for the worst initial time resolution can be observed.

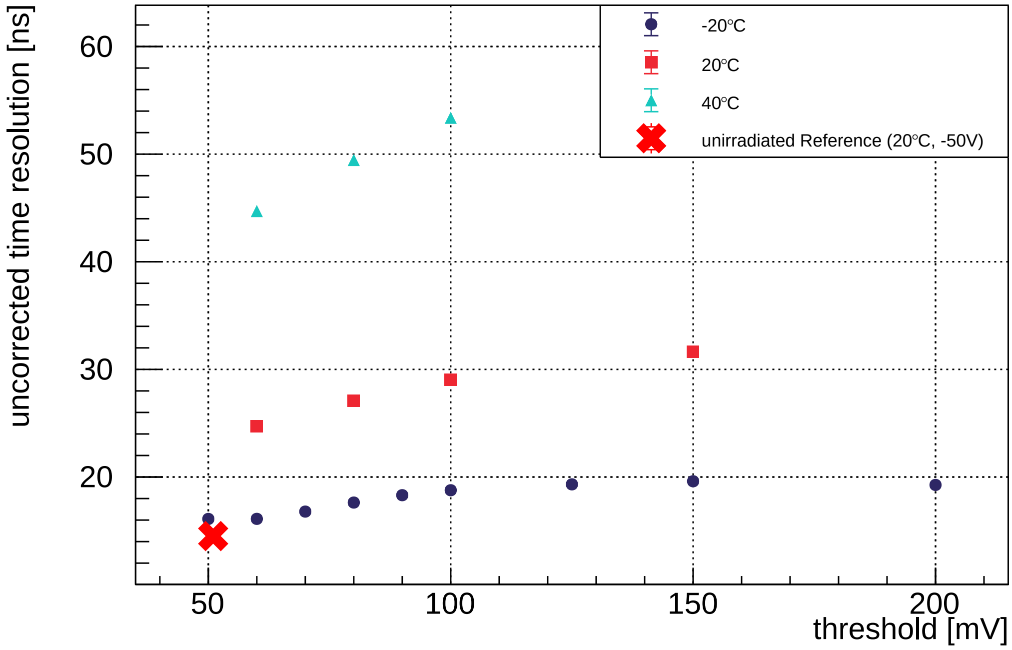

(a) At −50 V.

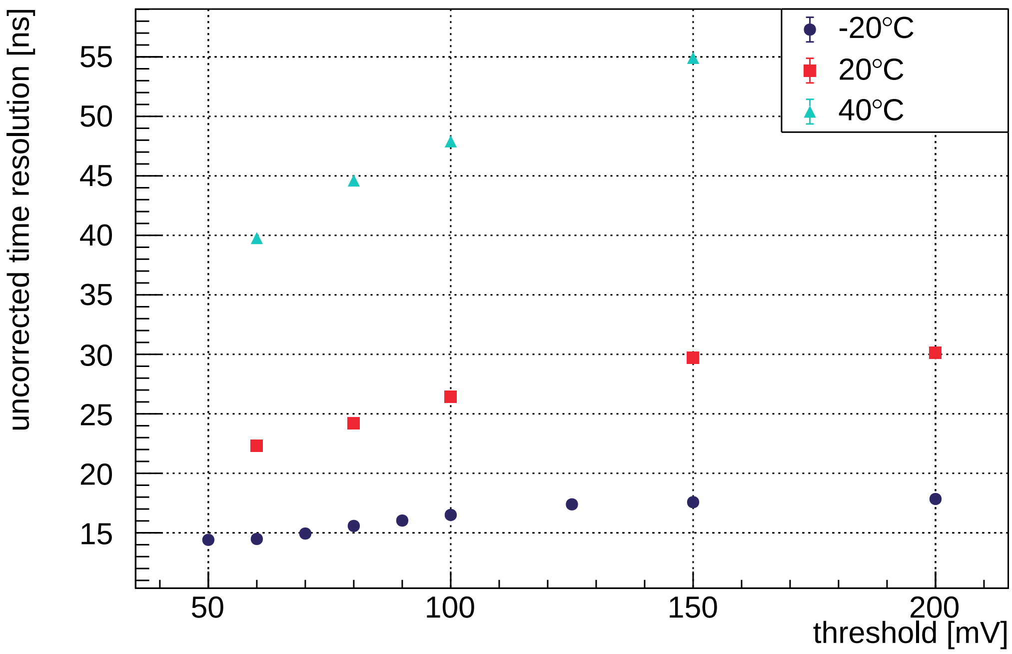

(b) At−70 V.

Figure 11.19: The uncorrected time resolution of the irradiated MuPix8 sensor.

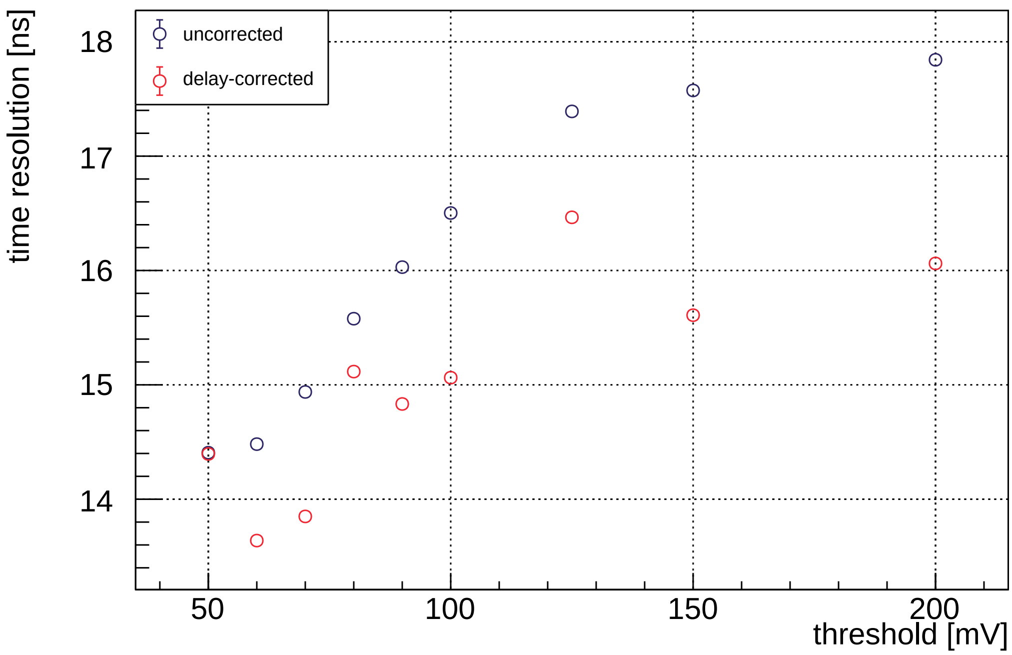

(a) At $-70\,\mathrm{V}$ and $-20\,^{\circ}\mathrm{C}$.

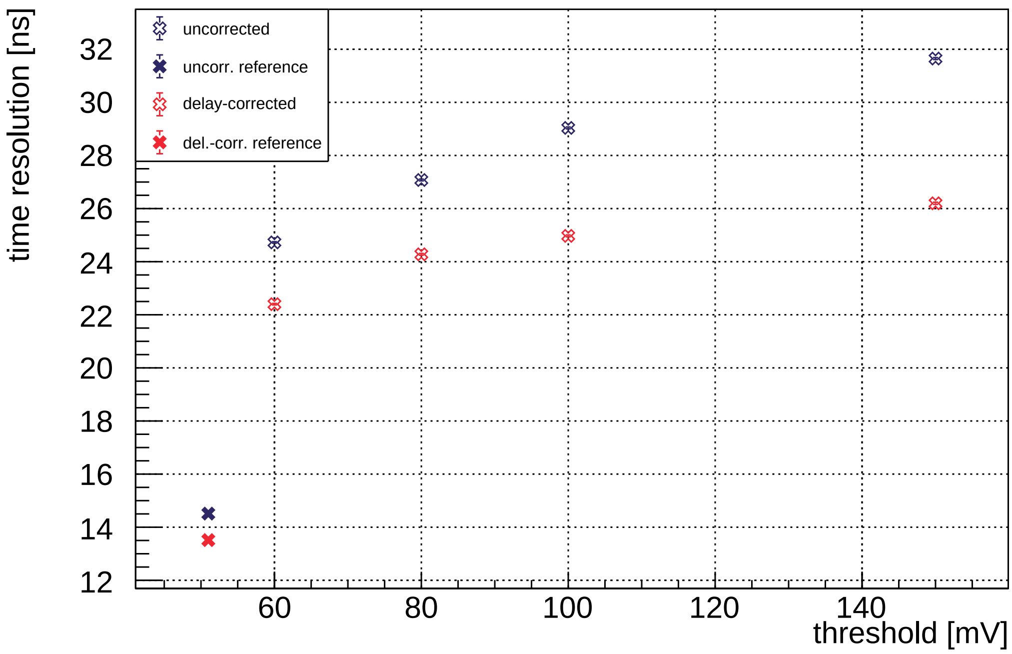

(b) At $-70\,\mathrm{V}$ and $-20\,^{\circ}\mathrm{C}$ with unirradiated reference.

Figure 11.20: The uncorrected time resolution compared to the delay-corrected time resolution.

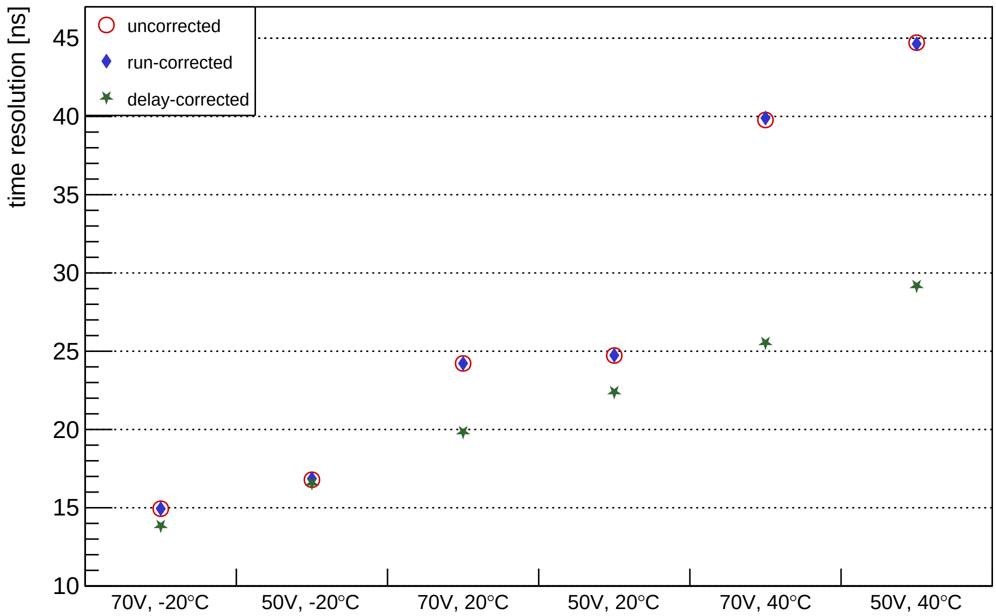

Figure 11.21: Overview of the time resolutions at different conditions with all available corrections. The thresholds were chosen as in Table 11.1 (i.e. at thresholds with reasonable efficiency/noise levels which also achieve satisfactory (in comparison to other thresholds) time resolution).

11.8.3 Evaluation of time resolution

The time resolution of all settings at reasonable thresholds (regarding the efficiency/noise of the sensor at these thresholds) are displayed in Figure 11.21. It is again visible, that the run-correction brings no real improvement in time resolution. The delay-correction however yields a significant improvement of up to 15 ns. It is clear that the time resolution has suffered due to the irradiation and it cannot be said with complete certainty, that this sensor will always fulfill the requirements for the final Mu3e experiment: In fact, early simulations of the cooling solution show that the inner detector as well as the outer detector have parts with helium (which is used for cooling) temperatures of up to 43 °C [33, pp. 44 sqq.].

However, the timewalk-correction step usually yields an additional improvement about as large as the one of the delay correction (see e.g. [9, p. 90], [14, p. 134]). This could not be verified for the irradiated sensor as the time over threshold could not be reconstructed, it is however likely that this correction step would bring the results at somewhat higher temperatures into an acceptable range. It further has to be noted, that the sensor was not tuned for optimal time resolution, so with different settings, a better time resolution is likely to be measured, however the impact is again hard to predict.

Part IV

Discussion

12 Conclusion

The Mu3e experiment aims to observe the decay of $> 2.5 \cdot 10^{15}$ muons only in phase I of the experiment [2, p. 2]. This shows the need for a detector that can – amongst satisfying the primary requirements tied to the main goals of the experiment – withstand a significant amount of low-energy irradiation stemming mostly from electrons.

Accordingly, an irradiation campaign with a Sr-90 source was carried out where an in situ powered and read out sensor was irradiated with approximately $5.4 \cdot 10^{12}$ electrons, equal to a dose of about 2 kGy. Due to the permanent monitoring during the irradiation, in this thesis it was found that the power consumption of the sensor increased by slightly more than 50 mW.

In this thesis it was shown that with the MuPix8 prototype, a solid foundation is laid for the final Mu3e sensor chip. While the efficiency and noise rate targets laid out for the Mu3e detector can be met, the desired time resolution could not be achieved. It was shown that the time resolution was severely impacted by the irradiation albeit under certain surrounding temperatures and with an increased high-voltage, a satisfactory time resolution could be reached.

Further, an increase in the breakdown voltage was observed which opens up new possibilities to easily improve the sensor characteristics of the chip after they have suffered from the effects of the irradiation.

The best-working settings for each temperature and high-voltage combination, that was tested with the irradiated sensor is displayed in Table 12.1. While the noise rate has significantly surpassed that of unirradiated sensors, it can be seen, that the sensor fulfills the Mu3e noise and efficiency requirements at all settings. The time resolution can however only be reached at a chiller temperature of $-20\,°\mathrm{C}$.

It was shown that during the irradiation the number of registered hits decreased by far more than the efficiency decreased over the same time frame. This is a clear indication that the irradiation caused a shift in the (optimal) working point of the sensor. Hence it is necessary, to find an optimized configuration for irradiated sensors, or rather a set of configurations for different amounts of radiation exposure. These settings are also expected to recover the sensor performance, especially the time resolution.

Temp. [°C]		HV	thresh.	eff.	noise	raw TR[c]	del.-corr. TR[c]
chiller	chip[d]	[V]	[mV]	[%]	[Hz/px]	[ns]	[ns]
-20	29.93 ± 1.37	-50	70	99.70	4.1	16.79 ± 0.01	16.58 ± 0.01
		-70	70	99.72	4.2	14.94 ± 0.01	13.85 ± 0.01
20	60.76 ± 1.27	-50	60	99.48	15.3	24.73 ± 0.03	22.40 ± 0.03
		-70	80	99.49	2.6	24.22 ± 0.02	19.84 ± 0.01
40	79.69 ± 1.32	-50	60	99.26	4.0	45.05 ± 0.05	29.18 ± 0.05
		-70	60	99.47	5.3	39.77 ± 0.03	25.54 ± 0.02
unirr. ref. ($\sim$20 °C, -50 V, 51 mV)				99.93	0.004	14.90 ± 0.01	13.91 ± 0.01

Table 12.1: An overview of the characteristics of the irradiated sensor.

[c] Time resolution.

[d] The chip temperature was derived from the on-chip temperature diode.

13 Outlook

The probably biggest issue encountered after the irradiation is the degraded time resolution. Consequently, more research has to be done in this direction. One idea is to do some sort of online timewalk-correction as proposed in [9, p. 84]. As timewalk-correction was not tested for the irradiated sensor, the actual impact of this is not clear but other datasets clearly indicate that the timewalk-correction delivers an even greater improvement than the delay correction.

On the other hand, more recent chip generations show an improved time resolution when compared to the MuPix8. It is unclear how these are impacted by irradiation and whether additional work is even necessary to reach the Mu3e requirements. Therefore the irradiation study has to be repeated with the available close-to-final chip MuPix10, to identify whether changes on the sensor are necessary to reach the Mu3e design goals or if the performance can be fully recovered with optimized chip configurations.

Further, a systematic study of the observed effects, most notably the better performance at lower temperatures and the recovery in power consumption after the power outage, suggests itself. Fully understanding the conditions and strengths of these effects could allow to exploit them in order to further improve the sensor performance over the experiment run-time.

Part V

Appendix

A Additional plots

A.1 Temperature-dependent behaviour of an unirradiated sensor

During the testing of some chip features in May 2019, the sensor with the ID 265-3-5 was tested at several temperatures. This allows to see the efficiency of an unirradiated chip at different temperatures which is shown in Figure A.1. It is clearly visible, that while the chip performs best at 20 °C, the performance severely degrades when going from 0 °C to −20 °C.

At the same testbeam, data about the time resolution was gathered as well. The results of the uncorrected can be seen in Figure A.2. Figure A.3 shows the delay corrected time resolution. Interestingly, the chip performs best at 0 °C chiller temperature while the performance at 20 °C is degraded. The difference in time resolution at different temperatures is however by far smaller than the differences the irradiated sensor showed.

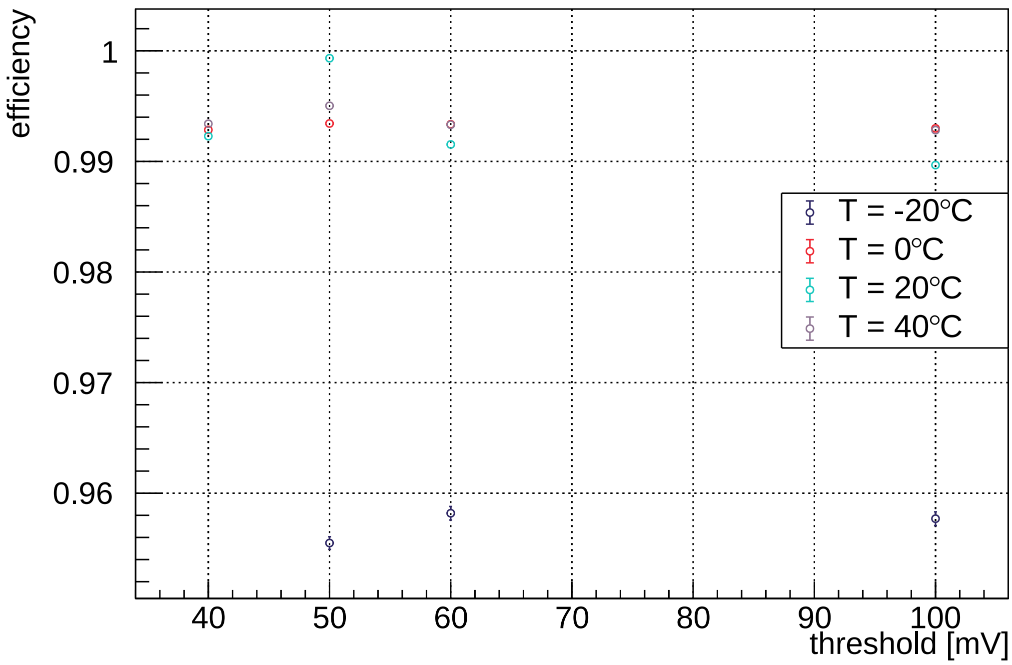

Figure A.1: The efficiency of a MuPix8 at different temperatures.

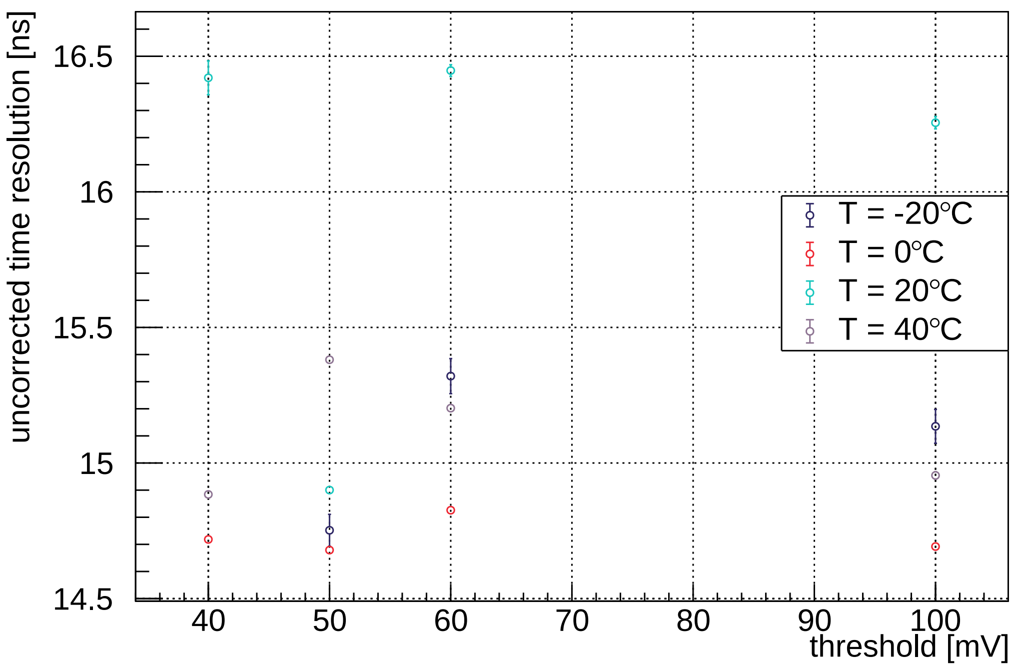

Figure A.2: The uncorrected time resolution of a MuPix8 at different temperatures.

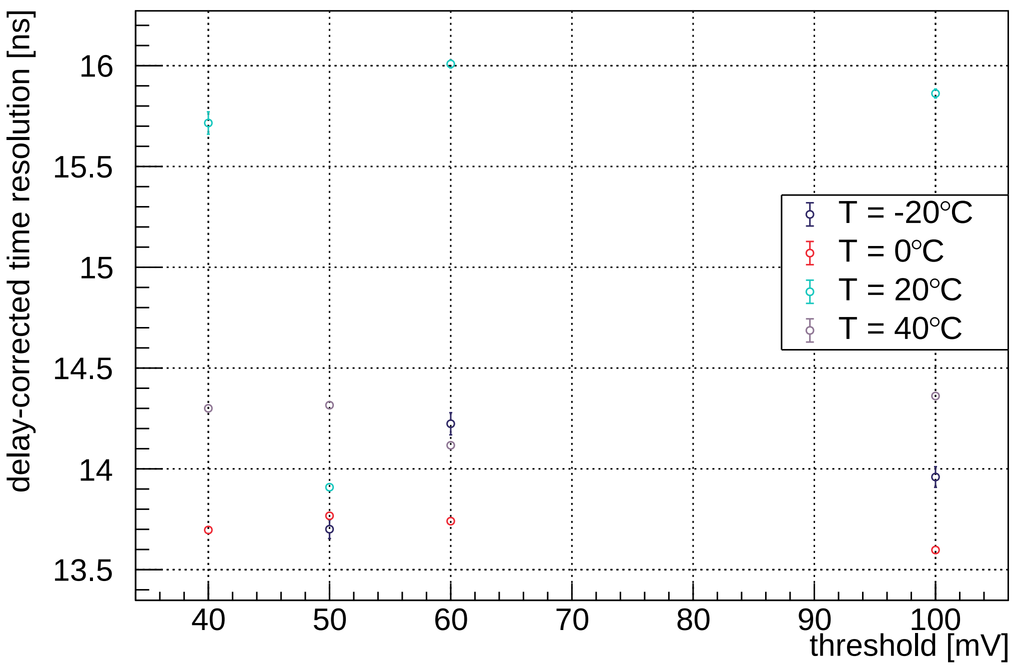

Figure A.3: The run- and delay corrected time resolution of a MuPix8 at different temperatures.

A.2 IV-Curves

In section 11.1 the breakdown voltage of the irradiated sensor at different conditions was mentioned. It is measured by increasing the applied high voltage and measuring the according current. This is then plotted and two linear functions are fitted to the breakdown part and to the normal operating part of the chip. The voltage at the intersection of these two lines then defines the breakdown voltage. The IV-curves of the measurements are shown in Figures A.4 to A.8.

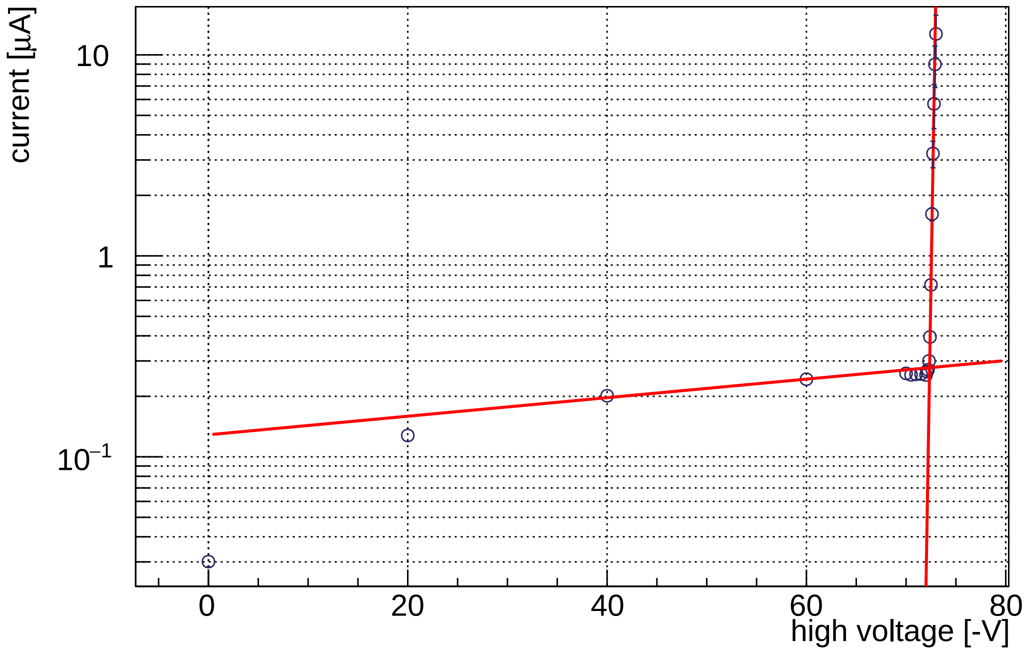

Figure A.4: IV curve at $-20\,°C$ before data taking.

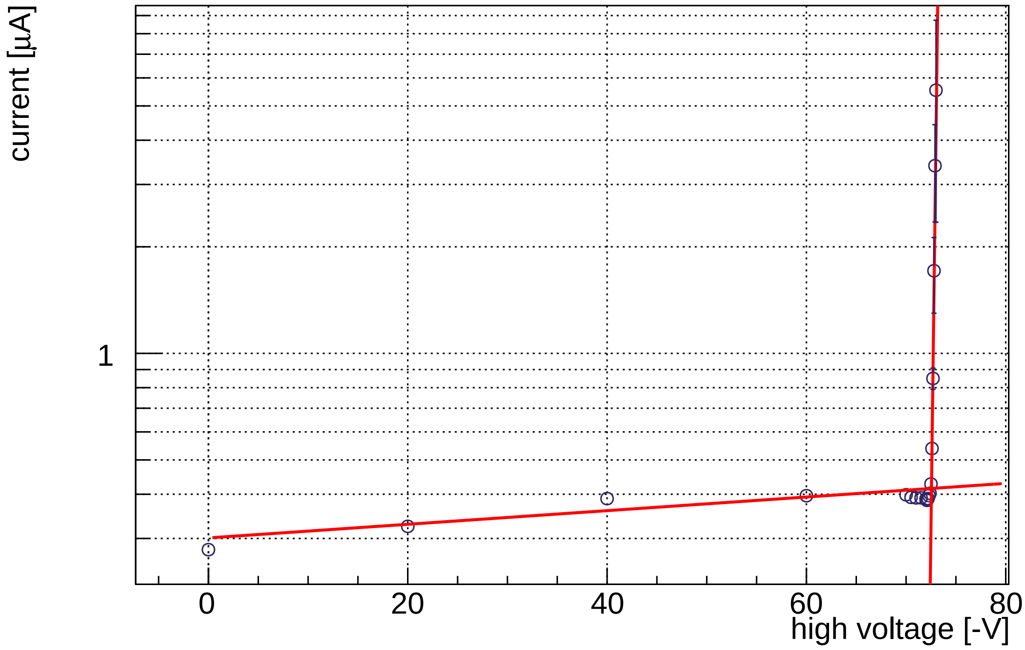

Figure A.5: IV curve at $-20\,^{\circ}\mathrm{C}$ after data taking.

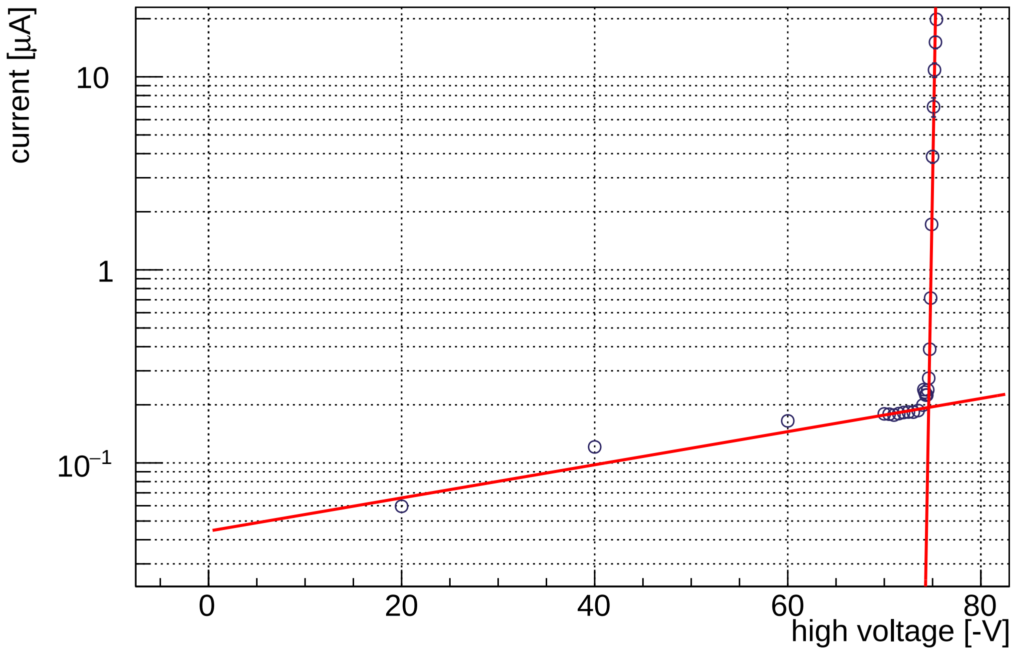

Figure A.6: IV curve at $20\,^{\circ}\mathrm{C}$ before data taking.

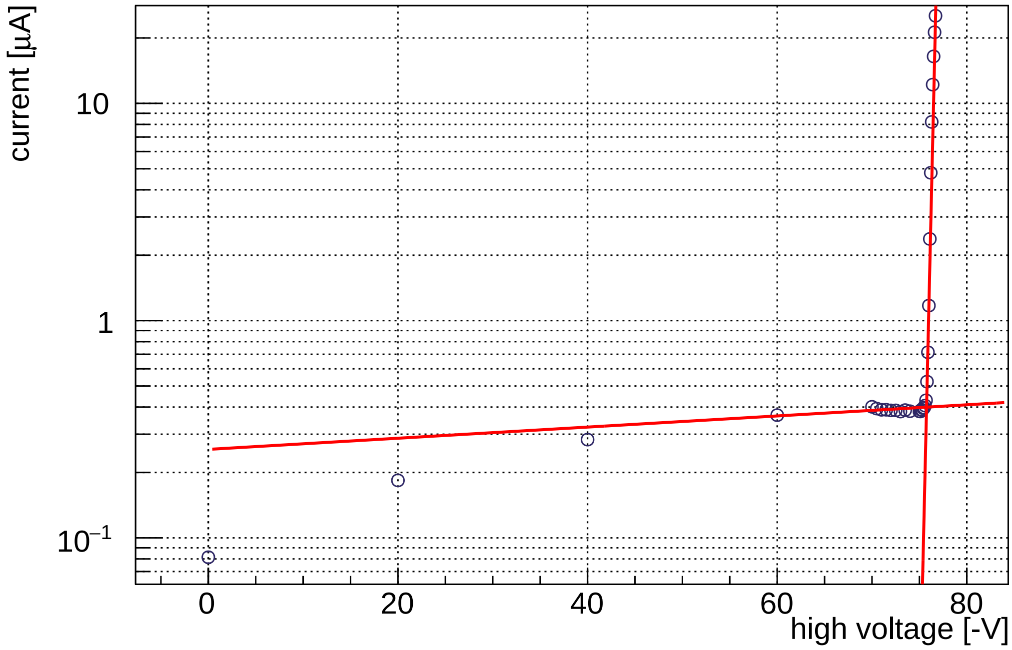

Figure A.7: IV curve at 40 °C before data taking.

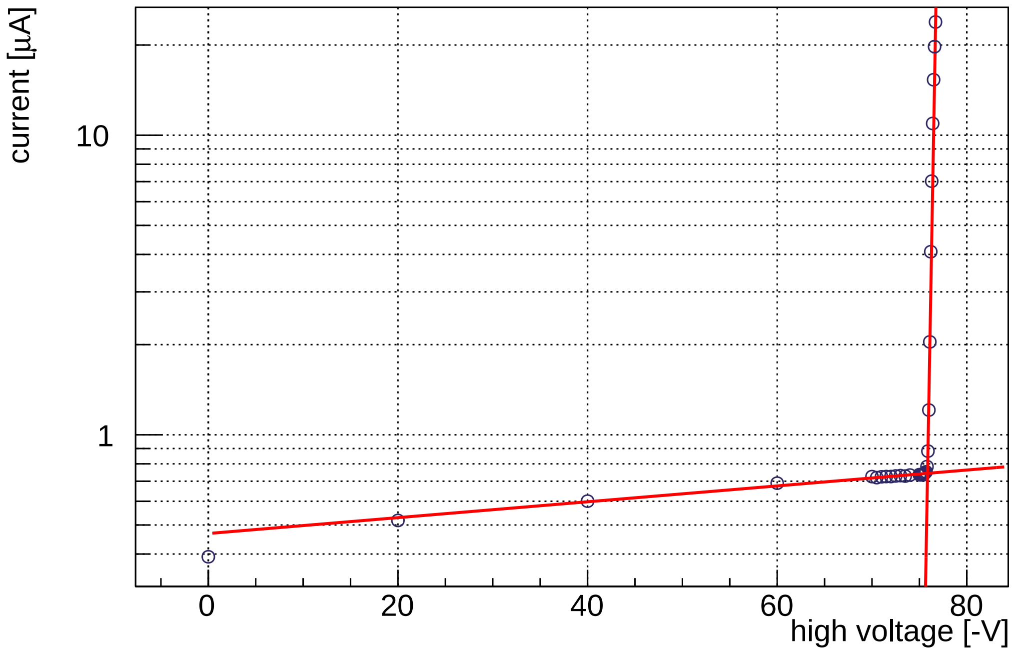

Figure A.8: IV curve at 40 °C after data taking.

A.3 Additional crosstalk plots

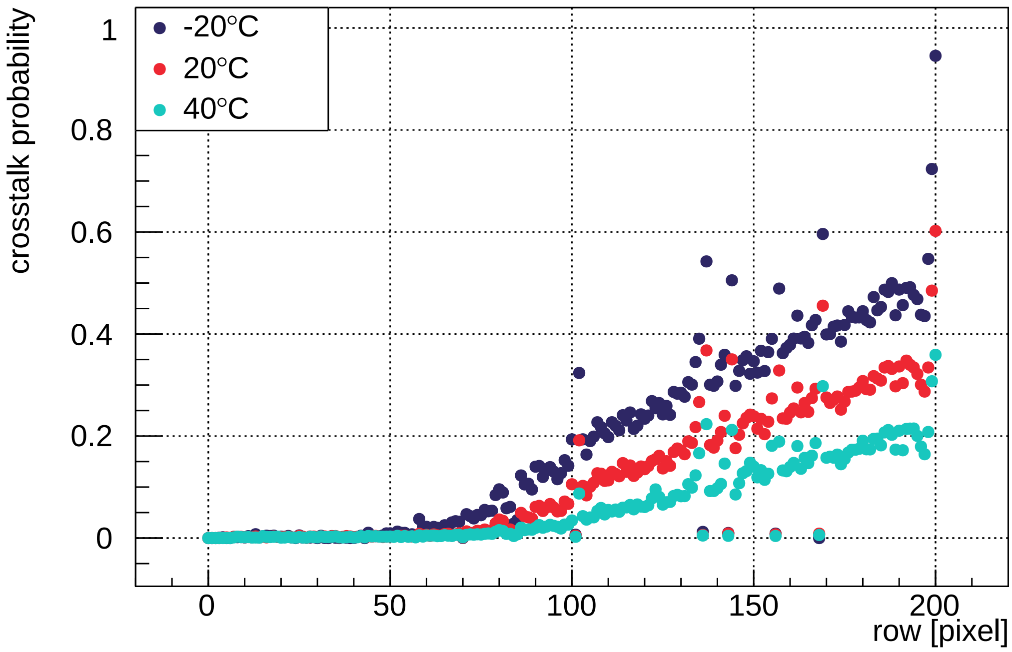

Figure A.9: Crosstalk at $-50\,\mathrm{V}$.

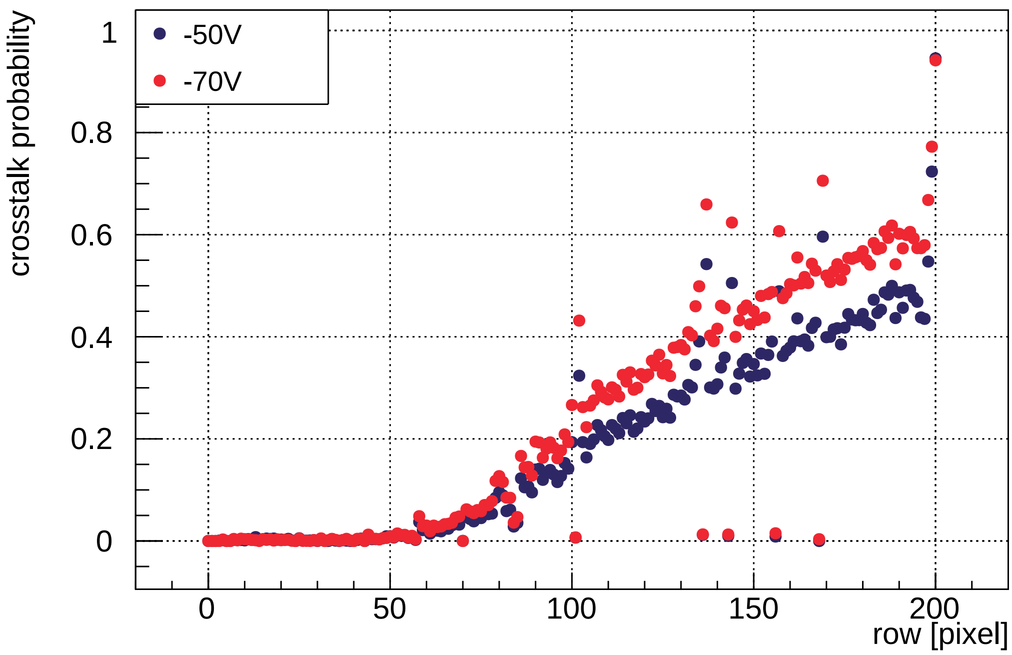

Figure A.10: Crosstalk at −20 °C.

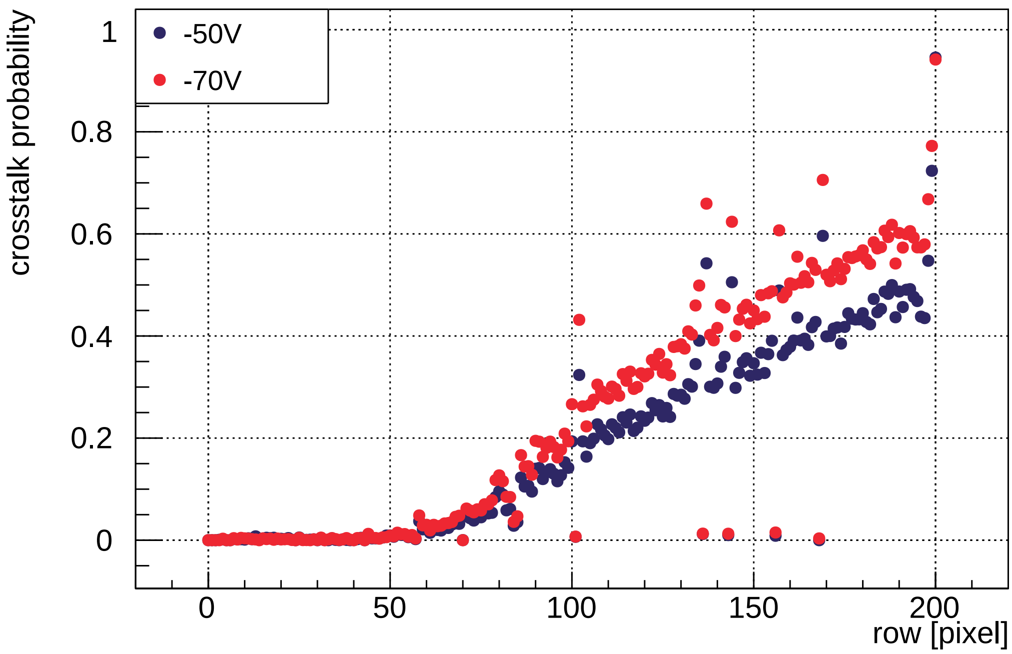

Figure A.11: Crosstalk at 40 °C.

A.4 Efficiency at $-50\,\mathrm{V}$

At $-50\,\mathrm{V}$ the efficiency shows a similar temperature- and threshold dependence as at $-70\,\mathrm{V}$, as shown in Figure 11.7. This is shown in Figure A.12.

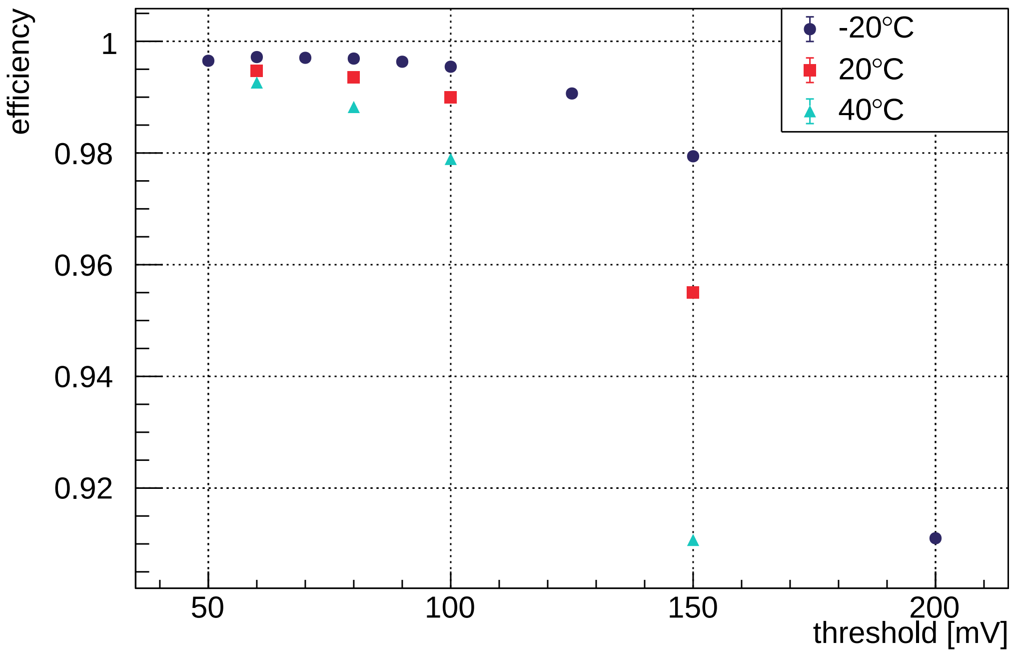

Figure A.12: Efficiency at $-50\,\mathrm{V}$.

Bibliography

[1] M. Aaboud et al. "Modelling radiation damage to pixel sensors in the ATLAS detector". In: *Journal of Instrumentation* 14.06 (June 2019), P06012–P06012. DOI: 10.1088/1748-0221/14/06/p06012.

[2] P. Baesso et al. *Technical design of the phase I Mu3e experiment.* Tech. rep. 2020. URL: https://arxiv.org/abs/2009.11690.

[3] M.-M. Bé et al. *Table of Radionuclides (Comments on evaluation).* Vol. 1–8. Monographie BIPM-5. BIPM, 2016.

[4] A. Blondel et al. *Research Proposal for an Experiment to Search for the Decay* $\mu \to eee$. Dec. 2012.

[5] R. Diener et al. "The DESY II test beam facility". In: *Nuclear Instruments and Methods in Physics Research Section A: Accelerators, Spectrometers, Detectors and Associated Equipment* 922 (2019), pp. 265–286. ISSN: 0168-9002. DOI: 10.1016/j.nima.2018.11.133.

[6] F. Faccio and G. Cervelli. "Radiation-induced edge effects in deep submicron CMOS transistors". In: *IEEE Transactions on Nuclear Science* 52.6 (Dec. 2005), pp. 2413–2420. DOI: 10.1109/TNS.2005.860698.

[7] Y. Fukuda et al. "Evidence for Oscillation of Atmospheric Neutrinos". In: *Phys. Rev. Lett.* 81 (8 Aug. 1998), pp. 1562–1567. DOI: 10.1103/PhysRevLett.81.1562.

[8] L. Gonella et al. "Total Ionizing Dose effects in 130-nm commercial CMOS technologies for HEP experiments". In: *Nuclear Instruments and Methods in Physics Research Section A: Accelerators, Spectrometers, Detectors and Associated Equipment* 582.3 (2007). VERTEX 2006, pp. 750–754. ISSN: 0168-9002. DOI: 10.1016/j.nima.2007.07.068.

[9] Jan Patrick Hammerich. "Analog Characterization and Time Resolution of a large scale HV-MAPS Prototype". Master thesis. Universität Heidelberg, 2018.

[10] H.H. Hansen. "Measurement of the beta-ray spectra of 90Sr-90Y". In: *The International Journal of Applied Radiation and Isotopes* 34.8 (1983), pp. 1241–1247. ISSN: 0020-708X. DOI: 10.1016/0020-708X(83)90193-X.

[11] Adrian Herkert. "Characterization of a Monolithic Pixel Sensor Prototype in HV-CMOS Technology for the High-Luminosity LHC". PhD thesis. Universität Heidelberg, Feb. 2020.

[12] G. Hernández-Tomé, G. López Castro, and P. Roig. "Flavor violating leptonic decays of τ and μ leptons in the Standard Model with massive neutrinos". In: *The European Physical Journal C* 79, 84 (Jan. 2019). ISSN: 1434-6052. DOI: 10.1140/epjc/s10052-019-6563-4. Considered Erratum from "Flavor violating leptonic decays of τ and μ leptons in the Standard Model with massive neutrinos". In: *The European Physical Journal C* 80, 438 (May 2019). ISSN: 1434-6052. DOI: 10.1140/epjc/s10052-020-7935-5.

[13] M. Huhtinen. "Simulation of non-ionising energy loss and defect formation in silicon". In: *Nuclear Instruments and Methods in Physics Research Section A: Accelerators, Spectrometers, Detectors and Associated Equipment* 491.1 (2002), pp. 194–215. ISSN: 0168-9002. DOI: 10.1016/S0168-9002(02)01227-5.

[14] Lennart Huth. "A High Rate Testbeam Data Acquisition System and Characterization of High Voltage Monolithic Active Pixel Sensors". PhD thesis. Universität Heidelberg, Dec. 2018.

[15] Dohun Kim. Picture taken by Dohun Kim.

[16] Hermann Kolanoski and Norbert Wermes. *Teilchendetektoren. Grundlagen und Anwendungen.* Berlin, Heidelberg: Springer Spektrum, 2016. ISBN: 978-3-662-45349-0. DOI: 10.1007/978-3-662-45350-6.

[17] Jens Kröger. "Readout Hardware for the MuPix8 Pixel Sensor Prototype and a Firmware-based MuPix8 Emulator". Master thesis. Universität Heidelberg, 2017.

[18] Yoshitaka Kuno and Yasuhiro Okada. "Muon decay and physics beyond the standard model". In: *Rev. Mod. Phys.* 73 (1 Jan. 2001), pp. 151–202. DOI: 10.1103/RevModPhys.73.151.

[19] S. Lazanu et al. "Non-ionising energy deposition of pions in GaAs and Si for radiation damage studies". In: *Nuclear Physics B – Proceedings Supplements* 61.3 (1998). Proceedings of the Fifth International Conference on Advanced Technology and Particle Physics, pp. 409–414. ISSN: 0920-5632. DOI: 10.1016/S0920-5632(97)00595-1.

[20] Claude Leroy and Pier-Giorgio Rancoita. *Principles of Radiation Interaction in Matter and Detection.* 4th ed. World Scientific Publishing Co. Pte. Ltd., 2016. ISBN: 9789814603188.

[21] Gerhard Lutz. *Semiconductor Radiation Detectors. Device Physics.* eng. SpringerLink : Bücher. Berlin, Heidelberg: Springer Berlin Heidelberg, 2007. ISBN: 978-3-540-71679-2. DOI: 10.1007/978-3-540-71679-2.

[22] Mu3e. Internal Mu3e images.

[23] Ivan Perić. "A novel monolithic pixelated particle detector implemented in high-voltage CMOS technology". In: *Nuclear Instruments and Methods in Physics Research Section A: Accelerators, Spectrometers, Detectors and Associated Equipment* 582.3 (2007). VERTEX 2006, pp. 876–885. ISSN: 0168-9002. DOI: 10.1016/j.nima.2007.07.115.

[24] Physikalisches Institut Heidelberg. Internal documentation of available radioactive sources, for the source in question issued by Eckert & Ziegler Nuclitec GmbH.

[25] Bogdan Povh et al. *Teilchen und Kerne. Eine Einführung in die physikalischen Konzepte*. 9th ed. Springer-Verlag Berlin Heidelberg, 2014. ISBN: 978-3-642-37822-5.

[26] Leonardo Rossi et al. *Pixel Detectors. From Fundamentals to Applications*. Particle Acceleration and Detection. Berlin Heidelberg: Springer, 2006. ISBN: 978-3-540-28332-4.

[27] Thomas Rudzki. Private communication.

[28] Stephen M. Seltzer and Martin J. Berger. "Improved procedure for calculating the collision stopping power of elements and compounds for electrons and positrons". In: *The International Journal of Applied Radiation and Isotopes* 35.7 (1984), pp. 665–676. ISSN: 0020-708X. DOI: `10.1016/0020-708X(84)90113-3`.

[29] *Silicon*. URL: `http://lampx.tugraz.at/~hadley/memm/materials/silicon/silicon.php`.

[30] *Silicon Dioxide Properties*. URL: `https://www.iue.tuwien.ac.at/phd/filipovic/node26.html`.

[31] J.R. Srour, C.J. Marshall, and P.W. Marshall. "Review of displacement damage effects in silicon devices". In: *IEEE Transactions on Nuclear Science* 50.3 (2003), pp. 653–670. ISSN: 0018-9499. DOI: `10.1109/TNS.2003.813197`.

[32] Frank Thuselt. *Physik der Halbleiterbauelemente. Einführendes Lehrbuch für Ingenieure und Physiker*. 3. Auflage. Berlin: Springer Spektrum, 2018. ISBN: 978-3-662-57638-0. DOI: `10.1007/978-3-662-57638-0`.

[33] Constantin Tormann. "Thermal Analysis of the Silicon Pixel Detector for the Mu3e Experiment". Bachelor thesis. Universität Heidelberg, 2018.

[34] Alena Weber and Ivan Peric. *Documentation MuPix8 (preliminary version 1)*. University of Heidelberg and Karlsruhe Institute of Technology. 2017.

Acknowledgments

In preparing and writing this thesis, I have learned a lot and gained a new perspective on scientific work. I'd like to thank Prof. André Schöning for giving me the opportunity to work in the Mu3e group on an equally interesting and challenging topic. Further, I thank Dr. Felix Sefkow for agreeing to be the second examiner of this thesis and for sparking my interest in particle physics.

Further, I am grateful for all the insight given and time spent explaining by David and Heiko who always had an open ear for any problems arising (and who, if the solution would not be apparent were always helpful in setting up an experiment to find it). I also thank all the other group members for their valuable input and the time spent together working toward the goal of making Mu3e happen, most notably Sebastian, Benjamin, Thomas, Luigi and Annie.

Additionally I would like to thank Lukas, Dohun, Marius, Konstantin, Alex and Florian for making and keeping the office and the laboratory at the institute a great workplace by sustaining an always friendly atmosphere and for always lending a hand when needed.

Finally, I thank my family for always supporting and encouraging me, not only in my studies.

Erklärung

Ich versichere, dass ich diese Arbeit selbstständig verfasst habe und keine anderen als die angegebenen Quellen und Hilfsmittel benutzt habe.

Heidelberg, den 29.10.2020,

Sebastian Preuß